Doctoral theses at NTNU, 2020:59

Dong Wang

Effect of Hydrogen in Advanced High Strength Alloys Revisited via Small-Scale In-Situ Techniques

Doctoral thesis

Dong Wang

ISBN 978-82-326-4472-8 (printed ver.)
ISBN 978-82-326-4473-5 (electronic ver.)
ISSN 1503-8181

NTNU
Norwegian University of Science and Technology

NTNU
Norwegian University of Science and Technology
Thesis for the Degree of
Philosophiae Doctor
Faculty of Engineering
Department of Mechanical and Industrial Engineering

Doctoral theses at NTNU, 2020:59

NTNU
Norwegian University of Science and Technology

Dong Wang

Effect of Hydrogen in Advanced High Strength Alloys Revisited via Small-Scale In-Situ Techniques

Thesis for the Degree of Philosophiae Doctor

Trondheim, February 2020

Norwegian University of Science and Technology
Faculty of Engineering
Department of Mechanical and Industrial Engineering

NTNU
Norwegian University of
Science and Technology

NTNU
Norwegian University of Science and Technology

Thesis for the Degree of Philosophiae Doctor

Faculty of Engineering
Department of Mechanical and Industrial Engineering

ISBN 978-82-326-4472-8 (printed ver.)
ISBN 978-82-326-4473-5 (electronic ver.)
ISSN 1503-8181

Doctoral theses at NTNU, 2020:59

Printed by NTNU Grafisk senter

Preface

This dissertation is submitted to the Norwegian University of Science and Technology (NTNU), in fulfillment of requirements for the Doctor of Philosophy degree. The work contained in this dissertation has been conducted in the period from September 2016 to September 2019 under the supervision of Prof. Afrooz Barnoush and co-supervision of Prof. Roy Johnsen. The main experimental work was carried out in the NTNU Nanomechanical lab and Metallography lab at the Department of Mechanical and Industrial Engineering, NTNU Nanolab, and NTNU XRD-lab.

The thesis was financially supported through the HyF-Lex project (244068/E30) by the Research Council of Norway (RCN) and the China Scholarship Council. The RCN is also acknowledged for support to NTNU NanoLab through the Norwegian Micro- and Nano-Fabrication Facility, Norfab (197411/ V30).

The thesis consists of two parts. The first part (Part I) includes introduction, literature review, and a summary of the work. The second part (Part II) contains four articles published or summitted to scientific journals.

Dong Wang

Trondheim, October 2019

Abstract

This thesis demonstrates a comprehensive study on the interaction between hydrogen and plasticity by using in-situ fine scale testing methods. It contains small-scale tensile tests with in-situ SEM observation as well as nanoindentation tests with in-situ electrochemical hydrogen charging and in-situ SPM imaging. There are two groups of materials studied in this PhD thesis. One is high-Mn TWIP steel, the other one is HEAs with stable and metastable states. The main object of this study is to gain understanding of hydrogen degradation mechanism by revealing the interaction between hydrogen and crystal defects.

First of all, a proper glycerol-based electrolyte was developed to protect specimen surface from corrosion through long-time cathodic hydrogen charging and testing, easing the following in-situ observation and characterization without further surface preparation. The deleterious effect of hydrogen on mechanical properties was demonstrated by tensile tests with in-situ SEM observation on pre-charged TWIP steel. During the tests, both fracture elongation and strength showed an accumulative degradation with amount of charged hydrogen indicated by the charging time. The charged hydrogen also induced secondary cracks on the gauge surface and a ductile-to-brittle fracture transition. This transition was triggered by sufficient hydrogen concentration with a threshold, which was quantitively determined by using the thermal desorption spectroscopy testing. In addition, the initiation and propagation of intergranular secondary cracks were comprehensively studied, and they were proposed as the result of hydrogen intrinsic detrimental effect on grain boundaries in combination with the stress concentration at intersecting points between deformation twin and grain boundary.

To get a deeper insight into the hydrogen detrimental effect, nanoindentation tests with in-situ hydrogen charging and in-situ SPM imaging were carried out. This technique can detect the effect of hydrogen on dislocation nucleation events, nanomechanical properties, and sample surface degradation. During the hydrogen charging, no hydrogen-induced surface degradation was observed on TWIP steel, while hydrogen-induced surface slip line formation and martensitic phase transformation were detected on HEAs with stable and metastable states, respectively. In the case of TWIP steel, introducing hydrogen results in a reduced pop-in load and an increased hardness. During the egression of hydrogen, both pop-in load and hardness showed recovery behavior but

with different recovery rates. The hydrogen reduced pop-in load indicates the hydrogen-enhanced homogeneous dislocation nucleation, which was fulfilled by reducing dislocation line energy or stacking fault energy. Tabor relation-based models were applied to analyze the hardness increment, and this was proposed due to the hydrogen-enhanced lattice friction. Moreover, the pop-in load and hardness have different affecting depths, which contain different amount of residual hydrogen during egression process lead to their different recovery rate.

In the case of HEAs, a severe hydrogen charging results in the formation of irreversible surface slip lines or martensitic phase transformation. The formation of surface lines is related to the plastic deformation caused by hydrogen-enhanced dislocation nucleation together with the hydrogen-induced internal stress, which was quantitively determined in this study. The formed surface lines irreversibly reduced the elastic modulus and pop-in load due to stress concentration and heterogeneous dislocation nucleation. The hardness, by contrast, was not influenced by the surface lines due to its deeper affecting depth. Martensitic phase transformation was detected on metastable HEA upon hydrogen charging, leading to an irreversible hardness increment. The hydrogen-induced internal stress together with the intrinsic hydrogen effect on SFE reduction and superabundant vacancies formation are proposed as the reasons. In addition, a critical amount of hydrogen is needed to trigger this phase transformation, and this threshold hydrogen content was determined in this study.

Acknowledgements

First and foremost, I would like to express my gratitude to my supervisor, Prof. Afrooz Barnoush. Without your help, this PhD work could not be finished. You always share your insightful ideas with me and encourage me to think in different ways. I will never forget the innovative brainstorms and discussions between us and your attitude towards science.

I would also like to thank my co-supervisor, Prof. Roy Johnsen for sharing your professional knowledge and valuable comments with me. I still remember I saw you working in the labs and taking care of experiments for so many times during weekends and holidays. You have provided an excellent role model for me. I also greatly appreciate the help from Prof. Torgeir Welo and Prof. Nuria Espallargas for taking care of my PhD defence and Dr. Nousha Kheradmand for teaching me technical skills in the labs and contributing valuable suggestions for my thesis writing.

During my PhD, I also received a lot of help outside NTNU. I would like to thank Dr. Xiaofei Guo from RWTH Aachen and Prof. Zhiming Li from Max-Planck Institut für Eisenforschung for providing me interesting materials and giving me so much valuable comments on my manuscripts. It was such a pleasure for me to work together with you.

Then I would like to appreciate all my lovely colleagues. Mr. Jan Inge Hammer Meling is the best office mate in the world! I appreciate your help to all my questions, the nice discussions, the interesting stories you told me, and your sense of humor. It was such a pleasure to have you around during my PhD journey! You will always be the top3 Norwegian-related memories in my life together with Norwegian salmon and Pinnekjøtt. Dr. Yun Deng gave me lots of great ideas on both experimental work and scientific writing. You made my PhD work much smoother. The same gratitude also goes to Dr. Di Wan. You are a talent young researcher and your technical skills made my work reaching to a higher level. You are also a good buddy. Thank you for helping me solving both life and scientific problems with your wisdom. My appreciation also goes to Mats Ingdal, Mohammad Ahmadzadeh, and Cristian Torres Rodriguez for helping me in corrosion lab, to Iman for helping me with the TDS measurement, to Gaute Stenerud for the help in the nanomechanical lab, to every colleagues in the Department of Mechanical and Industrial Engineering (MTP) for their limitless and friendly help, to my lovely friends in the Department of Material Science and Engineering for all the nice get-togethers and joyous moment.

Last and most importantly, I would like to express my deepest gratitude to my parents. Thank you for giving me a sweet home, teaching me to be a good person, and the never-ending love and support. To my lovely wife Xu Lu for your encouragement, patience, and understanding. You are my sunshine lighting up my most frustrating days. I love you forever! To my upcoming son. I cannot wait to see you in April. Wish you a lifetime of health and happiness!

List of papers

1. **D. Wang**, X. Lu, Y. Deng, X. Guo, A. Barnoush, Effect of hydrogen on nanomechanical properties in Fe-22Mn-0.6C TWIP steel revealed by in-situ electrochemical nanoindentation, *Acta Materialia* 166 (2019) 618-629.
2. **D. Wang**, X. Lu, D. Wan, Z. Li, A. Barnoush, In-situ observation of martensitic transformation in an interstitial metastable high-entropy alloy during cathodic hydrogen charging, *Scripta Materialia* 173 (2019) 56-60.
3. **D. Wang**, X. Lu, Y. Deng, D. Wan, Z. Li, A. Barnoush, Effect of hydrogen-induced surface steps on the nanomechanical behavior of a CoCrFeMnNi high-entropy alloy revealed by in-situ electrochemical nanoindentation, *Intermetallics* 114 (2019) 106605.
4. **D. Wang**, et al., Effect of hydrogen on the embrittlement susceptibility of Fe-22Mn-0.6C TWIP steel revealed by in-situ tensile tests, *submitted*.

Statement of author contributions

The main idea of this PhD research was designed together by Dong Wang and Prof. Afrooz Barnoush. Dong Wang performed most of the experimental work and data analysis presented in this thesis. Dr. Xiaofei Guo provided the Fe-22Mn-0.6C TWIP steel from the steel institute of RWTH Aachen university. Prof. Zhiming Li provided different types of high-entropy alloys from the Max-Planck-Institut für Eisenforschung. Xu Lu and Dr. Di Wan helped with the FIB milling and ECCI analysis. Dong Wang was the main author responsible for writing the manuscripts supervised by Prof. Afrooz Barnoush. All the co-authors joined the discussion and revised on the manuscripts.

Other scientific contributions

Other related publications

1. X. Lu, **D. Wang**, D. Wan, Z.B. Zhang, N. Kheradmand, A. Barnoush, Effect of electrochemical charging on the hydrogen embrittlement susceptibility of Alloy 718, *Acta Materialia* 179 (2019) 36-48.
2. X. Lu, **D. Wang**, Z. Li, Y. Deng, A. Barnoush, Hydrogen susceptibility of an interstitial equimolar high-entropy alloy revealed by in-situ electrochemical microcantilever bending test, *Materials Science and Engineering: A* 762 (2019) 138114.
3. T. Depover, T. Hajilou, D. Wan, **D. Wang**, A. Barnoush, K. Verbeken, Assessment of the potential of hydrogen plasma charging as compared to conventional electrochemical hydrogen charging on dual phase steel, *Materials Science and Engineering: A* 754 (2019) 613-621.
4. X. Lu, Y. Ma, M. Zamanzade, Y. Deng, **D. Wang**, W. Bleck, W.W. Song, A. Barnoush, Insight into hydrogen effect on a duplex medium-Mn steel revealed by in-situ nanoindentation test, *International Journal of Hydrogen Energy* 44(36) (2019) 20545-20551.
5. **D. Wang**, T. Hajilou, X. Guo, A. Barnoush, On the trail of the hydrogen embrittlement by novel critical experiments: In situ nanomechanical testing of high manganese steel, *Proceedings of the 3rd International Conference on Metals & Hydrogen* (2018).
6. X. Lu, **D. Wang**, A. Barnoush, Small-scale study of hydrogen embrittlement susceptibility of nickel-based 725 superalloy, *Proceeding of the Eurocorr Conference* (2019).
7. X. Lu, **D. Wang**, A. Barnoush, Hydrogen-induced cracking resolved by in-situ tensile test on Ni-based superalloys, *Proceedings of the 3rd International Conference on Metals & Hydrogen* (2018).
8. T. Depover, D. Wan, **D. Wang**, A. Barnoush, K. Verbeken, Hydrogen embrittlement evaluation of hydrogen plasma charged TRIP-assisted steel, *under review*.

Oral Presentations

1. **D. Wang**, A. Barnoush, Hydrogen effect on nanomechanical properties of TWIP steel revealed by in-situ electrochemical nanoindentation, *4th International Conference on Medium and High Manganese Steels,* Apr. 2019, Aachen, Germany.
2. **D. Wang**, A. Barnoush, Understanding the hydrogen embrittlement by novel critical experiments, *12th International Workshop on Materials Behavior at the Micro- and Nano-Scale*, Aug. 2019, Xi'an, China.
3. **D. Wang**, A. Barnoush, Effect of hydrogen on nanomechanical properties of TWIP steel and high-entropy alloy revealed by in-situ electrochemical nanoindentation, *Eurocorr*, Sep. 2019, Sevilla, Spain.

Posters

1. **D. Wang**, X. Guo, A. Barnoush, Effect of hydrogen on nanomechanical properties of Fe-22Mn-0.6C TWIP steel revealed by in-situ electrochemical nanoindentation, *3rd International Conference on Metals & Hydrogen*, Jun. 2018, Ghent, Belgium.
2. **D. Wang**, X. Lu, D. Yun, A. Barnoush, Hydrogen embrittlement in FeMnNiCoCr high entropy alloy revealed via in-situ nanoindentation and in-situ microcantilever bending tests, *MSE conference*, Sep. 2018, Darmstadt, Germany.
3. **D. Wang**, A. Barnoush, Examination of hydrogen embrittlement on high manganese steel by means of small-scale testing, *MSE conference*, Sep. 2018, Darmstadt, Germany.

Table of Contents

List of Abbreviations

AIDE	Adsorption-induced dislocation emission
BCC	Body centered cubic
BSE	Backscatter electron
EBSD	Electron backscatter diffraction
ECCI	Electron channeling contrast imaging
FCC	Face centered cubic
FIB	Focused ion beam
GIXRD	Grazing incident X-ray diffraction
GND	Geometrically necessary dislocation
HE	Hydrogen embrittlement
HEA	High-entropy alloy
HEDE	Hydrogen-enhanced decohesion
HEE	Hydrogen environment embrittlement
HELP	Hydrogen-enhanced localized plasticity
HESIV	Hydrogen-enhanced strain-induced vacancy formation
IHE	Internal hydrogen embrittlement
ISO	International Standard Organization
ND-IPF	Normal direction-inverse pole figure
SEM	Scanning electron microscopy
SFE	Stacking fault energy
SPM	Scanning probe microscopy

TDS	Thermal desorption spectroscopy
TEM	Transmission electron microscopy
TKD	Transmission Kikuchi diffraction
TRIP	Transformation-induced plasticity
TWIP	Twinning-induced plasticity
XRD	X-ray diffraction

Part I

1 Introduction

1.1 Background and motivation

The story of materials is the story of mankind's civilization. In the past thousands of years, metals have been the most essential materials fundamentally affected human's life in every aspect, such as economy, culture, and agriculture. With the development of technology, more and more advanced metallic materials have been discovered and produced. Nowadays, the metallic materials or alloys are used everywhere from construction to transportation, from manufactory to aerospace industry. Among these applications, there is a high possibility for metals to serve in harsh environments, such as oil and gas industries, nuclear constructions, and offshore infrastructures [1, 2]. These harsh environments always contain rich hydrogen and can degrade materials' mechanical properties, leading to premature or catastrophic failures known as hydrogen embrittlement (HE) [3]. The concept of HE was reported for the first time by W. H. Johnson in 1874 [4], where he described a brittle behavior on iron immersed into acids with the presence of hydrogen. Since then, intensive efforts were carried out to characterize and understand the HE phenomenon, and several mechanisms were proposed [5-10]. However, due to the complexity of HE, the fundamental mechanisms remain in debate and no single mechanism can exclusively explain all the hydrogen-induced failures.

In the past decades, the HE was drawing more and more attention due to the applications of ultra-high strength steels and clean energy revolution. The ultra-high strength steels exhibit both increased strength and improved fracture toughness, making them highly demanded in automobile and aerospace industries as a requirement of enhanced safety [11]. However, it has been reported that the HE susceptibility increases as the alloy's strength increases [12]. Moreover, due to the climate change and global warming, it is very urgent to shift our energy from polluting fossil fuels to clean and renewable energy, which makes hydrogen energy a very promising candidate [13]. Because hydrogen energy is a fuel that with high energy efficiency, overwhelming environmental benefits and exhaust only water when consumed in a fuel cell. As a result, the safety of hydrogen fuel usage, transportation, and storage is raising concern and it is crucial to minimize the risk of HE problems. Therefore, the basic mechanisms of HE need to be further understood.

Up to now, most of the HE studies were performed by using the macroscopic mechanical testing on specimens with pre-charged hydrogen [14, 15]. This testing system provides useful information on the HE phenomena showing the changes in mechanical properties and fracture behavior with adequate dissolved hydrogen. However, the focus of these studies is mainly on solving urgent engineering problems with the aim of selecting appropriate materials for certain applications and environment at macroscopic scale, making it very difficult to fully reveal the fundamental mechanism. Because HE is a complex process with many facets, and it is heavily affected by environmental and mechanical aspects as well as the intrinsic and extrinsic variables within the material. Therefore, the results of macroscopic tests reflect a combined effect between hydrogen and variable factors. Moreover, due to the hydrogen loss within the dwell time between charging and testing, the experimental work on pre-charged hydrogen cannot precisely connect HE phenomena with hydrogen content, which is important for determining the hydrogen degradation threshold. Therefore, a new method based on conventional mechanical tests that integrate in-situ hydrogen charging with small-scale testing is needed. The in-situ hydrogen charging provides a relatively stable hydrogen content at small testing volume and eases the hydrogen concentration quantification. The small-scale testing can clarify the individual interaction between hydrogen and defects such as dislocations, stacking faults, deformation twins, etc. With these above-mentioned advantages, the underlying mechanisms of HE can be better understood.

1.2 Objective

The primary objective of this thesis is to develop a comprehensive knowledge of mechanisms of hydrogen-induced degradation on advanced austenitic high strength alloys by using multi-scale in-situ testing methods. To achieve this goal, tensile testing was performed on specimens with pre-charged hydrogen in combination with in-situ SEM observation to understand the general hydrogen effect on macro-scaled mechanical properties and fracture mode. Small-scale nanoindentation testing was then carried out with in-situ hydrogen charging to reveal the interaction between hydrogen and material's intrinsic defects. Moreover, advanced post-mortem characterization techniques, including electron backscatter diffraction (EBSD), Electron channeling contrast imaging (ECCI), and transmission Kikuchi diffraction (TKD), were applied. The following objectives were pursued:

- Design an optimized hydrogen charging electrolyte, which can preserve the specimen surface from corrosion throughout the whole testing procedure, in order to minimize the influence on nanomechanical properties due to surface change and ease the post-mortem surface characterization.
- Achieve a comprehensive understanding of hydrogen degradation on high-Mn twinning-induced plasticity (TWIP) steel based on macro-scale tensile testing. This test focuses primarily on the hydrogen-induced mechanical properties reduction, the critical hydrogen content to trigger brittle fracture, and crack initiation and propagation.
- Evaluate the hydrogen effect on different advanced high strength alloys including high-Mn TWIP steel and high-entropy alloys (HEAs) with both metastable and stable states based on micro-scale nanoindentation testing, focusing on the influence of hydrogen on elastic modulus, dislocation nucleation, hardness, and phase stability.
- Comparing the results from aforementioned experiments with the existing mechanisms, providing necessary contributions to the HE studies.

1.3 Thesis outline

The thesis consists of two parts. **Part I** is an introduction part including 6 chapters. Chapter 1 gives a general introduction to the background which motivated the work in this thesis. In chapter 2, a brief overview of HE is introduced, focusing on the hydrogen sources, uptake, diffusion, and trapping. The hydrogen-defects interactions and the existing mechanisms of HE are also discussed. Chapter 3 provides the basic information of the studied advance austenitic high strength alloys, which contains high-Mn TWIP steel and HEAs in both stable and metastable states. Their HE behavior was also introduced here. Chapter 4 introduces the advanced nanoindentation technique, which can test the nanomechanical properties, such as elastic modulus, pop-in, and hardness. The detailed descriptions of the experimental methods and procedures are presented in Chapter 5. A summary of the papers is presented in Chapter 6. **Part II** comprises the research articles that have been published or in the process of being published in scientific journals.

2 Hydrogen embrittlement

2.1 Phenomenology

Hydrogen embrittlement (HE) is a process resulting in a delayed or sudden decrease of ductility or toughness of a metal due to the absorption of hydrogen, resulting in catastrophic failures and economic loss [16]. The HE has been reported to be detrimental to many alloys, such as high-Mn steels, high entropy alloys, Aluminum alloys, Magnesium alloys, and Titanium alloys [17-21]. HE endangers the operation safety of offshore platforms, oil pipelines, nuclear industries to name a few, and this topic has received increasing attention over the last decades. Despite its importance and massive performed studies, no consensus has been reached on understanding the mechanism of HE. The reason is that HE is a very complex phenomenon, which depends not only on the hydrogen environment, but also on the material's intrinsic properties and mechanical loading conditions. Figure 2-1 shows the three main factors that affect HE behavior [22]. Each factor has diverse conditions, which make it very difficult to conclude a universal mechanism to explain HE. In the past decades, the HE has been divided into different subgroups based on its different degradation types, such as hydrogen-enhanced fatigue cracking, hydride cracking, hydrogen-assisted stress corrosion cracking, etc [23]. To understand each failure phenomenon, the fundamental knowledge of hydrogen and its interaction with metals are required.

The hydrogen sources and uptake, its trapping sites and diffusion, together with several proposed mechanisms will be introduced and discussed in the following sections.

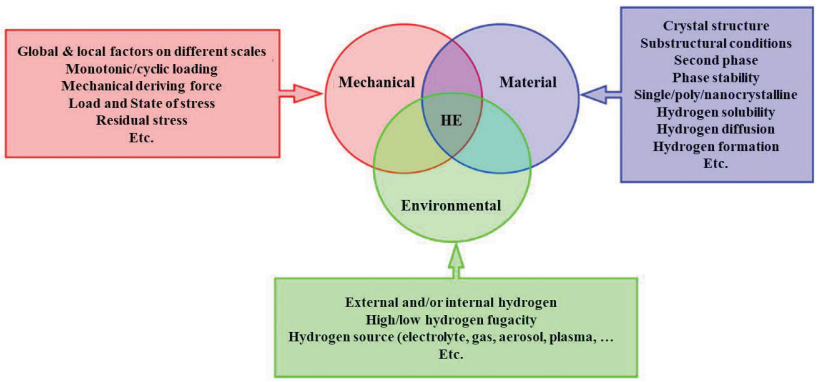

Figure 2-1: Global description of HE interaction aspects. Adapted from Ref. [22].

2.2 Hydrogen sources and uptake

The sources of hydrogen that induce embrittlement come from both manufacturing processes and operational uses. In manufacturing process, hydrogen can be produced during the welding and melting/casting of original material in moist atmosphere. The diverse heat treatment processes in hydrogen containing environment also lead to the formation of significant amount of hydrogen [24]. Another main source of hydrogen among manufacturing processes is the surface treatment, such as pickling, phosphating, and electroplating [25]. During these manufacturing processes, massive hydrogen can be generated and dissolved into metallic materials in the regions under high hydrostatic stress before industrial use. This pre-existing hydrogen would cause cracking under stresses even below the yield strength, referred to as internal hydrogen embrittlement (IHE) [26]. On the other hand, during operational use under the circumstances of cathodic protection, corrosion in aqueous solution, or directly exposed to hydrogen or hydrogen sulfide gases, atomic hydrogen can be produced, adsorbed, and absorbed by metals [27]. This dissolved hydrogen with high concentration also leads to brittle failure known as hydrogen environment embrittlement (HEE) [26]. Another important hydrogen source leading to HEE is the high-pressure hydrogen gas, which is getting more and more attention. On one hand, due to its high energy efficiency, high-pressure hydrogen gas is a promising fuel source for aerospace engineering, nuclear industries, and chemical industries; on the other hand, high-pressure hydrogen gas is a green energy that has a dramatical requirement in the future due to the climate change. Therefore, the hydrogen storage and transportation techniques are extensively demanded, and the corresponding equipment that exposed to hydrogen gas need to be protected from HE.

Hydrogen can enter a metal either from gas phase hydrogen or from aqueous electrolytes. In the case of gas phase, the uptake process starts with the adsorption of molecular hydrogen to metal surface. The adsorbed hydrogen then dissociated from molecular form to hydrogen atoms, which are further absorbed by metal surface and diffuse into the matrix [28]. In the current thesis, the source of hydrogen is only from aqueous electrolyte and the corresponding enter process will be discussed in detail below.

The hydrogen produced from aqueous electrolyte at cathodic polarization condition can be described in two steps. The first step is to form adsorbed hydrogen on metal surface, which is

shown in Eq. 2.1 and 2.2 depending on different pH value of the electrolyte: Eq. 2.1 describes the discharge of hydrated protons in acid solutions, while Eq. 2.2 indicates the electrolysis of water in alkaline solution.

$$H_3O^+ + M + e^- \rightarrow MH_{ads} + H_2O \text{ (in acid solution)} \quad (2.1)$$

$$H_2O + M + e^- \rightarrow MH_{ads} + OH^- \text{ (in alkaline solution)} \quad (2.2)$$

Here the MH_{ads} means the hydrogen atoms adsorbed on the metal surface. A large portion of the adsorbed hydrogen atoms will escape from the metal surface back to electrolyte. This detachment process occurs either from catalytic recombination regardless of the electrolyte as shown in Eq. 2.3 or by electrochemical desorption, which are exhibited in Eq. 2.4 and 2.5 for acid solution and alkaline solution, respectively.

$$MH_{ads} + MH_{ads} \rightarrow H_2 + 2M \quad (2.3)$$

$$MH_{ads} + H_3O^+ + e^- \rightarrow H_2 + H_2O + M \text{ (in acid solution)} \quad (2.4)$$

$$MH_{ads} + H_2O + e^- \rightarrow H_2 + OH^- + M \text{ (in alkaline solution)} \quad (2.5)$$

Despite the massive detached adsorbed hydrogen, a small percentage of hydrogen can switch the state from adsorption to absorption and consequently enter the metal surface as shown in Eq. 2.6.

$$MH_{ads} \rightarrow MH_{abs} \quad (2.6)$$

Where the MH_{abs} means the absorbed hydrogen right beneath the metal surface. The amount and rate of hydrogen absorption depends on many factors, such as intrinsic properties of metal, electrolyte composition, surface quality, current density, temperature, etc. One factor needs to be mentioned here is the hydrogen recombination poison, which is often used during the electrochemical hydrogen charging [29]. The poisons, which are normally based on the elements from the VA and VIA groups, are used to retard the recombination of adsorbed hydrogen and promote hydrogen entry into the metal as absorbed hydrogen. The absorbed hydrogen can move to deeper position by further diffusion process.

2.3 Hydrogen diffusion and trapping

Diffusion is a process of random movement of atoms caused by a concentration gradient and thermal activation [30]. The diffusion flux density was defined as the number of particles that pass through a unit area in a unit of time. According to the Fick's law, the diffusion flux density is proportional to the concentration gradient shown as follows.

$$j_D = -D\frac{d_c}{d_x} \tag{2.7}$$

where j_D is the diffusion flux density with the dimension of cm^{-2} s^{-1}, D is referred to as the diffusion coefficient with the dimension of cm^2 s^{-1}, and the minus sign on the right-hand side means the flux direction is opposite to the concentration gradient, i.e. from higher to lower concentration. The D has been experimentally confirmed as

$$D = D_0 \cdot \exp(-\frac{Q}{kT}) \tag{2.7}$$

where D_0 is a pre-exponential factor, Q is the activation energy, k is the Boltzmann constant, and T is the temperature. The activation energy Q indicates the elementary process of atomic motion depending on different elements and crystal structures. The different activation energy in different diffusion systems differ diffusion coefficient by several orders of magnitude [28].

In the case of hydrogen diffusion in metals, it generally shows a very high diffusion rate due to the small size of hydrogen atom. However, the behavior of hydrogen diffusion and solubility exhibit a huge difference between different crystal structures [26]. For metals with a body centered cubic (BCC) structure, the preferred interstitial sites for hydrogen are the kinetic rates of e tetrahedral sites at ambient temperature, since the size of tetrahedral site is about twice of that of octahedral site. While for face centered cubic (FCC) structure metals such as austenitic stainless steels, octahedral sites are relatively larger and are the preferred interstitials sites for hydrogen atoms [28]. Figure 2-2 shows the solubility of hydrogen in different steels. It clearly shows that metals with FCC structure generally have a higher hydrogen solubility compared to metals with BCC structure. This is due to the relatively larger size of octahedral sites for FCC metals than that of tetrahedral sites for BCC metals as the preferred hydrogen occupation sites.

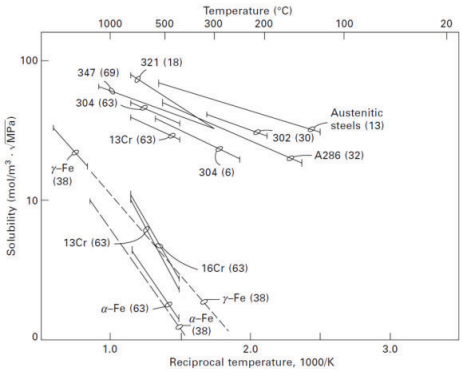

Figure 2-2: The solubility of hydrogen in different steels. Adapted from Ref. [28].

These interstitial hydrogen atoms are defined as diffusible hydrogen. In addition, the hydrogen can also be trapped at imperfections of microstructure in metals, such as vacancies, dislocations, grain boundaries, and precipitates as shown in Figure 2-3 [31]. These trapping sites strongly affect the hydrogen diffusion and distribution in materials and are classified into reversible and irreversible trapping sites depending on the hydrogen desorption activation energy [32]. The dislocations and grain boundaries are examples of reversible traps, which have lower trapping energy for hydrogen, making it possible for hydrogen to escape at elevated temperature [8, 33]. By contrast, the carbides are considered as irreversible ones with much higher hydrogen binding energy, making the hydrogen be irreversibly trapped [34, 35].

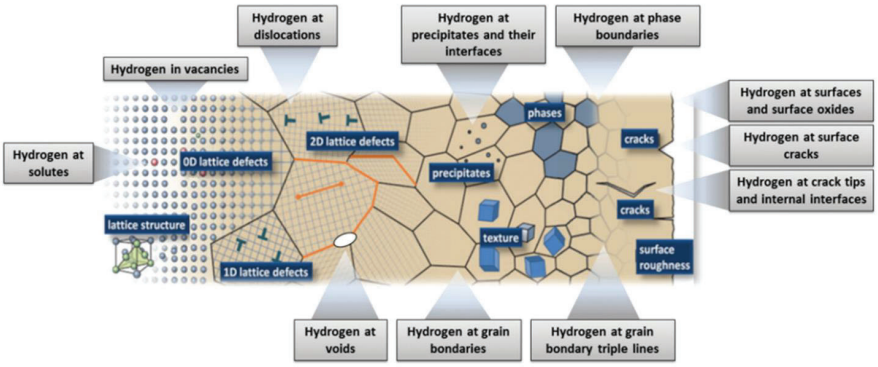

Figure 2-3: Schematic illustrations of sites and traps for hydrogen in materials. Adapted from Ref. [31].

Not only the hydrogen solubility is affected by the crystal structure, the diffusivity of hydrogen is also decisively affected by the crystal structure. The rate of hydrogen diffusion at ambient

temperature are generally four to five orders of magnitude higher for metals with BCC structure than that for FCC metals as shown in Figure 2-4 [28, 36]. The relatively low diffusivity and high solubility of hydrogen for FCC metals can lead to a superabundant hydrogen accumulated in the vicinity of sample surface resulting in a high hydrogen gradient toward the sample inside [37]. As a result, surface blisters was reported in alloy 718 [38], surface slip lines was observed in high-entropy alloy [39], and martensitic phase transformation was detected in 304 stainless steels [40, 41] after electrochemical hydrogen charging.

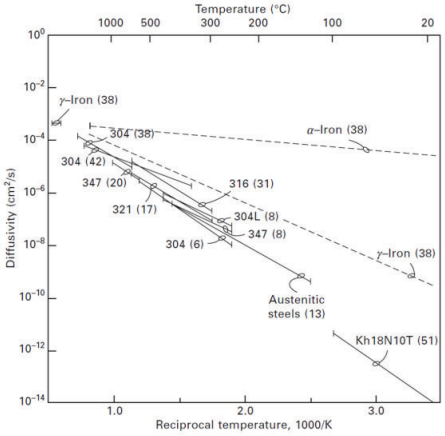

Figure 2-4: Hydrogen diffusivity in different stainless steels. Adapted from Ref. [28].

The hydrogen diffusion and trapping mechanisms have also been proved to be affected by the grain boundary type and grain size. Different grain boundary type shows different impact on the hydrogen behavior. The grain boundaries with low misorientation have ordered structure and can be considered as an accommodation of defects such as dislocations and vacancies. These grain boundaries normally represent as trapping sites for hydrogen and retard the diffusivity of hydrogen [36, 42]. However, the grain boundaries with a high misorientation contain a higher disordered structure with a larger excess free volume for hydrogen diffusion. Therefore, the hydrogen diffusion is accelerated at high angle grain boundaries by the mechanism of short-circuit diffusion [43, 44]. Oudriss et al. studied the effect of grain size on hydrogen diffusion and found a different diffusion behavior at different grain size [33]. Specifically, when the grain size is larger than a critical value (45 μm as proposed), the short-circuit diffusion dominates the diffusion process making the grain boundaries as the preferential diffusion paths. In this domain, a decreasing

diffusion coefficient was observed with a larger grain size. This is due to the reduction of grain boundary occupation at larger grains. When the grain size is less than the critical value down to several micrometer size, the diffusion coefficient shows a reduction trend with the reduction of grain size. This is proposed due to the increase of the density of geometrically necessary dislocations at grain boundaries acting as hydrogen irreversible trapping sites. Moreover, at the nano-grain scale, an acceleration of hydrogen diffusion was observed despite the increase in dislocation density. This is interpreted as the increment of triple junction density in nanocrystalline and accelerate the hydrogen diffusion.

2.4 Hydrogen embrittlement mechanisms

The fundamental mechanisms for HE has been extensively studied. However, it is still a controversial question without a clear consensus. Different mechanisms have been proposed based on different experiments and observations. Most of the HE problems without hydrides formation can be explained by using one or a combination of these mechanisms. The most popular models are introduced as following.

Hydrogen-enhanced localized plasticity

The mechanism of Hydrogen-enhanced localized plasticity (HELP) was firstly introduced by Beachem [45, 46], who performed in-situ transmission electron microscope (TEM) observation on a thin specimen that under plastic deformation exposed in hydrogen atmosphere. Observation showed that dislocations started to move with an increased velocity when hydrogen was introduced into the electron microscope. The dislocation structure ended up with a decreased spacing of dislocations in pile-ups. Based on this direct observation, the HELP mechanism proposes that solute hydrogen can facilitate the movement of dislocations by shielding the stress field of dislocations from interacting with other elastic obstacles. As a result, localized deformation is initiated near crack tips, where contains a high hydrogen concentration due to the hydrostatic stress [5, 47, 48]. Then the crack grows by a more localized microvoid coalescence process than that occurs in hydrogen-free conditions. The schematic diagram illustrating the HELP mechanism is shown in Figure 2-5.

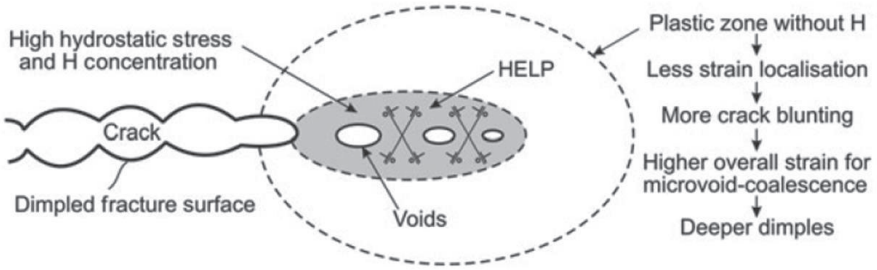

Figure 2-5: Schematic diagram illustrating the HELP mechanism, showing a localized plastic zone in the area with high hydrogen concentration. Adapted from Ref. [49].

Besides the direct in-situ TEM observation, the HELP mechanism can also be used to explain the appearance of quasi-cleavage fracture and slip line arrangement in hydrogen charged samples [50-53]. Moreover, the atomistic calculation supports HELP mechanism by indicating that solute hydrogen reduces dislocation core energy in aluminum and lowers the Peierls stress needed for dislocation movement [54].

Despite its popularity and widespread supports on HELP mechanism, there are still dissenting opinions. Firstly, the in-situ TEM study used a very thin specimen, which had a two-dimensional stress state. Therefore, the influence of surface effect on dislocation movement is debatable and might be a more dominated factor than the hydrogen. Moreover, Song and Curtin proposed that no shielding effect on dislocation interactions was provided by hydrogen and the solute hydrogen reduced the dislocation mobility instead of facilitating it, which is consistent with the solute drag theory based on atomic simulations [55, 56]. This hydrogen reduced dislocation mobility was further supported by the in-situ nanoindentation test [57], which explained the hydrogen-enhanced hardness as a result of hydrogen enhanced lattice friction on dislocation movement.

Hydrogen-enhanced decohesion

The mechanism of Hydrogen-enhanced decohesion (HEDE) was first proposed by Troiano in 1960 [58], and further developed in detail by Oriani and McMahon [59, 60]. The HEDE mechanism states that the cohesive energy between atoms decreases when hydrogen is trapped at the grain boundaries, interphases, and cleavage planes [61]. As a result, these areas become the most vulnerable sites that undergo cracking under stress. The schematic diagram illustrating the HEDE

mechanism is shown in Figure 2-6. The HEDE mechanism is usually evoked when the displacement of crack-tip-opening reaches to the half interatomic spacing during the tensile test [62]. Moreover, the HEDE mechanism is often used to explain the intergranular fracture behavior on hydrogen charged samples.

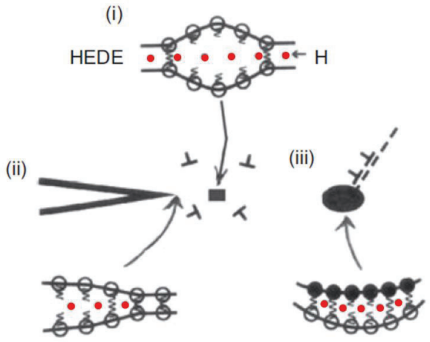

Figure 2-6: Schematic diagram illustrating the HEDE mechanism. (i) hydrogen in lattice, (ii) hydrogen absorbed at the crack tip, (iii) hydrogen at the interface between particle and matrix. Decohesion happens owing to the weakening of atomic bonding. Adapted from Ref. [49].

However, the direct experimental evidence of HEDE mechanism is still missing due to the technical limitations to observe crack tips on bulk materials at atomic scale. Also, it was proved that a large amount of hydrogen in interstitial sites ahead of crack tip is needed to trigger the decohesion. This high concentration of hydrogen requires a very high elastic stress, which is impossible in real cases [63].

Adsorption-induced dislocation emission

The Adsorption-induced dislocation emission (AIDE) mechanism was first introduced by Lynch [7]. He proposed that the adsorbed hydrogen can facilitate the dislocation nucleation at crack tip, and the nucleated dislocations subsequently move away from the crack tip to the area ahead of crack tip. AIDE mechanism contains two steps: dislocation nucleation and dislocation emission. The nucleation step involves the simultaneous dislocation core formation at the crack tip by atomic shearing effect, i.e., breaking and reforming of interatomic bonds, which is weakened by adsorbed hydrogen. The hydrogen-promoted dislocation emission on suitably inclined slip planes leads to crack growth [7]. In the AIDE model, the crack growth is not only facilitated by dislocation

emission, the microvoids formation ahead of crack tips also contribute to this process. The coalescence of cracks with microvoids produces fracture surface with dimples [64, 65].

In summary, AIDE is fundamentally a complex model combining both HELP and HEDE mechanisms. It is based on the fact that hydrogen weakens the interatomic bonding energy (HEDE) in combination with crack growth due to localized slip (HELP). The AIDE mechanism finds its popularity in explaining the fracture surface with dimple structure [64].

Hydrogen-enhanced strain-induced vacancy formation

The hydrogen-enhanced strain-induced vacancy formation (HESIV) was first introduced by Nagumo [66], suggesting that hydrogen enhances the creation and clustering of vacancies during plastic deformation and therefore promotes voids formation and crack propagation. Nagumo et al. [66] performed thermal desorption spectroscopy (TDS) analysis on hydrogen gas charged steels and observed that the amount of hydrogen absorbed in the weak trapping sites substantially increases with plastic strain. The weak trapping sites normally indicate as vacancies. In combination with further fracture surface observation, hydrogen was proposed to enhance the vacancy formation. These vacancies agglomerate to voids localized in the vicinity of crack tip leading to shear instability with crack propagation [67]. McLellan et al. [68] performed thermodynamic analysis on iron and stated that the formation of large amount of vacancies was caused by the reduction in vacancy formation energy due to the interaction of hydrogen atoms with iron. The HESIV mechanism was also widely supported by the studies on hydrogen-induced failures in Ni-based alloys through both experimental work and computational simulations [8, 69-71].

Defactants theory

Kirchheim introduced the Defactants theory as “DEFect ACTing AgeNTS” [72], in analogy to the concept of surfactants (SURFace ACTing AgeNTS), which indicate a reduced surface energy of water by solute molecules. It is a novel concept explaining HE behavior based on thermodynamic calculations. The Defactants theory proposed that the segregation of defactants, such as hydrogen, into defects, such as vacancies, dislocations, and stacking faults, can reduce the defect formation energy and therefore improves the generation rate [9, 10]. This theory can be directly proved by

the in-situ nanoindentation tests, where the homogeneous dislocation nucleation is enhanced with a reduced pop-in load in the presence of hydrogen [22, 57, 73].

In fact, HE is a very complex process depending on material, environment, and stress state. No aforementioned mechanisms can exclusively explain all HE issues and occasionally several different mechanisms need to combine together to explain the HE behavior [16]. For example, in the process of hydrogen-induced crack propagation, dislocations first nucleate at the crack tip based on AIDE and then steadily move away due to the enhanced mobility according to HELP [26]. Furthermore, these mechanisms are not completely distinct but with some overlap between each other. AIDE and defactants both contain similar aspects on hydrogen eased dislocation formation, which is also described in HEDE mechanism [26].

3 Advanced high strength alloys and their HE behavior

3.1 High-Mn TWIP steels

TWIP steels, which stand for twinning-induced plasticity steels, combine high strength with good ductility. This outstanding mechanical property made them very attractive for structural applications as soon as they were introduced [74]. The original idea of TWIP steel was proposed by Robert Hadfield in 1888 by adding high content of manganese to low alloyed steels to achieve a fully austenitic structure at room temperature [75]. During the last decade, a breakthrough combination between strength and ductility was achieved through tuning the stacking fault energy (SFE) by adding more manganese and less amount of carbon, plus other alloying elements such as Al (<3 wt.%) or Si (<3 wt.%) [76].

The SFE is the most crucial parameter in FCC metals determining their deformation mechanisms and mechanical properties. When the SFE is less than 18 mJ/m^2, the phase transformation from austenite to martensite is energetically favorable, while when the SFE is higher than 45 mJ/m^2, the plastic deformation with strain hardening is only controlled by the dislocation glide and interactions [77, 78]. The twinning behavior only occurs when the SFE is between 18 and 45 mJ/m^2 [79]. By choosing the appropriate alloying elements, the TWIP steels are controlled to a relatively low SFE between 20 and 40 mJ/m^2 at room temperature, in order to exploit the fully TWIP effect during deformation [77]. The Manganese is an austenite stabilizing element and with a high concentration, as in TWIP steel, can dramatically reduce the austenite transformation temperature and increase the solubility of carbon [80]. The alloying elements of Al and Si can increase and decrease the SFE, respectively, tuning the SFE in the optimized range. Additionally, the Al can reduce the weight of steel, and both Al and Si contribute to enhance the strength by solid solution hardening [81]. As a result, during plastic deformation the TWIP steels with appropriate SFE form isolated stacking faults and deformation twins, which reduce the dislocation mean free path as these are considered to be strong obstacles to dislocation glide [82, 83].

The newly developed TWIP steels show an excellent strength with ultimate tensile strength up to 1 GPa, in combination with high ductility with fracture elongation up to 80% [76, 80]. Figure 3-1 shows the mechanical properties of TWIP steels in comparison with traditional steels. Therefore,

TWIP steels are becoming prime candidate materials for applications of automotive, shipbuilding, and oil and gas industries.

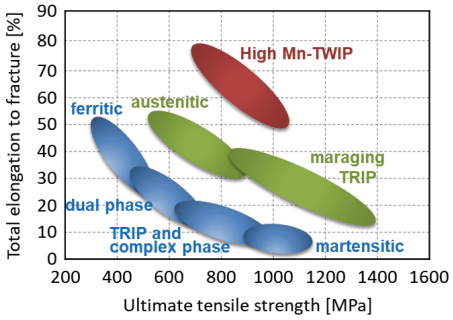

Figure 3-1: Ductility and strength in tension diagram for different steels.

3.2 Hydrogen embrittlement in high-Mn TWIP steels

The TWIP steels generally have better resistance to HE when compared to low carbon steels, dual phase steels, and martensitic steels [84-86]. This is due to the low hydrogen diffusivity in TWIP steels with FCC structure, which suppresses the severe interactions between hydrogen and dislocations. However, the hydrogen induced fracture was also reported in TWIP steels when the materials are subjected to severe mechanical loading conditions in combination with abundant charged hydrogen [86]. Up to now, most of HE studies on TWIP steels were conducted by using slow strain rate tensile tests (SSRT) or cup drawing tests. These tests mainly focused on the influencing factors of microstructure, alloying elements, hydrogen content, and strain rate to the HE susceptibility.

The effect of grain size on the susceptibility of HE in Fe-22Mn-0.6C TWIP steel was studied by Zan et al. [14]. They performed SSRT tests on hydrogen pre-charged samples with four different grain sizes and observed that the sample with a finer grain size showed a better HE resistance with higher fracture stress and strain. The raised HE susceptibility in coarse grain was explained due to the early initiation of deformation twins with a high density as well as the higher amount of diffusible hydrogen per unit grain boundary area. The behavior of hydrogen-assisted cracking on Fe-18Mn-1.2%C TWIP steel was studied in detail by Koyama et al. [87]. They observed that the cracking was initiated not only on the grain boundaries, but also on the twin boundaries, and the

cracking propagation were observed along both boundary types. The hydrogen-assisted twin boundary failure was proposed as the result of hydrogen-induced stress concentration at the tip of the deformation twins. The effect of alloying elements on HE susceptibility was also studied focusing on the influence of Si, Cu, and Al in solid solution states [88-92]. It has been reported that the addition of 1.5% Si reduces the HE resistance with larger brittle area on the fracture surface, but the mechanical twinning behavior is kept during plastic deformation. Further addition of Si to 3% leads to a considerable amount of deformation-induced martensite, which causes severe hydrogen-induced deterioration [88]. The addition of Cu was proposed to suppress HE with a reduced hydrogen-induced fracture elongation loss. This is because adding Cu into TWIP steels leads to an increased SFE, which makes cross-slip easier to occur and inhibits dislocation pile-ups as well as suppresses the local hydrogen concentration [92]. Among all the alloying elements in TWIP steels, Al is the most important one. Similar to the Cu effect, Al also rises the SFE and thereby increases the resistance to HE [89]. Moreover, the permeability and diffusivity of hydrogen are reduced by the addition of Al [93]. As a result, not only the hydrogen-induced mechanical degradation from tensile tests are suppressed, the hydrogen-induced delayed fracture is also suppressed as shown in Figure 3-2 as an example.

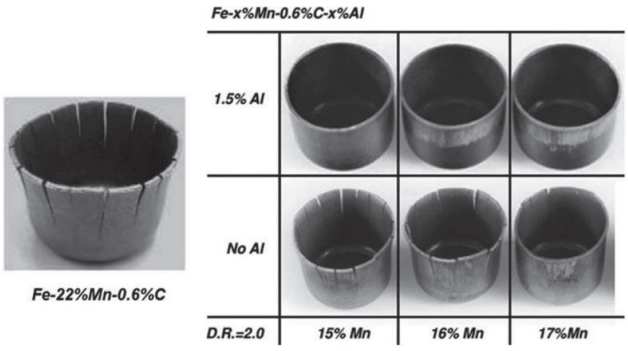

Figure 3-2: Hydrogen-induced delayed fracture in TWIP steels with and without the addition of Al. The value of D.R. indicates the drawing ratio. Adapted from Ref. [86].

The effect of hydrogen content on the tensile properties of Fe-18Mn-0.6C TWIP steel was studied by Koyama et al. [94]. The results showed that the samples with relatively low diffusible hydrogen content showed ductile fracture with high resistant to HE, while the samples with high hydrogen content exhibited an intergranular fracture with clear strength degradation. In addition, the HE

susceptibility of TWIP steels was also affected by the strain rate. It shows that the HE is substantially more pronounced at lower strain rates [15]. Because at lower strain rates, there is an increased waiting time for hydrogen to segregate and it is easier for hydrogen-decorated dislocations to move to twin boundaries and deliver hydrogen atoms there.

3.3 High-entropy alloys

In 2004, a new group of alloys was introduced by Yeh et al. referred to as high-entropy alloys (HEAs) [95]. They are composed of at least four principal alloying elements, each of which has a concentration ranging between 5 and 35 at.%. In contrast to conventional alloys, which usually based on one major element with additional minor alloying elements to improve specific properties. The HEAs have no "base element" and the random mixing of multi-elements leads to a high configurational entropy. The high configurational entropy, together with other intrinsic characteristics such as sluggish atomic diffusion and large lattice distortion, promote the formation of solid solution phase with higher stability and impede the dislocation mobility, thereby improving the mechanical properties [96-98]. As a result, the HEAs attracted considerable attention since the first introduction. Up to now, massive single phase HEAs have been developed, such as CoCrFeMnNi, CoCrCuFeNi, NiFeCrCo, and $Al_{0.5}$CoCrCuFeNi with FCC structure [99], ZrNbTiVHf, NbMoTaW, and TaNbHfZrTi with BCC structure [100], and BeCoMgTi and CoOsReRu with HCP structure [101]. Among them, the CoCrFeMnNi, described by Cantor et al. [102], has been mostly studied and well understood. It was reported that CoCrFeMnNi has high thermodynamic stability, excellent malleability, high strength, and good ductility even at cryogenic temperature [103-105], and the deformation-induced twins were found to be responsible for these outstanding mechanical properties. This suggests that this HEA has a moderate SFE, which agrees with the first-principles calculation [106] and experimental measurement [107].

In order to improve the mechanical properties of original equiatomic HEAs, a new class of HEAs with additional interstitial carbon were produced [108, 109]. Figure 3-3 shows the effect of interstitial carbon on the mechanical properties on CoCrFeMnNi HEA (curves #5 and #6) [109]. The results show that adding 0.5 at. % carbon enhanced both yield strength and ultimate tensile strength while maintained the fracture elongation. It needs to mention here that the ductile

reduction of curve #6 compared with curve #5 mainly comes from its relative larger grain size. The interstitial carbon-enhanced mechanical properties was reported due to its promptness of deformation twinning and interstitial solid solution strengthening [110]. The mechanical properties of HEAs were further enhanced by varying the Mn contents and as a result the phase stability can be tuned from stable to metastable state in order to achieve the transformation-induced plasticity (TRIP) effect as shown in Figure 3-3 (curves #1-#4) [111]. Therefore, the recently developed HEAs exhibit excellent combination of strength and ductility due to the activation of practically all possible strengthening effects, e.g. interstitial and substitutional solid solution strengthening, TWIP effect, TRIP effect, precipitation hardening, work hardening by staking faults and dislocations, and grain refinement [108, 112]. These outstanding features make HEAs as promising materials for advanced structural applications in future.

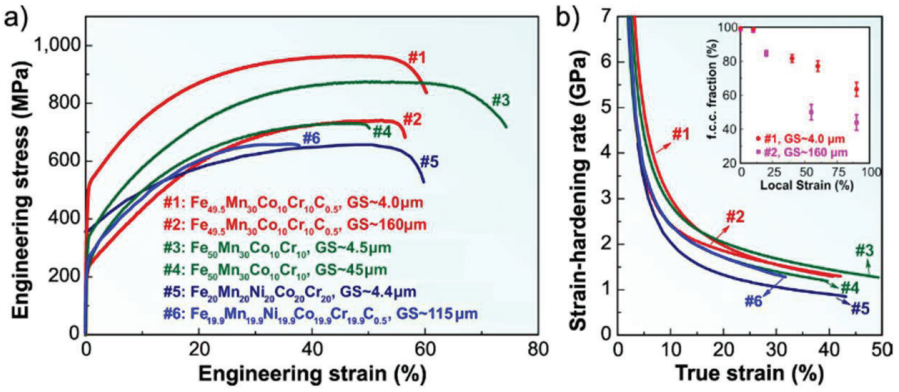

Figure 3-3: Mechanical behavior of the HEAs with TRIP effect (#1-#4) and single-phase (#5-#6). GS refers to the grain size. (a) Engineering stress-strain curves, (b) Strain-hardening for the same group of alloys. The inset shows the increased stability of the FCC phase upon grain refinement. Adapted from Ref. [109].

3.4 Hydrogen embrittlement in high-entropy alloys

Due to the novelty of HEA design concept with a short period of research, there is no comprehensive HE study on HEAs. Up to now, most of the HE studies on HEAs were performed on classic CoCrFeMnNi alloy with interesting observations and conclusions. Luo et al. [113] performed in-situ tensile tests on samples with different amount of pre-charged hydrogen. They reported that the dissolved hydrogen with a content of 8.01-33.25 wppm increases both the strength

and ductility rather than causing catastrophic HE failure. The reason was proposed as that hydrogen can tune the alloy's SFE and phase stability. Therefore, the density of nano-twin is increased during plastic deformation leading to an enhanced work hardening capability and thus both strength and ductility. Zhao et al. [114] also reported a high HE resistance on the same HEA from tensile tests on pre-charged samples. Specifically, the sample was charged with 76.5 wppm hydrogen by high pressure gas (15 MPa) at 300 °C for 72 h. The results showed only 5% ductility loss compared with uncharged sample, and the yield strength, flow stress, or statin hardening rate were not affected by hydrogen. Also, the fracture surface of charged and uncharged samples were similar, both exhibited pure ductile fracture surface with fully-covered dimples. This excellent resistance to HE property on CoCrFeMnNi alloy was also reported by other researchers [115, 116]. However, different observation showing catastrophic hydrogen-induced failure was reported by Nygren et al. [117], who charged massive hydrogen (146.9 wppm) into the same alloy from high temperature gas. By performing tensile tests, the results showed a significant ductility reduction and the fracture mode changed from ductile microvoid coalescence to brittle intergranular failure. Two reasons can explain this different HE behavior: the hydrogen content and the strain rate. The hydrogen contents in the first two studies were much lower compared to 146.9 wppm in the third study. The lower amount of hydrogen might be insufficient to cause the HE failure. Additionally, the strain rates in the first two studies were 10^{-4} and 1.67×10^{-4} s^{-1}, respectively, which were much faster than the 1.7×10^{-6} s^{-1} used in the third study. As discussed in section 3.2 the susceptibility of HE is generally greater for decreasing strain rates. Up to now, it is generally agreed that this alloy shows good resistance to HE at relatively low hydrogen concentration, while it can suffer from embrittlement when applied to high hydrogen content environments.

In addition to the aforementioned HE studies on HEAs, other hydrogen-related studies with a different focus have also been reported. The HE susceptibility of CoCrFeMnNi HEA with interstitial carbon was studied by Luo et al. [18] through low strain rate tensile tests with in-situ hydrogen charging. The results showed a significant hydrogen-induced ductility reduction with only 5.65 wppm dissolved hydrogen. The failure mode in presence of hydrogen combines both intergranular and transgranular fracture as well as microvoid coalescence. Aggregated nano-carbides were observed in the vicinity of cracking and were proposed as potential sites for crack initiation, causing the susceptibility to HE. The correlation between hydrogen and nanohardness

was studied by carrying out nanoindentation test on hydrogen pre-charged CoCrFeMnNi HEA [114]. The hardness increased upon hydrogen charging and it decreased gradually during subsequent aging process, which ended up with a softening effect. The hydrogen-enhanced hardness upon charging was due to hydrogen promoted interstitial solid solution strengthening. The softening behavior was proposed as a result of hydrogen-induced superabundant vacancy formation. The intergranular brittle fracture was also observed on the four-element FeNiCoCr HEA by Nygren et al. [118] through slow strain rate tensile tests on samples charged with 58.5 wppm hydrogen. It shows that the movement of hydrogen by mobile dislocations redistributes hydrogen, which results in a continual evolution of hydrogen concentration on grain boundaries, making the grain boundaries as the most vulnerable sites to HE.

4 Nanoindentation and scanning probe microscopy

4.1 Generalities

Nanoindentation is a testing technique used for investigating properties of small volumes and thin films. It was originally designed as a hardness measurement tool focusing on the micro or nano-scale due to the today's driving for smaller and smaller materials such as chips. Nowadays, the well-developed instrumented nanoindentation is also capable of testing a range of mechanical properties such as elastic modulus, creep, fatigue, and scratch resistance. During nanoindentation, a sharp indenter is brought into contact with a sample under a controlled force or displacement as shown in Figure 4-1(a), which are continuously measured with high resolution sensors and transducers. The force resolution is in the order of μN and the displacement resolution is in the order of nm, both of which are continuously recorded during the test and provide a load-displacement curve. A typical load-displacement curve for a ductile metal with well-prepared surface is shown in Figure 4-1(b), which consists of four regions: elastic loading, pop-in as an excursion in depth, subsequent elasto-plastic loading, and elastic unloading. Each of these parts describes different intrinsic properties of the tested material [119]. For example, the elastic loading and unloading parts are generally used to calculate the reduced modulus, the pop-in indicates the homogeneous dislocation nucleation, phase transformation or a crack formation, the elastoplastic part describes a continuously hardening process, which will be discussed into details in the following sections.

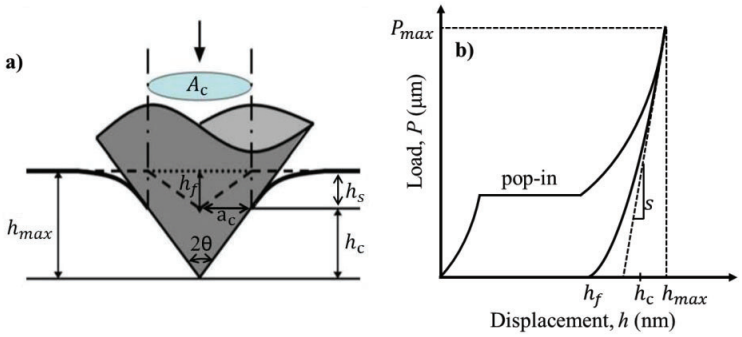

Figure 4-1: a) Schematic of an indentation test at maximum load. b) Schematic of the load-displacement curve. h_{max} and h_c is the maximum depth and tip-sample contact depth, respectively, at maximum load P_{max}. h_f is the final indented depth after the tip has been removed, h_s is the displacement between the surface and contact point. S is the stiffness defined as the slope at the beginning of unloading.

The scanning probe microscopy (SPM) is a tool used for studying the surfaces and structures at the micro- or nano-scale. The SPM forms surface topography by using a sharp physical probe to scan back and forth over the sample surface with a force on the order of μN. The probe is mounted on the end of a cantilever or connected with a sensitive spring system, which sends data containing contact information between tip and sample surface back to computer. Thereby a two-dimensional image of surface topography is generated. The SPM works differently than the optical microscopies by "feeling" the surface instead of directly "seeing" it. By using an extremely sharp probe (3-20 nm), it can reach to a resolution of sub nanometer or even able to individually detect the surface atom by atom. In terms of HE studies, SPM can directly reflect the surface degradation and phase transformation when combined with in-situ hydrogen charging. Also, SPM is able to evaluate the surface quality of sample according to the surface roughness and to determine whether it is suitable to perform reliable nanoindentation test. Because the mechanical properties from nanoindentation test are based on an assumed perfectly flat surface and a surface roughness even with tens of nm change can drastically interfere in the results. For example, the indenter can reach a peak or valley on sample with a high surface roughness. As a result, the hardness will be underestimated if the indenter contacts with a peak, which causes an intensively localized stress and leads to a deeper penetration with a given load. While the hardness will be overestimated if the indenter contacts with a valley, which leads to a bigger contact area and smaller plastic deformation. The International Standard Organization (ISO 14577-4) suggests that the surface roughness should be less than 5% of the maximum penetration depth to ensure the accuracy of measurement [120].

4.2 Contact mechanics

Contact mechanics is the study of deformation of solids that touch each other with an interaction force at one or more points [121]. Basic contact mechanics should be known to understand the nanoindentation process, which is a special case of bringing two solid bodies into contact: one is the stiff indenter and the other one is the specimen to be tested. The contact mechanics have been studied for more than 100 years with several popular theories. Hertz proposed a theory focusing on the contact between a rigid spherical indenter and a flat elastic isotropic half-space [122], Boussinesq studied the contact of a rigid cylindrical flat indenter onto an elastic half-space [123],

and Sneddon further extended the theory applying to a rigid conical indenter [124]. The Hertz contact and Sneddon contact will be introduced in the following, since they are more related to the nanoindentation process in this thesis.

The Hertz theory was built on the following assumptions: the contact surfaces are continuous and non-conforming, the strains are small, solids are pure elastic, and the surfaces are frictionless [122]. Therefore, it can be used to describe the elastic part of nanoindentation process and qualify the contact area, contact compression pressure, and the induced stress to specimen. Hertz determined the contact area radius a_c (as shown in Figure 4-1(a)) as:

$$a_c = \sqrt[3]{\frac{3}{4}\frac{PR}{E_r}} \tag{4.1}$$

where the P is the load, R is the radius of the indenter, and E_r is the reduced modulus. E_r represents the elastic deformation that occurs in both specimen and indenter, and it can be represented by:

$$\frac{1}{E_r} = \frac{1-\nu_1^2}{E_1} + \frac{1-\nu_2^2}{E_2} \tag{4.2}$$

Here, the E indicates the elastic modulus and ν is the Poisson's ratio, the subscripts 1 and 2 represent the specimen and the tip, respectively. The indenters are generally made of diamond, which has an elastic modulus of 1140 GPa and a Poisson's ratio of 0.07. In addition, the Hertz theory also describes the indentation depth as the following equation:

$$h = \left(\frac{3}{4E_r}\right)^2 \frac{P^2}{R} \tag{4.3}$$

By converting the Eq. 4.3, the applied load can be described as a function of indentation depth by:

$$P = \frac{4}{3}E_r\sqrt{Rh^3} \tag{4.4}$$

Therefore, if the radius of indenter tip is known, one can get the E_r value of specimen by fitting the elastic loading part of the load-displacement curve with the Hertzian model in Eq. 4.4. After further calculation based on Eq. 4.2, the elastic modulus of tested specimen can be easily obtained.

The Sneddon model describes the frictionless indentation by a rigid conical indenter with an angle of 2θ on an isotropic elastic half-space as a function of the applied force and indentation depth [124]. The applied load P is shown in Eq. 4.5 and the indentation depth h is described in Eq. 4.6.

$$P = \frac{\pi a_c}{2} E_r a_c \cot\theta \tag{4.5}$$

$$h = \frac{\pi}{2} a_c \cot\theta \tag{4.6}$$

Here, a_c is the contact area radius defined in Eq. 4.1. By combining Eqs. 4.5 and 4.6 and eliminating a_c, the applied load can be rewritten as a function of indentation depth as follows:

$$P = \frac{\pi}{2} E_r h^2 \tan\theta \tag{4.7}$$

The contact stiffness S can be calculated as the slope at the beginning of unloading:

$$S = \frac{dP}{dh} = 2E_r \sqrt{\frac{A_c}{\pi}} \tag{4.8}$$

where A_c is the projected contact area defined as πa_c^2. Therefore, the reduced modulus can be rewritten as:

$$E_r = \frac{S}{2} \sqrt{\frac{\pi}{A_c}} \tag{4.9}$$

The Sneddon model gives an idea to calculate reduced modulus from the stiffness. However, this model is only suitable for an indenter with perfect rigid cone shape. This model was further improved by Oliver and Pharr, who fitted the upper portion of unloading part of load-displacement curve with a power-law equation and made the Sneddon equation be adaptable to different shaped indenters [119]. The reduced modules E_r is defined according to the Oliver and Pharr model as:

$$E_r = \frac{S}{2\beta} \sqrt{\frac{\pi}{A_c}} \tag{4.10}$$

Here β is the geometric correction factor, which was proposed as 1.034 for triangle-based indenter such as Berkovich, and 1.012 for a square-based indenter such as cube corner.

4.2.1 Reduced modulus

Young's modulus is one of the most commonly concerned material properties and it shows the tendency of an object to deform along an axis with applied force. It can be easily determined by nanoindentation test through the measurement of reduced modulus E_r . Based on the aforementioned contact mechanics, the reduced modulus E_r can be obtained from the load-displacement curves by either fitting the initial elastic loading part with the Hertzian model (Eq. 4.4), or calculating from the stiffness value of unloading curve based on the Oliver-Pharr method (Eq. 4.10). In terms of Oliver-Pharr method, it needs to pay attention on determining the projected contact area A_c, which relates to both the indenter contact depth and the indenter area function. The contact depth indicates the vertical distance along the contact. As shown in Figure 4-1(a), the contact depth h_c was proposed by Oliver and Pharr as [119]:

$$h_c = h_{max} - \in \frac{P_{max}}{S} \tag{4.11}$$

Here, the h_{max} and P_{max} indicate the maximum indentation depth and maximum applied load, respectively. The $\in$ is a constant that depends on the indenter geometry. $\in$ is 0.72 for conical indenter and 0.75 for Berkovich indenter. The area function defines the relation between the contact area $A(h_c)$ and contact depth h_c. It is generally described by a sixth order polynomial equation as:

$$A(h_c) = C_0 h_c^2 + C_1 h_c + C_2 h_c^{1/2} + C_3 h_c^{1/4} + C_4 h_c^{1/8} + C_5 h_c^{1/16} \tag{4.12}$$

C_0 is 24.5 for Berkovich indenters and is 2.598 for a cube corner indenters. C_1 to C_5 are determined by performing a series of indenting with various contact depth on fused quartz, which has a fixed and known reduced modulus and hardness. These indentation curves will be further fitted one by one with Eq. 4.12 to estimate the coefficient values. With a qualified area function, the reduced modulus thereby can be precisely calculated by using the Oliver-Pharr method shown in Eq. 4.10.

4.2.2 Hardness

Hardness describes the resistance to permanent deformation of a material. It is defined as the maximum applied load P_{max} divided by the corresponding contact area A_c:

$$H = \frac{P_{max}}{A_c} \tag{4.13}$$

The P_{max} can be directly obtained from the load-displacement curve, and the A_c can by calculated as a function of contact depth by Eq. 4.12.

However, for the nanoindentation test with a maximum indentation depth less than 5 μm, metallic materials exhibit an increasing hardness value with decreasing indentation depth [125], as shown in Figure 4-2. This is known as indentation size effect. The size effect is proposed by Nix and Gao as a result of geometrically necessary dislocations (GNDs) induced by imposed strain gradients [126]. By using the Taylor relation, Nix-Gao model connects the size effect with GNDs, which have a density proportional to the inverse of indentation depth. Further, the measured hardness as a function of indentation depth can be described as:

$$H^2 = H_0^2 \left(1 + \frac{h_0}{h}\right) \tag{4.14}$$

Here H is the measured hardness value, H_0 is the hardness value in ideal condition without any GNDs, h_0 is a length scale related to H_0, and h is the indentation depth. Eq. 4.14 shows a linear relationship between H^2 and h^{-1}, indicating the size effect. It needs to mention here that the Nix-Gao model assumed that all the GNDs are stored in plastic zone, which has a radius equal to the contact area radius. However, the actual plastic zone should have a larger radius than the contact radius due to the repulsive force between GNDs. This means the hardness from Nix-Gao model is overestimated and it has been further improved by other works in ref. [127-129].

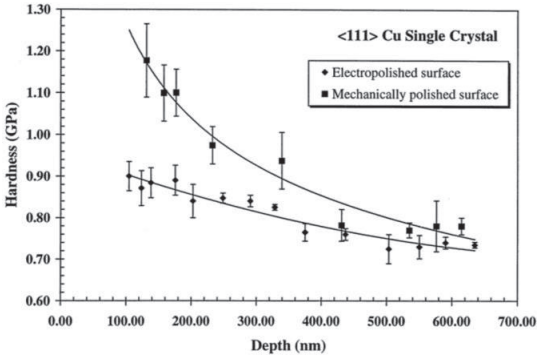

Figure 4-2: Depth dependent hardness on single crystal of copper. Adapted from Ref. [130]

4.2.3 Pop-in

The pop-in phenomenon during nanoindentation tests is often observed on crystalline materials as a sudden displacement burst as shown in Figure 4-1(b) [131-134]. For an annealed sample without oxide layer on a well-prepared surface, the pop-in effect indicates the onset of dislocation nucleation [135, 136]. Other possibilities are also able to induce a pop-in phenomenon such as the rupture of a hard brittle surface film, the strain transfer across grain boundaries, crack formation, and phase transformation [137-139]. Since none of these is the case in the current study, they are out of the discussion scope in this thesis. For all the nanoindentation tests in this thesis, the pop-in happens after elastic loading and followed by elastoplastic loading. This means that the observed pop-in is a discrete transition from elastic to plastic deformation due to homogeneous nucleation of dislocation loops. The term "homogeneous" is used here to indicate that the dislocations are nucleated from a dislocation-free area [22]. According to the continuum mechanics, the maximum shear stress during an indentation test is reached below the sample surface with a depth equal to $0.48a_c$. a_c is the contact radius that proposed in Eq. 4.1 [121]. The value and the depth of maximum shear stress τ_{max} and $Z_{\tau_{max}}$ are given by:

$$\tau_{max} = 0.31\left(\frac{6PE_r^2}{\pi^3 R^2}\right)^{\frac{1}{3}} \tag{4.15}$$

$$Z_{\tau_{max}} = 0.48\left(\frac{3PR}{4E_r}\right)^{\frac{1}{3}} \tag{4.16}$$

According to the Frenkel's model [140], the theoretical shear strength is proposed as a fraction of the shear modulus (μ) in the range between μ/20 and μ/10. Therefore, the pop-in can be interpreted as homogeneous nucleation of dislocation when maximum shear stress τ_{max} underneath the indenter reaches to the theoretical shear strength of the material.

5 Experimental

5.1 Materials and sample preparation

There are two groups of materials studied in this PhD thesis. One is high-Mn TWIP steel with the composition of Fe-22Mn-0.6C (wt.%), the other one is HEA with stable state of 20Co-20Cr-20Fe-20Mn-20Ni (at.%) and metastable state of Fe-30Mn-10Co-10Cr-0.5C (at.%).

The TWIP steel has been melted in laboratory, ingot casted, hot rolled, and cold rolled to a thickness of 1.0 mm, followed by grain growth annealing at 1150 °C for 5 h in Ar atmosphere. The two HEAs were cast in a vacuum induction furnace by using ultra-clean metals with a purity higher than 99.8 wt.%. The as-cast alloy sheets were hot rolled at 900 °C with 50% thickness reduction, homogenized at 1200 °C for 2 h in an Ar atmosphere followed by water quenching. The tested specimens were further cut by electrical charge machining into desired shapes. The specimens were ground sequentially by using 220-4000 grit SiC papers, followed by two polishing steps with 3 and 1 μm diamond sprays. For TWIP steel, the surface preparation was finalized by 20 min polishing with 40 nm colloidal silica suspension to remove the deformation layer. While electropolishing in a methanol/H_2SO_4 solution was performed on HEAs as the final surface preparation step. The prepared surface was then checked by SPM with a surface root-mean-square roughness to be less than 1 nm over 64 μm^2.

The microstructure of these specimens was further analyzed by electron microscopy (more details in section 5.4). All the samples exhibit a single FCC structure consisting of equiaxed grains with annealing twins as shown in the normal direction-inverse pole figure (ND-IPF) maps in Figure 5-1. The grain size is 85, 160, and 120 μm for TWIP steel, stable and metastable HEAs, respectively.

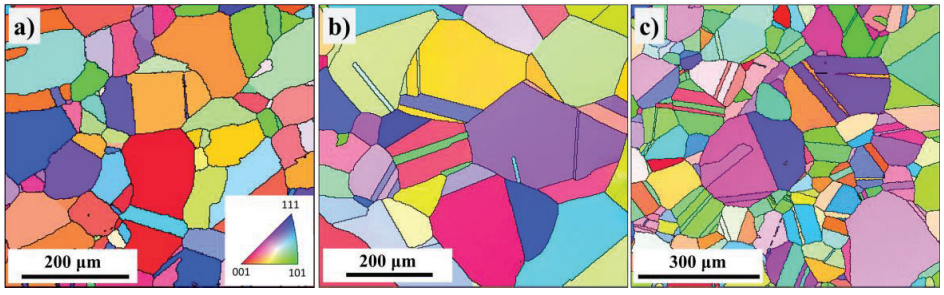

Figure 5-1: ND-IPF maps showing the microstructure of (a) TWIP steel, (b) stable HEA, and (c) metastable HEA.

5.2 Electrochemical hydrogen charging

The hydrogen charging electrolyte used in this thesis is a glycerol-based solution, which consists of 600 g borax (sodium tetraborate decahydrate) dissolved into 1 L glycerol. In addition, 20 vol.% distilled water with 0.002 M $Na_2S_2O_3$ (sodium thiosulfate) is added to ensure the conductivity and promote hydrogen absorption [141]. This electrolyte has the advantage to protect specimen surface from corrosion throughout the whole test due to its extremely low oxygen solubility and diffusivity [142], making it possible to directly perform the following in-situ tests without further surface preparation.

Regarding to the specimens for tensile test, the hydrogen pre-charging was carried out by using a standard electrochemical cell, which consists of a Pt net as counter electrode and Ag/AgCl reference electrode. The hydrogen charging was performed at 80 °C with a constant cathodic potential of -1400 mV (~10 mA/cm^2). Three different charging times of 50, 150, and 300 h were applied. While for specimens used for nanoindentation test, in-situ hydrogen charging was performed at room temperature inside a specially designed electrochemical cell consisting of a Pt counter electrode and $Hg/HgSO_4$ reference electrode (more details in 5.3.2). During the test, different cathodic hydrogen charging potentials and anodic hydrogen discharging potential were applied. The charging/discharging potentials were determined from the polarization curve, which was scanned by using the same electrochemical system from -2500 to 1500 mV with a scan rate of 1 mV/s. The different charging potentials were chosen from cathodic branch indicate different surface hydrogen concentrations, while anodic discharging potential was chosen from passive region to egress dissolved diffusible hydrogen and also minimize the surface degradation.

5.3 In-situ testing

5.3.1 In-situ tensile testing

The tensile tests with in-situ scanning electron microscope (SEM) observation were performed on pre-charged TWIP steels. The specimens were machined into a two-step dog-bone shape with gauge geometry of 5 mm × 2 mm × 1 mm as shown in Figure 5-2. The tensile tests were carried out by using a Kammrath & Weiss tensile/compression module, which was installed inside the SEM chamber for in-situ observation. The engineering strain rate was chosen as 4×10^{-5} s^{-1}. Two

groups of TWIP specimens were tested under tensile tests: for the first group, the specimens were loaded until fracture happened, in order to determine the overall hydrogen effect on mechanical properties and fracture mode. For the second group, the tests were stopped at 10% elongation to analyze the initiation and propagation of secondary cracks on gauge surface. Each group contains four specimens with 0, 50, 150, and 300 h pre-charged hydrogen. The dwell time between the finish of hydrogen charging and the start of tensile tests was kept less than 5 min to minimize the hydrogen loss during this period.

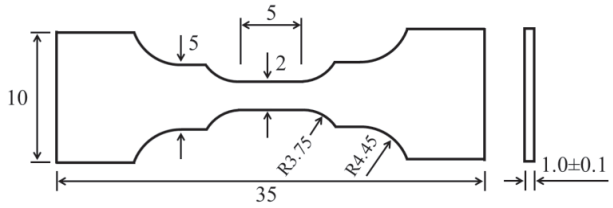

Figure 5-2: Geometry of specimen for tensile test (in mm).

5.3.2 In-situ nanoindentation testing

Both TWIP steel and two types of HEAs were examined by nanoindentation and SPM tests with in-situ hydrogen charging. The nanoindentation test was carried out by using a Hysitron Tribo-indenter TI 950 equipped with a long-shaft Berkovich tip, which was used for both indenting and SPM imaging. The setup for in-situ nanoindentation is shown in Figure 5-3(a) and the load function is shown in Figure 5-3(b). The load function starts with a loading segment of 8000 μN/s loading rate until the peak load of 2000 μN is reached plus a 0.45 s holding time, then an 8000 μN/s unloading segment is followed with an additional 0.25 s holding time at the 10% of peak load for drift correction. For each polarization condition, at least three groups of indents (nine indents for each group) were performed to guarantee the reproducibility of results. The SPM images were scanned after each group of indentation test with a size of 15×15 μm^2. The scan force was 2 μN, the scan rate was 1.5 Hz, and the scan resolution was 1024×1024. The scanned SPM images were further analyzed with Gwyddion software to obtain the morphology information.

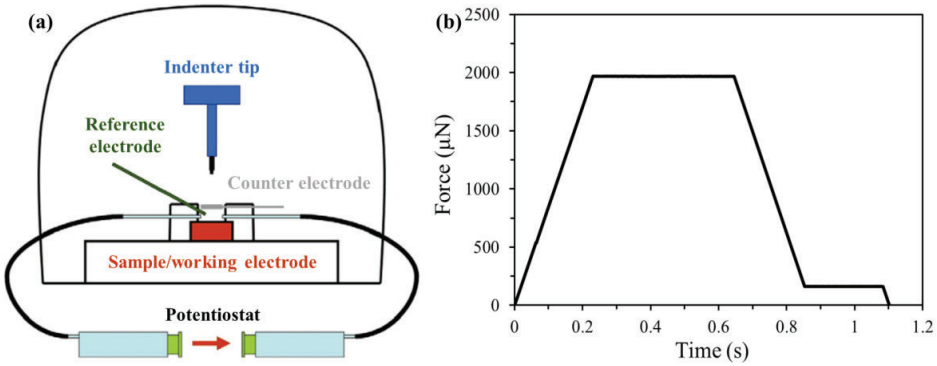

Figure 5-3: (a) Schematic drawing of the in-situ nanoindentation test setup. (b) The load function for nanoindentation test.

5.4 Post-mortem analysis

Scanning electron microscopy and Electron backscatter diffraction

The SEM used in this thesis was a high-resolution Quanta 650 FEG model (Thermo Fisher Scientific Inc.), which was used for in-situ tensile test observation and also surface microstructure analysis. In addition, the SEM was installed with a backscatter electron (BSE) detector and a phosphor screen, which enable the BSE imaging and the electron backscatter diffraction (EBSD) characterization, respectively. The EBSD technique was used for microstructure analysis, phase determination, and orientation analysis. During the EBSD characterization, the diffraction patterns were acquired by a NORDIF detector and further indexed and analyzed by the OIM software.

Electron channeling contrast imaging

Electron channeling contrast imaging (ECCI) has been proven as an excellent SEM technique based on the strong dependence of the backscatter electron intensity on the orientation of crystal lattice planes with respect to the incident electron beam due to the electron channeling mechanism [82, 143]. In this thesis, the ECC imaging was performed at 30 kV acceleration voltage with approximately 6.5 mm working distance by using the same SEM facility equipped with a solid-state four-quadrant backscatter electron detector. By tilting the specimen to a certain angle, where the grain matrix is under Bragg condition, an optimum channeling contrast can be obtained,

making it possible to directly observe the lattice defects such as dislocations and stacking faults within the depth of tens of nanometers. In the ECC images, the dislocations appear as white curved lines or dots on the dark background due to the interaction between dislocations with sample surface, while the stacking faults appear as bright areas with a white straight line on one side, indicating the interaction between the stacking fault plane and the sample surface [143].

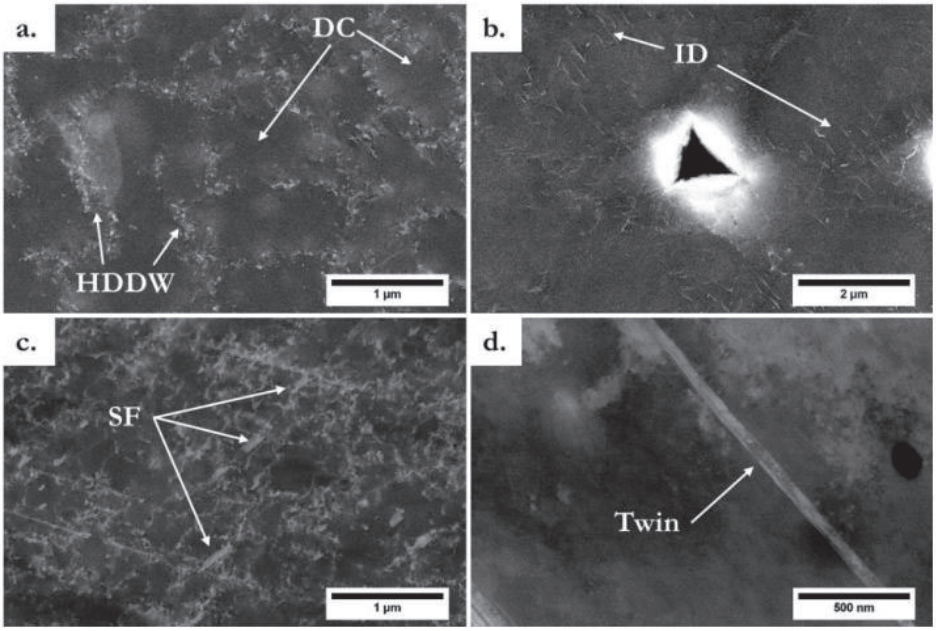

Figure 5-4: Examples of ECC images. (a) highly-densed dislocation walls (HDDW) and dislocation cells (DC). (b) individual dislocations (c) stacking faults (SFs) accompanying dislocations in a deformed 304 stainless. (d) a nano-scaled twin. Adopted from Ref. [144]

Thermal desorption spectroscopy

The content of absorbed hydrogen at desired condition was determined by the thermal desorption spectroscopy (TDS) test. The TDS measurement was carried out immediately after each polarization condition with a dwell time less than 5 min to eliminate the hydrogen outgassing effect. In this thesis, the TDS test was performed by using a Bruker G4 Phoenix DH hydrogen analyzer in combination with an ESD 100 mass spectrometry detector setup (InProcess Instruments, Germany) under the environment of pure N_2 as the carrier gas. The heating rate was 25 °C/min from 25 °C to 700 °C.

X-ray diffraction

X-ray diffraction (XRD) is a rapid analytical technique to identify the phase of a crystalline material. In this thesis, XRD was performed to determine the phase transformation induced by cathodic hydrogen charging. Due to the fact that only the specimen surface within several micrometer suffered from phase transformation owing to the short charging time and low hydrogen diffusivity, XRD with grazing incident mode (GIXRD) was carried out to intensify the signal from surface layer and minimize the disturbed signal from substrate. The GIXRD (D8 DaVinci with LynxEye™ Superspeed detector) was operated by using Cu Kα radiation (40 kV, 40 mA) at 0.75° incident angle. The step size was 0.02° and a counting time of 4.8 s was applied for each step.

Focused ion beam and transmission Kikuchi diffraction

To determine the depth of phase transformation after hydrogen charging, a novel transmission Kikuchi diffraction (TKD) was performed on a thin sample cut from the hydrogen charged specimen. The thin sample was cut by using the focused ion beam (FIB, Helios Dual Beam, Thermo Fisher Scientific Inc., USA) from the specimen surface to a depth of 5 μm and then milled from both sides to reduce the thickness to approximately 100 nm. During the FIB milling process, different steps with current from 2.8 nA down to 10 pA was applied to ensure a smooth surface, also carbon deposition was applied on surface to protect from Ga ion induced FIB damage. The TKD technique is also known as transmission-EBSD. For the traditional EBSD, the signal is produced by back scattering diffracted electrons escaping from a 70° tilted bulk sample. While the TKD technique captures the Kikuchi pattern signal from an electron transparent sample with a small source volume, which improves the spatial resolution from 20 nm in EBSD down to 2 nm [145, 146]. In the current thesis, the TKD was performed by using the same Quanta 650 FEG SEM with a voltage of 30 kV and a step size of 10 nm. The sample was tilted to 20° to the electron beam direction. The transmission Kikuchi signal were acquired by a NORDIF detector and further indexed and analyzed by the OIM data collection and analysis software.

6 Summary of papers

This section contains a short introduction of the papers that have been published or prepared during the PhD period. The full manuscripts are attached as the **Part II** of this thesis.

Paper I: Effect of hydrogen on the embrittlement susceptibility of Fe-22Mn-0.6C TWIP steel revealed by in-situ tensile tests, Submitted

Abstract: We investigated the hydrogen embrittlement on a Fe-22Mn-0.6C twinning-induced plasticity steel by tensile tests with in-situ scanning electron microscope observation, plus electron backscatter diffraction and electron channeling contrast imaging techniques. The tensile tests were performed on specimens with 0, 50, 150, and 300 hours pre-charged hydrogen, which accumulatively reduced the mechanical properties and induced a ductile-to-brittle fracture transition. The threshold of hydrogen content to trigger this ductile-to-brittle transition was further determined. During the tensile tests, intergranular secondary cracks were observed on gauge surface of specimens with pre-charged hydrogen. The low angle grain boundaries exhibited better resistance to both crack initiation and propagation compared with high angle grain boundaries. In addition, the stress concentration together with the hydrogen effect on grain boundaries intersecting with deformation twins are proposed as the reasons for the crack initiation and propagation.

Keywords: Twinning-induced plasticity (TWIP) steel; Hydrogen embrittlement; Deformation twinning; Secondary cracks; Electron channeling contrast imaging (ECCI).

6. Summary of papers

Paper II: Effect of hydrogen on nanomechanical properties in Fe-22Mn-0.6C TWIP steel revealed by in-situ electrochemical nanoindentation, Acta Mater. 166 (2019) 618-629.

Dong Wang, Xu Lu, Yun Deng, Xiaofei Guo, Afrooz Barnoush

Abstract: In-situ electrochemical nanoindentation was applied to study the effect of hydrogen on the mechanical properties of Fe-22Mn-0.6C TWIP steel at the nanoscale. Distinctive behaviors in three defined grain orientations: (001), (101), and (111) were investigated in a sequence of air, hydrogen ingress, and hydrogen egress processes. The obvious pop-in load drop caused by introducing hydrogen was analyzed using the classical dislocation theory in combination with the "Defactants" model, wherein hydrogen-enhanced homogenous dislocation nucleation through the reduction of the dislocation line energy and the stacking fault energy were proposed as the reasons. The dependence of pop-in behaviors on the crystallographic orientations was also discussed. Tabor relation-based models were applied to analyze the nanohardness increment, which was related to the hydrogen-enhanced lattice friction and the hydrogen-reduced plastic zone size. The different recovery behaviors of the pop-in load and nanohardness during hydrogen egress were assessed according to the different amounts of residual hydrogen in the corresponding affected zone.

Keywords: Hydrogen embrittlement; Electrochemical nanoindentation; TWIP steel; Dislocation nucleation; Nanohardness.

Graphical Abstract:

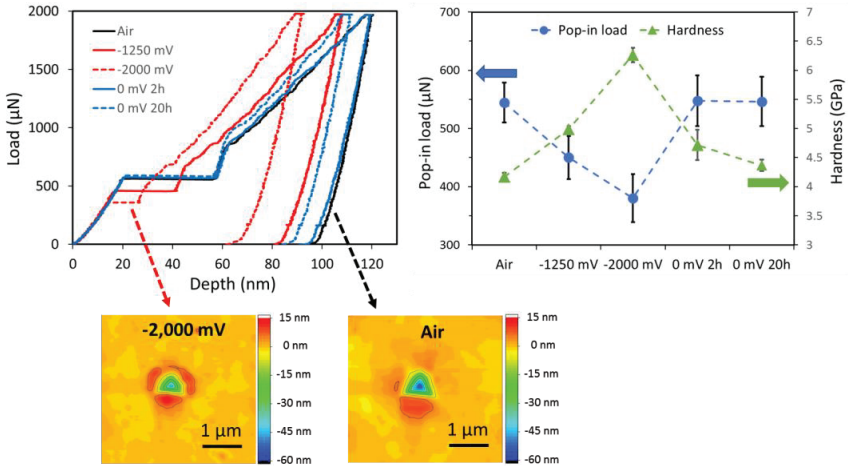

Paper III: In-situ observation of martensitic transformation in an interstitial metastable high-entropy alloy during cathodic hydrogen charging, Scr. Mater. 173 (2019) 56-60.

Dong Wang, Xu Lu, Di Wan, Zhiming Li, Afrooz Barnoush

Abstract: We show for the first time that a critical amount of dissolved hydrogen can induce a phase transformation from γ-austenite to ε-martensite in an interstitial metastable high-entropy alloy. This is demonstrated by in-situ hydrogen charging in combination with nanoindentation and scanning probe microscopy, plus further electron channeling contrast imaging, X-ray diffraction, and transmission Kikuchi diffraction techniques. The transformed martensites appear as bands on the surface along γ-{111} habit planes, leading to an irreversible increase of hardness. The hydrogen-induced internal stress together with the intrinsic hydrogen effects are proposed to be responsible for the martensitic transformation upon hydrogen charging.

Keywords: Hydrogen; High-entropy alloy; Martensitic transformation; In-situ electrochemical nanoindentation; Transmission Kikuchi diffraction.

Graphical Abstract:

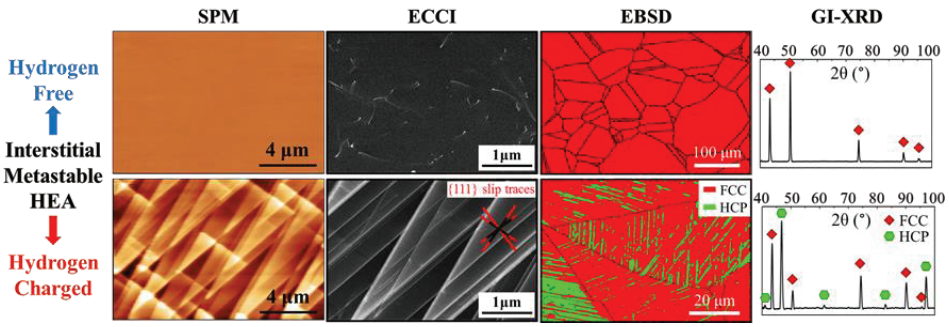

6. Summary of papers

Paper IV: Effect of hydrogen-induced surface steps on the nanomechanical behavior of a CoCrFeMnNi high-entropy alloy revealed by in-situ electrochemical nanoindentation, Intermetallics 114 (2019) 106605.

Dong Wang, Xu Lu, Yun Deng, Di Wan, Zhiming Li, Afrooz Barnoush

Abstract: The effect of hydrogen on the nanomechanical properties of CoCrFeMnNi high-entropy alloy was investigated by in-situ electrochemical nanoindentation testing. The changes in surface morphology, elastic modulus, pop-in load, and hardness during hydrogen ingress and egress processes were systematically evaluated. The results show that hydrogen charging leads to the formation of irreversible slip lines accumulated as surface steps. Furthermore, the irreversible reduced pop-in load and elastic modulus, and reversible increased hardness are detected. In this paper, the mechanisms of hydrogen-induced surface steps together with their further influences on the nanomechanical properties are discussed in detail.

Keywords: In-situ electrochemical nanoindentation; High-entropy alloy; Hydrogen embrittlement; Hydrogen-induced surface steps; Electron channeling contrast imaging; Nanomechanical.

Graphical Abstract:

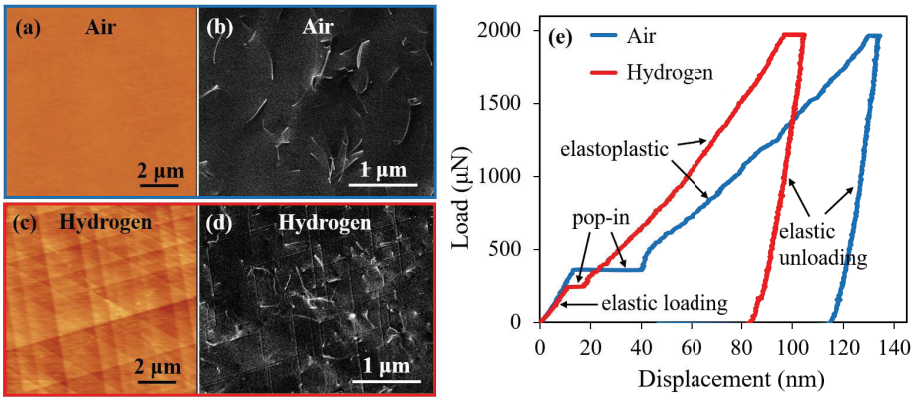

(a)-(b) SPM and ECC images of sample surface in air condition. (c)-(d) SPM and ECC images of sample surface after cathodic hydrogen charging. (e) The load-displacement curves in different conditions showing the influence of hydrogen charging on the nanomechanical properties.

7 Conclusion and Outlook

To sum up, the present PhD work comprehensively studied the interaction between hydrogen and plasticity in high strength alloys by using novel in-situ techniques. Multi-scale testing methods were applied from small-scale in-situ tensile test to nano-scale in-situ indentation test. Some major conclusions can be drawn as follows:

1) The presence of hydrogen has a strong detrimental effect on both the tensile strength and fracture elongation on the studied TWIP steel. The fracture surface shows a ductile-to-brittle transition with the charged hydrogen. Moreover, the different amount of charged hydrogen shows an accumulatively effect on the mechanical property degradation and leads to a deeper ductile-to-brittle transition depth. A specific amount of hydrogen can be determined as the threshold value for this ductile-to-brittle transition.
2) During the tensile tests on TWIP steel, the secondary intergranular cracks on gauge surface were detected on the hydrogen-charged specimens. The amount and area occupation of secondary cracks increased as the increasing of charging time and tensile elongation. Moreover, it shows that the grain boundaries intersecting with thick deformation twins and close to perpendicular angle are the preferential crack initiation sites and propagation paths. This is due to the stress concentration at these intersecting points in combination with the intrinsic hydrogen effect on grain boundaries.
3) From the in-situ nanoindentation test on TWIP steel, the pop-in load was continuously reduced and the hardness value was continuously increased with the amount of charged hydrogen. The hydrogen reduced pop-in load is caused by the hydrogen-enhanced homogeneous dislocation nucleation through the reduction of dislocation line energy and stacking fault energy. The hydrogen enhanced hardness value is related to hydrogen-enhanced lattice friction and retard the mobility of dislocation. Moreover, the pop-in load and hardness have different affecting depths, where the amount of dissolved hydrogen determines the corresponding intensity of hydrogen effect.
4) The influence of hydrogen charging alone on the microstructure stability was studied on two HEAs with metastable and stable phases properties. The results show that cathodic hydrogen charging with a critical charging current density can lead to γ-austenite to ε-martensite phase transformation on metastable HEA and also lead to the formation of

irreversible slip lines accumulated as surface steps on stable HEA. The phase transformation and surface step formation were proposed as the result of hydrogen charging induced internal stress together with the intrinsic hydrogen effect on SFE reduction and superabundant vacancies formation.

5) To the best of our knowledge, the hydrogen charging alone induced martensite phase transformation and surface step formation on the studied HEAs have not been observed and discussed before. It will be necessary to consider this effect in future studies on hydrogen embrittlement and design of hydrogen-tolerant alloys.

However, due to the time and technical limitations, some works unfortunately could not be performed and realized in the presented PhD study. Some of the outlooks and future works are listed as follows:

1) As we observed in the in-situ tensile tests on TWIP steel, the grain boundaries are the most vulnerable sites for hydrogen embrittlement, resulting in intergranular secondary cracks on the gauge surface during deformation. However, the following in-situ nanoindentation test focused on the hydrogen effect inside of specific grains, which is not enough to reveal the macroscopic hydrogen embrittlement on the studied material. Therefore, further studies focusing on the grain boundary behavior need to be performed. This can be achieved by performing cantilever bending test with a notch on grain boundary and bi-pillar compression test with a grain boundary in between.
2) We observed the γ-austenite to ε-martensite phase transformation by only hydrogen charging on metastable HEA and we accordingly suggested that it is necessary to consider these effects in future studies on hydrogen embrittlement and the design of hydrogen-tolerant alloys. Therefore, the contribution between hydrogen charging induced phase transformation and tensile deformation induced phase transformation need to be quantified by further studies.
3) In this study, we mainly focused on the hydrogen effect on the nanomechanical properties in a relatively small scale. Further studies are needed to establish a relationship between nano-scaled data to the fracture mechanical properties on bulk materials.

8 Reference

[1] P.R. Rhodes, L.A. Skogsberg, R.N. Tuttle, Pushing the Limits of Metals in Corrosive Oil and Gas Well Environments, Corrosion 63(1) (2007) 63-100.
[2] H.C. Rogers, Hydrogen Embrittlement of Metals, Science 159(3819) (1968) 1057-1064.
[3] M. Nagumo, Fundamentals of hydrogen embrittlement, Springer, Singapore, 2016.
[4] W.H. Johnson, On Some Remarkable Changes Produced in Iron and Steel by the Action of Hydrogen and Acids, Proceedings of the Royal Society of London 23 (1874) 168-179.
[5] P. Ferreira, I. Robertson, H. Birnbaum, Hydrogen effects on the interaction between dislocations, Acta Mater. 46(5) (1998) 1749-1757.
[6] Z. Tarzimoghadam, M. Rohwerder, S.V. Merzlikin, A. Bashir, L. Yedra, S. Eswara, D. Ponge, D. Raabe, Multi-scale and spatially resolved hydrogen mapping in a Ni-Nb model alloy reveals the role of the δ phase in hydrogen embrittlement of alloy 718, Acta Mater. 109 (2016) 69-81.
[7] S.P. Lynch, Environmentally Assisted Cracking: Overview of Evidence for an Adsorption-Induced Localized-Slip Process, Acta Metall. 36(10) (1988) 2639-2661.
[8] A. Oudriss, J. Creus, J. Bouhattate, E. Conforto, C. Berziou, C. Savall, X. Feaugas, Grain size and grain-boundary effects on diffusion and trapping of hydrogen in pure nickel, Acta Mater. 60(19) (2012) 6814-6828.
[9] R. Kirchheim, Reducing grain boundary, dislocation line and vacancy formation energies by solute segregation. I. Theoretical background, Acta Mater. 55(15) (2007) 5129-5138.
[10] R. Kirchheim, Reducing grain boundary, dislocation line and vacancy formation energies by solute segregation II. Experimental evidence and consequences, Acta Mater. 55(15) (2007) 5139-5148.
[11] B.C. De Cooman, L. Chen, H.S. Kim, Y. Estrin, S.K. Kim, H. Voswinckel, REVIEW OF THE MECHANICAL PROPERTIES OF HIGH STRENGTH, HIGH-Mn TWIP STEELS FOR AUTOMOTIVE APPLICATIONS, New Developments on Metallurgy and Applications of High Strength Steels: Buenos Aires 2008, Vols 1 and 2, Proceedings, (2008) 69.
[12] Q.L. Liu, Q.J. Zhou, J. Venezuela, M.X. Zhang, J.Q. Wang, A. Atrens, A review of the influence of hydrogen on the mechanical properties of DP, TRIP, and TWIP advanced high-strength steels for auto construction, Corros. Rev. 34(3) (2016) 127-152.
[13] D. Cheddie, Ammonia as a hydrogen source for fuel cells: a review, InTech2012.
[14] N. Zan, H. Ding, X.F. Guo, Z.Y. Tang, W. Bleck, Effects of grain size on hydrogen embrittlement in a Fe-22Mn-0.6C TWIP steel, Int. J. Hydrog. Energy 40(33) (2015) 10687-10696.
[15] B. Bal, M. Koyama, G. Gerstein, H.J. Maier, K. Tsuzaki, Effect of strain rate on hydrogen embrittlement susceptibility of twinning-induced plasticity steel pre-charged with high-pressure hydrogen gas, Int. J. Hydrog. Energy 41(34) (2016) 15362-15372.
[16] O. Barrera, D. Bombac, Y. Chen, T.D. Daff, E. Galindo-Nava, P. Gong, D. Haley, R. Horton, I. Katzarov, J.R. Kermode, C. Liverani, M. Stopher, F. Sweeney, Understanding and mitigating hydrogen embrittlement of steels: a review of experimental, modelling and design progress from atomistic to continuum, J. Mater. Sci. 53(9) (2018) 6251-6290.
[17] M. Koyama, H. Springer, S.V. Merzlikin, K. Tsuzaki, E. Akiyama, D. Raabe, Hydrogen embrittlement associated with strain localization in a precipitation-hardened Fe–Mn–Al–C light weight austenitic steel, Int. J. Hydrog. Energy 39(9) (2014) 4634-4646.
[18] H. Luo, Z.M. Li, W.J. Lu, D. Ponge, D. Raabe, Hydrogen embrittlement of an interstitial equimolar high-entropy alloy, Corros. Sci. 136 (2018) 403-408.

[19] H.G. Nelson, D.P. Williams, J.E. Stein, Environmental hydrogen embrittlement of an α-β titanium alloy: Effect of microstructure, Metallurgical and Materials Transactions B 3(2) (1972) 473-479.
[20] D.G. Chakrapani, E.N. Pugh, Hydrogen embrittlement in a Mg-Al alloy, Metallurgical Transactions A 7(2) (1976) 173-178.
[21] R.J. GEST, A.R. TROIANO, Stress Corrosion and Hydrogen Embrittlement in an Aluminum Alloy, Corrosion 30(8) (1974) 274-279.
[22] A. Barnoush, H. Vehoff, Recent developments in the study of hydrogen embrittlement: Hydrogen effect on dislocation nucleation, Acta Mater. 58(16) (2010) 5274-5285.
[23] I.M. Robertson, P. Sofronis, A. Nagao, M.L. Martin, S. Wang, D.W. Gross, K.E. Nygren, Hydrogen Embrittlement Understood, Metall. Mater. Trans. A 46a(6) (2015) 2323-2341.
[24] A.R. Troiano, R. Gibala, R. Hehemann, Hydrogen embrittlement and stress corrosion cracking: a Troiano Festschrift, ASM International, Ohio, 1984.
[25] H.J. Flitt, J.O.M. Bockris, Hydrogen/metal interactions with special reference to electrochemical approaches, Int. J. Hydrog. Energy 6(2) (1981) 119-138.
[26] S. Lynch, Hydrogen embrittlement phenomena and mechanisms, Corros. Rev. 30(3-4) (2012) 105-123.
[27] J.O.M. Bockris, E.C. Potter, The Mechanism of Hydrogen Evolution at Nickel Cathodes in Aqueous Solutions, The Journal of Chemical Physics 20(4) (1952) 614-628.
[28] A. Turnbull, 4 - Hydrogen diffusion and trapping in metals, in: R.P. Gangloff, B.P. Somerday (Eds.), Gaseous Hydrogen Embrittlement of Materials in Energy Technologies, Woodhead Publishing2012, pp. 89-128.
[29] K. Farrell, M.B. Lewis, The hydrogen content of austenite after cathodic charging, Scr. Metall. Mater. 15(6) (1981) 661-664.
[30] G. Gottstein, Physical foundations of materials science, Springer Science & Business Media2013.
[31] M. Koyama, M. Rohwerder, C.C. Tasan, A. Bashir, E. Akiyama, K. Takai, D. Raabe, K. Tsuzaki, Recent progress in microstructural hydrogen mapping in steels: quantification, kinetic analysis, and multi-scale characterisation, Mater. Sci. Technol. 33(13) (2017) 1481-1496.
[32] E. Van den Eeckhout, T. Depover, K. Verbeken, The Effect of Microstructural Characteristics on the Hydrogen Permeation Transient in Quenched and Tempered Martensitic Alloys, Metals-Basel 8(10) (2018).
[33] A. Oudriss, J. Creus, J. Bouhattate, C. Savall, B. Peraudeau, X. Feaugas, The diffusion and trapping of hydrogen along the grain boundaries in polycrystalline nickel, Scr. Mater. 66(1) (2012) 37-40.
[34] D.P. Escobar, K. Verbeken, L. Duprez, M. Verhaege, Evaluation of hydrogen trapping in high strength steels by thermal desorption spectroscopy, Mater. Sci. Eng. A 551 (2012) 50-58.
[35] D. Guedes, L. Cupertino Malheiros, A. Oudriss, S. Cohendoz, J. Bouhattate, J. Creus, F. Thébault, M. Piette, X. Feaugas, The role of plasticity and hydrogen flux in the fracture of a tempered martensitic steel: A new design of mechanical test until fracture to separate the influence of mobile from deeply trapped hydrogen, Acta Mater. 186 (2020) 133-148.
[36] J. Li, A. Oudriss, A. Metsue, J. Bouhattate, X. Feaugas, Anisotropy of hydrogen diffusion in nickel single crystals: the effects of self-stress and hydrogen concentration on diffusion, Sci. Rep. 7(1) (2017) 45041.
[37] V. Olden, C. Thaulow, R. Johnsen, Modelling of hydrogen diffusion and hydrogen induced cracking in supermartensitic and duplex stainless steels, Mater. Des. 29(10) (2008) 1934-1948.

[38] X. Lu, D. Wang, D. Wan, Z.B. Zhang, N. Kheradmand, A. Barnoush, Effect of electrochemical charging on the hydrogen embrittlement susceptibility of Alloy 718, Acta Mater. 179 (2019) 36-48.
[39] D. Wang, X. Lu, Y. Deng, D. Wan, Z. Li, A. Barnoush, Effect of hydrogen-induced surface steps on the nanomechanical behavior of a CoCrFeMnNi high-entropy alloy revealed by in-situ electrochemical nanoindentation, Intermetallics 114 (2019) 106605.
[40] D.G. Ulmer, C.J. Altstetter, Phase-Relations in the Hydrogen Austenite System, Acta Metall. Mater. 41(7) (1993) 2235-2241.
[41] Q. Yang, L.J. Qiao, S. Chiovelli, J.L. Luo, Critical hydrogen charging conditions for martensite transformation and surface cracking in type 304 stainless steel, Scr. Mater. 40(11) (1999) 1209-1214.
[42] A. Oudriss, S. Le Guernic, Z. Wang, B. Osman Hoch, J. Bouhattate, E. Conforto, Z. Zhu, D.S. Li, X. Feaugas, Meso-scale anisotropic hydrogen segregation near grain-boundaries in polycrystalline nickel characterized by EBSD/SIMS, Mater. Lett. 165 (2016) 217-222.
[43] B. Ladna, H.K. Birnbaum, SIMS study of hydrogen at the surface and grain boundaries of nickel bicrystals, Acta Metall. 35(10) (1987) 2537-2542.
[44] T. Tsuru, R.M. Latanision, Grain boundary transport of hydrogen in nickel, Scr. Metall. Mater. 16(5) (1982) 575-578.
[45] C. Beachem, A new model for hydrogen-assisted cracking (hydrogen "embrittlement"), Metallurgical and Materials Transactions B 3(2) (1972) 441-455.
[46] H.K. Birnbaum, P. Sofronis, Hydrogen-enhanced localized plasticity—a mechanism for hydrogen-related fracture, Mater. Sci. Eng. A 176(1) (1994) 191-202.
[47] I.M. Robertson, The effect of hydrogen on dislocation dynamics, Eng. Fract. Mech. 68(6) (2001) 671-692.
[48] P. Sofronis, I. Robertson, Transmission electron microscopy observations and micromechanical/continuum models for the effect of hydrogen on the mechanical behaviour of metals, Philosophical Magazine A 82(17-18) (2002) 3405-3413.
[49] S. Lynch, Progress towards understanding mechanisms of hydrogen embrittlement and stress corrosion cracking, CORROSION 2007, NACE International, 2007.
[50] M.L. Martin, J.A. Fenske, G.S. Liu, P. Sofronis, I.M. Robertson, On the formation and nature of quasi-cleavage fracture surfaces in hydrogen embrittled steels, Acta Mater. 59(4) (2011) 1601-1606.
[51] T. Neeraj, R. Srinivasan, J. Li, Hydrogen embrittlement of ferritic steels: Observations on deformation microstructure, nanoscale dimples and failure by nanovoiding, Acta Mater. 60(13-14) (2012) 5160-5171.
[52] W.A. Mcinteer, A.W. Thompson, I.M. Bernstein, The Effect of Hydrogen on the Slip Character of Nickel, Acta Metall. 28(7) (1980) 887-894.
[53] E. Lunarska, V. Novak, N. Zarubova, S. Kadeckova, Effect of Electrolytic Hydrogen Charging on Flow-Stress and Slip Line Pattern in Iron Single-Crystals, Scr. Metall. Mater. 17(6) (1983) 705-710.
[54] G. Lu, Q. Zhang, N. Kioussis, E. Kaxiras, Hydrogen-enhanced local plasticity in aluminum: An ab initio study, Phys. Rev. Lett. 87(9) (2001) art. no.-095501.
[55] J. Song, W.A. Curtin, A nanoscale mechanism of hydrogen embrittlement in metals, Acta Mater. 59(4) (2011) 1557-1569.
[56] J. Song, W.A. Curtin, Mechanisms of hydrogen-enhanced localized plasticity: An atomistic study using alpha-Fe as a model system, Acta Mater. 68 (2014) 61-69.

[57] A. Barnoush, M. Asgari, R. Johnsen, Resolving the hydrogen effect on dislocation nucleation and mobility by electrochemical nanoindentation, Scr. Mater. 66(6) (2012) 414-417.
[58] A.R. Troiano, The role of hydrogen and other interstitials in the mechanical behavior of metals, trans. ASM 52 (1960) 54-80.
[59] R.A. Oriani, P.H. Josephic, Equilibrium Aspects of Hydrogen-Induced Cracking of Steels, Acta Metall. 22(9) (1974) 1065-1074.
[60] C.J. McMahon, Hydrogen-induced intergranular fracture of steels, Eng. Fract. Mech. 68(6) (2001) 773-788.
[61] L.B. Pfeil, The effect of occluded hydrogen on the tensile strength of iron, Proceedings of the Royal Society of London. Series A, Containing Papers of a Mathematical and Physical Character 112(760) (1926) 182-195.
[62] J.F. Knott, Fracture Toughness and Hydrogen-Assisted Crack Growth in Engineering Alloys, Hydrogen Effects in Materials, pp. 385-408.
[63] J. Yao, S.A. Meguid, Hydrogen diffusion and intergranular cracking in nickel, Int. J. Hydrog. Energy 22(10) (1997) 1021-1026.
[64] S. Lynch, Some fractographic contributions to understanding fatigue crack growth, Int. J. Fatigue 104 (2017) 12-26.
[65] S.P. Lynch, 2 - Hydrogen embrittlement (HE) phenomena and mechanisms, in: V.S. Raja, T. Shoji (Eds.), Stress Corrosion Cracking, Woodhead Publishing2011, pp. 90-130.
[66] M. Nagumo, Hydrogen related failure of steels - a new aspect, Mater. Sci. Technol. 20(8) (2004) 940-950.
[67] M. Hatano, M. Fujinami, K. Arai, H. Fujii, M. Nagumo, Hydrogen embrittlement of austenitic stainless steels revealed by deformation microstructures and strain-induced creation of vacancies, Acta Mater. 67 (2014) 342-353.
[68] R.B. McLellan, Z.R. Xu, Hydrogen-induced vacancies in the iron lattice, Scr. Mater. 36(10) (1997) 1201-1205.
[69] A. Metsue, A. Oudriss, X. Feaugas, Hydrogen solubility and vacancy concentration in nickel single crystals at thermal equilibrium: New insights from statistical mechanics and ab initio calculations, J. Alloys Compd. 656 (2016) 555-567.
[70] A. Metsue, A. Oudriss, X. Feaugas, Trapping/detrapping kinetic rates of hydrogen around a vacancy in nickel and some consequences on the hydrogen-vacancy clusters thermodynamic equilibrium, Comp. Mater. Sci. 151 (2018) 144-152.
[71] G. Hachet, J. Li, A.M. Hallil, A. Metsue, A. Oudriss, J. Bouhattate, X. Feaugas, A multi-scale analysis of the different interactions between defects and hydrogen: A review on the contribution of the elastic fields, Eng. Fract. Mech. 218 (2019) 106621.
[72] R. Kirchheim, Revisiting hydrogen embrittlement models and hydrogen-induced homogeneous nucleation of dislocations, Scr. Mater. 62(2) (2010) 67-70.
[73] M. Zamanzade, H. Vehoff, A. Barnoush, Cr effect on hydrogen embrittlement of Fe3Al-based iron aluminide intermetallics: Surface or bulk effect, Acta Mater. 69 (2014) 210-223.
[74] O. Grassel, L. Kruger, G. Frommeyer, L.W. Meyer, High strength Fe-Mn-(Al, Si) TRIP/TWIP steels development-properties-application, Int. J. Plast. 16(10-11) (2000) 1391-1409.
[75] R.A. Hadfield, Manganese-steel: I. Manganese in its application to metallurgy: II. Some newly-discovered properties of iron and manganese, Institution1888.
[76] O. Bouaziz, S. Allain, C.P. Scott, P. Cugy, D. Barbier, High manganese austenitic twinning induced plasticity steels: A review of the microstructure properties relationships, Curr. Opin. Solid State Mater. Sci. 15(4) (2011) 141-168.

[77] S. Allain, J.P. Chateau, O. Bouaziz, A physical model of the twinning-induced plasticity effect in a high manganese austenitic steel, Mater. Sci. Eng. A 387 (2004) 143-147.
[78] S. Curtze, V.T. Kuokkala, Dependence of tensile deformation behavior of TWIP steels on stacking fault energy, temperature and strain rate, Acta Mater. 58(15) (2010) 5129-5141.
[79] D.T. Pierce, J.A. Jiménez, J. Bentley, D. Raabe, J.E. Wittig, The influence of stacking fault energy on the microstructural and strain-hardening evolution of Fe–Mn–Al–Si steels during tensile deformation, Acta Mater. 100 (2015) 178-190.
[80] B.C. De Cooman, Y. Estrin, S.K. Kim, Twinning-induced plasticity (TWIP) steels, Acta Mater. 142 (2018) 283-362.
[81] A.S. Hamada, L.P. Karjalainen, M.C. Somani, The influence of aluminum on hot deformation behavior and tensile properties of high-Mn TWIP steels, Mater. Sci. Eng. A 467(1) (2007) 114-124.
[82] I. Gutierrez-Urrutia, S. Zaefferer, D. Raabe, Electron channeling contrast imaging of twins and dislocations in twinning-induced plasticity steels under controlled diffraction conditions in a scanning electron microscope, Scr. Mater. 61(7) (2009) 737-740.
[83] J.L. Zhang, S. Zaefferer, D. Raabe, A study on the geometry of dislocation patterns in the surrounding of nanoindents in a TWIP steel using electron channeling contrast imaging and discrete dislocation dynamics simulations, Mater. Sci. Eng. A 636 (2015) 231-242.
[84] D.W. Suh, Critical Assessment 2: Hydrogen induced fracture in austenitic, high-manganese TWIP steel, Mater. Sci. Technol. 30(10) (2014) 1131-1134.
[85] J.A. Ronevich, S.K. Kim, J.G. Speer, D.K. Matlock, Hydrogen effects on cathodically charged twinning-induced plasticity steel, Scr. Mater. 66(12) (2012) 956-959.
[86] M. Koyama, E. Akiyama, Y.K. Lee, D. Raabe, K. Tsuzaki, Overview of hydrogen embrittlement in high-Mn steels, Int. J. Hydrog. Energy 42(17) (2017) 12706-12723.
[87] M. Koyama, E. Akiyama, K. Tsuzaki, D. Raabe, Hydrogen-assisted failure in a twinning-induced plasticity steel studied under in situ hydrogen charging by electron channeling contrast imaging, Acta Mater. 61(12) (2013) 4607-4618.
[88] S.M. Lee, I.J. Park, J.G. Jung, Y.K. Lee, The effect of Si on hydrogen embrittlement of Fe-18Mn-0.6C-xSi twinning-induced plasticity steels, Acta Mater. 103 (2016) 264-272.
[89] K.G. Chin, C.Y. Kang, S.Y. Shin, S. Hong, S. Lee, H.S. Kim, K.H. Kim, N.J. Kim, Effects of Al addition on deformation and fracture mechanisms in two high manganese TWIP steels, Mater. Sci. Eng. A 528(6) (2011) 2922-2928.
[90] M. Koyama, E. Akiyama, K. Tsuzaki, Hydrogen Embrittlement in Al-added Twinning-induced Plasticity Steels Evaluated by Tensile Tests during Hydrogen Charging, ISIJ Int. 52(12) (2012) 2283-2287.
[91] T. Dieudonne, L. Marchetti, M. Wery, J. Chene, C. Allely, P. Cugy, C.P. Scott, Role of copper and aluminum additions on the hydrogen embrittlement susceptibility of austenitic Fe-Mn-C TWIP steels, Corros. Sci. 82 (2014) 218-226.
[92] Y.J. Kwon, T. Lee, J. Lee, Y.S. Chun, C.S. Lee, Role of Cu on hydrogen embrittlement behavior in Fe-Mn-C-Cu TWIP steel, Int. J. Hydrog. Energy 40(23) (2015) 7409-7419.
[93] O. Bouaziz, S. Allain, C. Scott, Effect of grain and twin boundaries on the hardening mechanisms of twinning-induced plasticity steels, Scr. Mater. 58(6) (2008) 484-487.
[94] M. Koyama, E. Akiyama, K. Tsuzaki, Effect of hydrogen content on the embrittlement in a Fe-Mn-C twinning-induced plasticity steel, Corros. Sci. 59 (2012) 277-281.

[95] J.W. Yeh, S.K. Chen, S.J. Lin, J.Y. Gan, T.S. Chin, T.T. Shun, C.H. Tsau, S.Y. Chang, Nanostructured high-entropy alloys with multiple principal elements: Novel alloy design concepts and outcomes, Adv. Eng. Mater. 6(5) (2004) 299-303.
[96] Y. Zhang, T.T. Zuo, Z. Tang, M.C. Gao, K.A. Dahmen, P.K. Liaw, Z.P. Lu, Microstructures and properties of high-entropy alloys, Prog. Mater. Sci. 61 (2014) 1-93.
[97] A.J. Zaddach, R.O. Scattergood, C.C. Koch, Tensile properties of low-stacking fault energy high-entropy alloys, Mater. Sci. Eng. A 636 (2015) 373-378.
[98] A.J. Zaddach, C. Niu, C.C. Koch, D.L. Irving, Mechanical Properties and Stacking Fault Energies of NiFeCrCoMn High-Entropy Alloy, Jom 65(12) (2013) 1780-1789.
[99] D.B. Miracle, O.N. Senkov, A critical review of high entropy alloys and related concepts, Acta Mater. 122 (2017) 448-511.
[100] O. Senkov, J. Scott, S. Senkova, D. Miracle, C. Woodward, Microstructure and room temperature properties of a high-entropy TaNbHfZrTi alloy, J. Alloys Compd. 509(20) (2011) 6043-6048.
[101] M.C. Gao, B. Zhang, S.M. Guo, J.W. Qiao, J.A. Hawk, High-Entropy Alloys in Hexagonal Close-Packed Structure, Metall. Mater. Trans. A 47a(7) (2016) 3322-3332.
[102] B. Cantor, I.T.H. Chang, P. Knight, A.J.B. Vincent, Microstructural development in equiatomic multicomponent alloys, Mater. Sci. Eng. A 375-377 (2004) 213-218.
[103] T. Teramoto, K. Yamada, R. Ito, K. Tanaka, Monocrystalline elastic constants and their temperature dependences for equi-atomic Cr-Mn-Fe-Co-Ni high-entropy alloy with the face-centered cubic structure, J. Alloys Compd. 777 (2019) 1313-1318.
[104] F. Otto, N.L. Hanold, E.P. George, Microstructural evolution after thermomechanical processing in an equiatomic, single-phase CoCrFeMnNi high-entropy alloy with special focus on twin boundaries, Intermetallics 54 (2014) 39-48.
[105] G. Laplanche, P. Gadaud, O. Horst, F. Otto, G. Eggeler, E.P. George, Temperature dependencies of the elastic moduli and thermal expansion coefficient of an equiatomic, single-phase CoCrFeMnNi high-entropy alloy, J. Alloys Compd. 623 (2015) 348-353.
[106] S. Huang, W. Li, S. Lu, F.Y. Tian, J. Shen, E. Holmstrom, L. Vitos, Temperature dependent stacking fault energy of FeCrCoNiMn high entropy alloy, Scr. Mater. 108 (2015) 44-47.
[107] S.F. Liu, Y. Wu, H.T. Wang, J.Y. He, J.B. Liu, C.X. Chen, X.J. Liu, H. Wang, Z.P. Lu, Stacking fault energy of face-centered-cubic high entropy alloys, Intermetallics 93 (2018) 269-273.
[108] Z. Wu, C.M. Parish, H. Bei, Nano-twin mediated plasticity in carbon-containing FeNiCoCrMn high entropy alloys, J. Alloys Compd. 647 (2015) 815-822.
[109] Z.M. Li, C.C. Tasan, H. Springer, B. Gault, D. Raabe, Interstitial atoms enable joint twinning and transformation induced plasticity in strong and ductile high-entropy alloys, Sci. Rep. 7 (2017) 40704.
[110] Z. Li, Interstitial equiatomic CoCrFeMnNi high-entropy alloys: carbon content, microstructure, and compositional homogeneity effects on deformation behavior, Acta Mater. 164 (2019) 400-412.
[111] Z. Li, K.G. Pradeep, Y. Deng, D. Raabe, C.C. Tasan, Metastable high-entropy dual-phase alloys overcome the strength-ductility trade-off, Nature 534(7606) (2016) 227-30.
[112] Z.M. Li, D. Raabe, Strong and Ductile Non-equiatomic High-Entropy Alloys: Design, Processing, Microstructure, and Mechanical Properties, Jom 69(11) (2017) 2099-2106.
[113] H. Luo, Z. Li, D. Raabe, Hydrogen enhances strength and ductility of an equiatomic high-entropy alloy, Sci. Rep. 7(1) (2017) 9892.

[114] Y. Zhao, D.-H. Lee, M.-Y. Seok, J.-A. Lee, M.P. Phaniraj, J.-Y. Suh, H.-Y. Ha, J.-Y. Kim, U. Ramamurty, J.-i. Jang, Resistance of CoCrFeMnNi high-entropy alloy to gaseous hydrogen embrittlement, Scr. Mater. 135 (2017) 54-58.
[115] Y.J. Kwon, J.W. Won, S.H. Park, J.H. Lee, K.R. Lim, Y.S. Na, C.S. Lee, Ultrahigh-strength CoCrFeMnNi high-entropy alloy wire rod with excellent resistance to hydrogen embrittlement, Mater. Sci. Eng. A 732 (2018) 105-111.
[116] M. Koyama, K. Ichii, K. Tsuzaki, Grain refinement effect on hydrogen embrittlement resistance of an equiatomic CoCrFeMnNi high-entropy alloy, Int. J. Hydrog. Energy (2019).
[117] K.E. Nygren, K.M. Bertsch, S. Wang, H. Bei, A. Nagao, I.M. Robertson, Hydrogen embrittlement in compositionally complex FeNiCoCrMn FCC solid solution alloy, Curr. Opin. Solid State Mater. Sci. 22(1) (2018) 1-7.
[118] K.E. Nygren, S. Wang, K.M. Bertsch, H.B. Bei, A. Nagao, I.M. Robertson, Hydrogen embrittlement of the equi-molar FeNiCoCr alloy, Acta Mater. 157 (2018) 218-227.
[119] W.C. Oliver, G.M. Pharr, Measurement of hardness and elastic modulus by instrumented indentation: Advances in understanding and refinements to methodology, J. Mater. Res. 19(1) (2004) 3-20.
[120] ISO14577-4, Metallic materials—Instrumented indentation test for hardness and materials parameters—Part 4: Test method for metallic and non-metallic coatings, International Organization for Standardization, Geneva, 2016.
[121] K.L. Johnson, Contact Mechanics, Cambridge University Press, Cambridge, 1987.
[122] H.R. Hertz, Ueber die Berührung fester elastischer Körper, Journal für die reine und angewandte Mathematik (Crelles Journal), 1882, pp. 157-171.
[123] J. Boussinesq, Théorie des ondes et des remous qui se propagent le long d'un canal rectangulaire horizontal, en communiquant au liquide contenu dans ce canal des vitesses sensiblement pareilles de la surface au fond, Journal de mathématiques pures et appliquées (1872) 55-108.
[124] I.N. Sneddon, The relation between load and penetration in the axisymmetric boussinesq problem for a punch of arbitrary profile, International Journal of Engineering Science 3(1) (1965) 47-57.
[125] K. Durst, B. Backes, M. Goken, Indentation size effect in metallic materials: Correcting for the size of the plastic zone, Scr. Mater. 52(11) (2005) 1093-1097.
[126] W.D. Nix, H.J. Gao, Indentation size effects in crystalline materials: A law for strain gradient plasticity, J. Mech. Phys. Solids 46(3) (1998) 411-425.
[127] J. Chen, S.J. Bull, On the relationship between plastic zone radius and maximum depth during nanoindentation, Surf. Coat. Technol. 201(7) (2006) 4289-4293.
[128] S. Shim, H. Bei, E.P. George, G.M. Pharr, A different type of indentation size effect, Scr. Mater. 59(10) (2008) 1095-1098.
[129] Y. Gao, C.J. Ruestes, D.R. Tramontina, H.M. Urbassek, Comparative simulation study of the structure of the plastic zone produced by nanoindentation, J. Mech. Phys. Solids 75 (2015) 58-75.
[130] Y. Liu, A.H.W. Ngan, Depth dependence of hardness in copper single crystals measured by nanoindentation, Scr. Mater. 44(2) (2001) 237-241.
[131] B.B. He, M.X. Huang, Z.Y. Liang, A.H.W. Ngan, H.W. Luo, J. Shi, W.Q. Cao, H. Dong, Nanoindentation investigation on the mechanical stability of individual austenite grains in a medium-Mn transformation-induced plasticity steel, Scr. Mater. 69(3) (2013) 215-218.

[132] T.L. Li, Y.F. Gao, H. Bei, E.P. George, Indentation Schmid factor and orientation dependence of nanoindentation pop-in behavior of NiAl single crystals, J. Mech. Phys. Solids 59(6) (2011) 1147-1162.
[133] A. Barnoush, Correlation between dislocation density and nanomechanical response during nanoindentation, Acta Mater. 60(3) (2012) 1268-1277.
[134] A. Barnoush, M.T. Welsch, H. Vehoff, Correlation between dislocation density and pop-in phenomena in aluminum studied by nanoindentation and electron channeling contrast imaging, Scr. Mater. 63(5) (2010) 465-468.
[135] D.F. Bahr, D.E. Kramer, W.W. Gerberich, Non-linear deformation mechanisms during nanoindentation, Acta Mater. 46(10) (1998) 3605-3617.
[136] M. Zamanzade, H. Vehoff, A. Barnoush, Effect of chromium on elastic and plastic deformation of Fe3Al intermetallics, Intermetallics 41 (2013) 28-34.
[137] T.B. Britton, D. Randman, A.J. Wilkinson, Nanoindentation study of slip transfer phenomenon at grain boundaries, J. Mater. Res. 24(3) (2009) 607-615.
[138] N.G. Chechenin, J. Bøttiger, J.P. Krog, Nanoindentation of amorphous aluminum oxide films II. Critical parameters for the breakthrough and a membrane effect in thin hard films on soft substrates, Thin Solid Films 261(1) (1995) 228-235.
[139] J.R. Morris, H. Bei, G.M. Pharr, E.P. George, Size Effects and Stochastic Behavior of Nanoindentation Pop In, Phys. Rev. Lett. 106(16) (2011) 165502.
[140] J. Frenkel, Zur Theorie der Elastizitätsgrenze und der Festigkeit kristallinischer Körper, 37(7) (1926) 572-609.
[141] M. Kappes, G.S. Frankel, R. Thodla, M. Mueller, N. Sridhar, R.M. Carranza, Hydrogen Permeation and Corrosion Fatigue Crack Growth Rates of X65 Pipeline Steel Exposed to Acid Brines Containing Thiosulfate or Hydrogen Sulfide, Corrosion 68(11) (2012).
[142] M. Deutges, I. Knorr, C. Borchers, C.A. Volkert, R. Kirchheim, Influence of hydrogen on the deformation morphology of vanadium (100) micropillars in the α-phase of the vanadium–hydrogen system, Scr. Mater. 68(1) (2013) 71-74.
[143] S. Zaefferer, N.N. Elhami, Theory and application of electron channelling contrast imaging under controlled diffraction conditions, Acta Mater. 75 (2014) 20-50.
[144] D. Wan, Hydrogen-Assisted Fatigue Crack Growth in Ferritic Steels, NTNU, 2019.
[145] R.R. KELLER, R.H. GEISS, Transmission EBSD from 10 nm domains in a scanning electron microscope, J. Microsc. 245(3) (2012) 245-251.
[146] G.C. Sneddon, P.W. Trimby, J.M. Cairney, Transmission Kikuchi diffraction in a scanning electron microscope: A review, Materials Science and Engineering: R: Reports 110 (2016) 1-12.

Part II

Paper I

Effect of hydrogen on the embrittlement susceptibility of Fe-22Mn-0.6C TWIP steel revealed by in-situ tensile tests

Submitted

Effect of hydrogen on the embrittlement susceptibility of Fe-22Mn-0.6C TWIP steel revealed by in-situ tensile tests

Abstract: We investigated the hydrogen embrittlement on a Fe-22Mn-0.6C twinning-induced plasticity steel by tensile tests with in-situ scanning electron microscope observation, plus electron backscatter diffraction and electron channeling contrast imaging techniques. The tensile tests were performed on specimens with 0, 50, 150, and 300 hours pre-charged hydrogen, which accumulatively reduced the mechanical properties and induced a ductile-to-brittle fracture transition. The threshold of hydrogen content to trigger this ductile-to-brittle transition was further determined. During the tensile tests, intergranular secondary cracks were observed on gauge surface of specimens with pre-charged hydrogen. The low angle grain boundaries exhibited better resistance to both crack initiation and propagation compared with high angle grain boundaries. In addition, the stress concentration together with the hydrogen effect on grain boundaries intersecting with deformation twins are proposed as the reasons for the crack initiation and propagation.

Keywords: Twinning-induced plasticity (TWIP) steel; Hydrogen embrittlement; Deformation twinning; Secondary cracks; Electron channeling contrast imaging (ECCI)

1. Introduction

High manganese twinning induced plasticity (TWIP) steels are drawing increasing attention in automobile and construction industries due to their excellent combination of high strength and good ductility [1-3]. The outstanding mechanical properties of TWIP steels have been revealed as a result of mechanical twin formation and dynamic strain aging effect during plastic deformation due to its relatively low stacking fault energy (SFE, between 20 and 40 mJ/m^2 at room temperature) [4]. With this low SFE, the mobility of dislocations is reduced and the work hardening capacity is enhanced. However, the catastrophic degradation of mechanical properties has been reported on TWIP steels at hydrogen-containing environment known as hydrogen embrittlement phenomenon [5-7]. The hydrogen embrittlement is a crucial problem that needs to be urgently solved on TWIP steels before further practical using.

Up to now, the hydrogen embrittlement on different types of high-Mn steels has been studied by a large variety of experiment methods such as tensile test [8, 9], deep drawing cup test [10], nanoindentation test [11] and microcantilever bending test [12]. These tests were performed at different scales focusing on the effect of grain size, alloying elements, dissolved hydrogen concentration, and strain rate on the hydrogen embrittlement behaviors. Specifically, the hydrogen embrittlement resistance decreases with grain refinement [8, 13], addition of Al and Cu [10, 14], decreasing diffusible hydrogen content [12], and increasing strain rate [15, 16]. With further fractographic analysis, critical in-situ observations, and computational simulations, several mechanisms have been proposed, among which the hydrogen-enhanced localized plasticity (HELP) [17, 18], hydrogen-enhanced decohesion (HEDE) [19, 20], adsorption-induced dislocation emission (AIDE) [21, 22], and hydrogen-enhanced strain-induced vacancy formation (HESIV) [23, 24] are the most popular ones.

The HELP mechanism was firstly introduced by Beachem [17, 25], who analyzed the interaction between hydrogen and dislocations through in-situ transmission electron microscopy (TEM) observations. The main idea is that hydrogen atoms surrounding the dislocations can effectively shield the stress field of dislocations in certain directions and lead to slip planarity in those soft directions. Moreover, hydrogen atoms accumulated around the crack tips facilitate dislocation activities and lead to the formation of localized plastic zones, enhancing the crack propagation. The HEDE mechanism proposes that the cohesive energy decreases when hydrogen is trapped at the grain boundaries, second phase interfaces, and cleavage planes [26]. Consequently, these areas become the most vulnerable sites that undergo cracking under stress. The AIDE mechanism states that the hydrogen adsorbed at the crack tips weakens interatomic bonds and thereby facilitates dislocation nucleation and microvoid formation ahead of the crack tips and further contributes to crack growth [21]. The HESIV model proposed by Nagumo [24] shifted the viewpoint of the research community from hydrogen to hydrogen-enhanced strain-induced formation of vacancies. This mechanism has been proven in many cases of face-centered cubic (FCC) austenitic steels [27, 28]. Specifically, it suggests that hydrogen enhances the density and clustering of vacancies, which coalesce to microvoids and further combine as larger voids, thereby decreasing the ductile crack growth resistance. In spite of extensive studies and debates, consensus could not be reached on the hydrogen embrittlement behavior, since it is a complex process depending heavily on the applied

environment and material structure. Moreover, the aforementioned mechanisms are not completely distinct but share overlaps with each other [22].

In this study, the effect of hydrogen on a Fe-22Mn-0.6C TWIP steel was evaluated by tensile test with different amount of pre-charged hydrogen under in-situ scanning electron microscope (SEM) observation, plus further post-mortem characterizations at the microstructure level. The objective of this paper is to reveal a quantitative relationship between the fracture mode transition and the dissolved hydrogen content, to analyze the vulnerability of different types of grain boundaries to hydrogen-assisted cracking, and also to determine the mechanism of secondary cracks initiation and propagation.

2. Experimental

The studied material is a Fe-22Mn-0.6C (wt. %) TWIP steel and its chemical composition is shown in Table 1. The material was prepared by ingot casting, followed by hot rolling and cold rolling to a thickness of 1.5 mm. It was then solution treated at 1150 °C for 5 h in an argon atmosphere. The specimens used for slow strain rate tensile test (SSRT) were cut by electrical discharge machining into a two-step dog-bone shape with gauge geometry of 5 mm × 2 mm × 1 mm as shown in Fig. 1. Prior to the hydrogen charging, the sample surface was ground sequentially from 120 to 4000 grit SiC papers and then polished with 3 μm and 1 μm diamond pastes. The surface preparation was finalized by additional polishing with colloidal silica suspension for 20 min to remove the deformation layer from the previous mechanical polishing.

The hydrogen pre-charging process was performed by using a standard electrochemical cell, which consists of a Pt net as counter electrode and an Ag/AgCl reference electrode. Hereafter, all the reported potentials in this study are versus Ag/AgCl reference electrode. The hydrogen charging was performed at 80 °C with a constant cathodic potential of -1400 mV (~10 mA/cm^2) in a glycerol-based electrolyte, which consists of 600 g borax (sodium tetraborate decahydrate) dissolved into 1 L glycerol. In addition, 20 vol% distilled water with 0.002 M $Na_2S_2O_3$ were added to enhance the conductivity and promote the hydrogen absorption [12]. This electrolyte has been proven to be able to preserve the sample surface from corrosion after long-time electrochemical charging [11], easing the in-situ observation during tensile tests without additional surface

preparation. In the current study, three different charging times of 50, 150, 300 h were applied to study the effect of different hydrogen content on the mechanical properties.

The hydrogen content after different charging time was measured by thermal desorption spectroscopy (TDS). The TDS tests were performed using a Bruker G4 PHOENIX DH hydrogen analyzer together with a mass spectrometry detector set up (ESD 100, InProcess Instruments, Germany) at a corresponding heating rate of 25 °C/min from 25 °C to 750 °C. In order to eliminate the outgassing of hydrogen, the TDS tests were started immediately after each hydrogen charging process with a dwell time of less than 5 min.

The SSRT tests were carried out by a Kammrath & Weiss tensile/compression module, which was installed into the chamber of a high-resolution scanning electron microscope (Quanta 650, Thermo Fisher Scientific Inc., US) for the sake of in-situ observation. The engineering strain rate was chosen as 4×10^{-5} s^{-1}. In the current study, the proposed strain value was calculated by dividing the elongation by the initial gauge length. The dwell time between the finish of hydrogen charging and the start of tensile test was controlled to less than 5 min to minimize the hydrogen loss during this period. The SSRT tests were performed on two groups of charged samples: one group was loaded till fracture to study the hydrogen effect on mechanical properties and fracture mode, the other group was loaded till 10% elongation to analyze the initiation of secondary cracks on the gauge surface. The details of the testing conditions in the current study are summarized in Table 2.

Prior to the tensile tests, the microstructure of the studied material was characterized by SEM with a backscatter electron (BSE) detector as well as the electron backscatter diffraction (EBSD) technique. After the tensile tests, the same microstructural characterization process was also conducted to observe the fracture surface and gauge surface. Specifically, the fracture mode transition was determined by a detailed fractographic analysis. The EBSD was conducted on the re-polished gauge surface to analyze the crystallographic information. In addition, the secondary cracks on the gauge surface in association with deformation twins were observed by the electron channeling contrast imaging (ECCI) technique, which has been proven as an excellent tool for identifying twins, stacking faults, and dislocations based on the controlled diffraction condition with optimum contrast [6, 29]. In the current study, the ECCI was performed in the same SEM equipped with a solid-state four-quadrant BSE detector at an acceleration voltage of 30 kV with a

working distance of ~6 mm. The ideal channeling contrast was obtained by tilting the specimen to an angle when the grain matrix is exactly in the Bragg condition, thus enabling the diffraction vector in a two-beam condition.

Table 1

Chemical composition of the studied Fe-22Mn-0.6C TWIP steel.

Element	Mn	C	Nb	Ti	V	N	Al	Fe
wt. %	22.60	0.63	0.03	0.03	0.108	0.016	0.008	Bal.

Table 2

Testing conditions in the current study.

testing group	charging time/ h	testing	aim
1	0, 50, 150, 300	tensile test till fracture	mechanical properties and fractography
2	0, 50, 150, 300	TDS	content of dissolved hydrogen
3	0, 300	Subsurface characterization	hydrogen charging induced subsurface crack
4	0, 50, 150, 300	tensile test till 10% elongation	secondary crack initiation

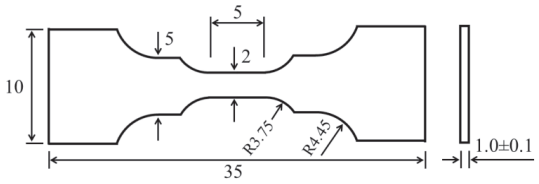

Fig. 1. Geometry of the tensile sample (in mm).

3. Results

3.1 Effect of electrochemical charging on surface and subsurface

The BSE image and the normal direction-inverse pole figure (ND-IPF) map of studied sample after surface preparation are presented in Fig. 2. It shows a smooth surface without any detectable scratches or cracks. The EBSD result shows a pure FCC phase with equiaxed grains containing annealing twins in the initial microstructure. The average grain size is 85 μm.

Lu et al. [30] studied the effect of electrochemical hydrogen charging on the sample surface of alloy 718. After long-time (60-80 h) charging with a similar charging condition as the current study, the slip lines and transgranular cracks were observed on the gauge surface of alloy 718. The cracks on subsurface were also detected through cross-section analysis. Moreover, the amount and size of cracks increased as a result of longer charging time. The morphology changes due to the electrochemical charging can be a strong influencing factor in the tensile performance of the charged material. Thus, a surface check after charging is needed to avoid such influence in this study. To detect the influence of electrochemical hydrogen charging process on the sample surface and subsurface, a maximum charging time of 300 h was performed followed by subsequent gauge surface and cross-section microstructure analysis. Fig. 3a and 3b show the SEM image and magnified BSE image of the gauge surface after 300 h hydrogen charging. In contrast to the aforementioned observations in alloy 718, neither slip lines nor surface cracks were detected on the gauge surface of the studied TWIP sample after long time hydrogen charging. The charged specimen was further electroplated with Ni and cut from the center to obtain the cross-section surface. The cross-sectional was carefully ground and polished with different removal thickness to guarantee the reproducibility of observation. The representative BSE images of cross-section on 300 h charged sample are shown in Fig. 3c and 3d, a defect-free subsurface without any observable cracks can be obtained. Therefore, the charging process in the current study using glycerol-based electrolyte can not only protect sample surface from corrosion, easing the following in-situ SEM observation, but also maintain the sample integrity during hydrogen charging without forming cracks on surface and subsurface.

It needs to mention here that the authors have also conducted the same electrochemical charging method on two types of high-entropy alloys with pure austenitic structure, in which slip lines were generated [31] or martensitic phase transformation was detected [32] during the charging process.

However, due to the different alloying systems and a relatively higher SFE (20-40 mJ/m^2), the currently studied TWIP steel did not show such behaviors during electrochemical charging, which can be confirmed from the SEM characterizations (Fig. 3). Therefore, the performance measured in the current study is the intrinsic hydrogen influenced property of the studied material and no external damage was contributing to the final performance.

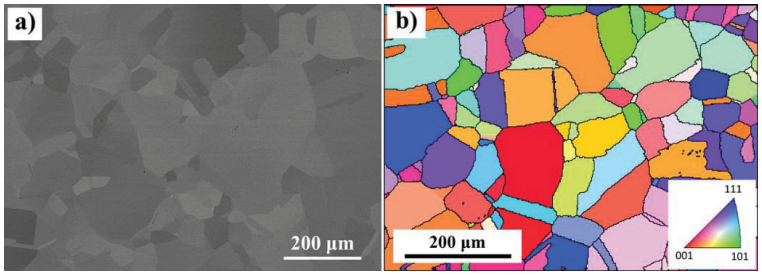

Fig. 2. (a) BSE image and (b) ND-IPF map showing the microstructure of the studied sample.

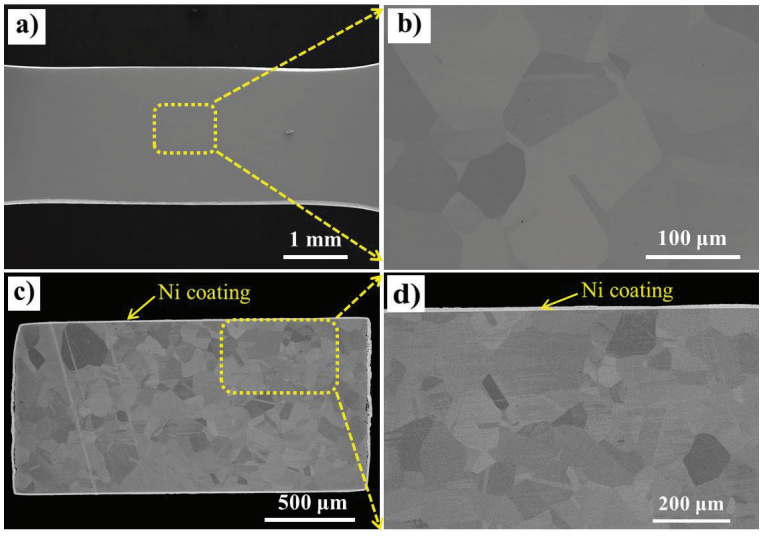

Fig. 3. (a) SE image of gauge surface after 300 h electrochemical hydrogen charging. (b) BSE image of magnified area of (a). (c) BSE image of cross-section after 300 h electrochemical hydrogen charging. (d) BSE image of magnified area of (c).

3.2 Tensile tests and associated hydrogen content measurement

The tensile tests were performed inside the SEM chamber with in-situ SEM observation for both hydrogen free and hydrogen pre-charged specimens. Four videos recording the testing process are presented in the supplementary document. For the hydrogen free specimen (as shown in Video1), a uniform elongation before the necking and fracture is presented. For the specimens charged with 50, 150, and 300 h hydrogen (as shown in Video 2, 3, and 4, respectively), secondary cracks can be clearly detected on the gauge surface after the yielding and the fracture elongations were also reduced with longer charging time. The engineering stress-strain curves of hydrogen uncharged and charged specimens are shown in Fig. 4. Clear serrations can be observed on the stress-strain curves due to the dynamic strain aging effect [33], which has been proposed as a common phenomenon in TWIP steels [1, 34]. The curves present an overlapped elastic region with a same yielding strength regardless of the charged hydrogen. However, both the tensile strength and the elongation to fracture reduced in the hydrogenated specimens, and the reduction was more significant with longer charging time. For the uncharged specimen, the fracture elongation was 77.2% and the ultimate tensile strength was 828.1 MPa. When charged with hydrogen by 50, 150, and 300 h, the fracture elongation was reduced to 62.8%, 49.1%, and 29.6%, and the ultimate tensile strength was reduced to 747.1, 622.7, and 477.4 MPa, respectively. In addition, the corresponding mechanical degradation due to dissolved hydrogen can be described by the embrittlement factor (EF) [35] as follows:

$$\mathrm{EF} = \left(1 - \frac{\varepsilon_H}{\varepsilon_{no\ H}}\right) \times 100\% \tag{1}$$

Where ε_H and $\varepsilon_{no\ H}$ indicate the engineering fracture strain of hydrogen pre-charged sample and uncharged sample, respectively. 0 is defined as the EF value at the uncharged condition and it continuously increased to 11.7%, 36.4%, and 61.7% after 50, 150, and 300 h hydrogen charging, respectively. A detailed summary of hydrogen induced mechanical property degradation is shown in Table 3.

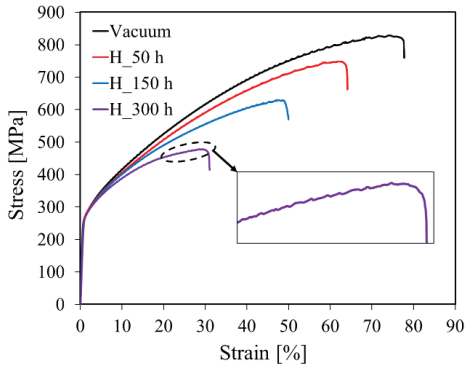

Fig. 4. Engineering stress-strain curves of specimens with different hydrogen pre-charging time.

Fig. 5 shows the curves of hydrogen desorption rate on the charged and uncharged samples obtained from the TDS measurement. The amount of hydrogen under the first peak at 300 °C stands for diffusible hydrogen, while that under the second peak at 550-600 °C corresponds to trapped hydrogen. The original hydrogen content of uncharged sample was 0.02 wppm and the dissolved hydrogen contents were 9.39, 16.57, and 22.31 wppm after 50, 150, and 300 h of electrochemical hydrogen charging, respectively. With increasing charging time, the hydrogen content increases significantly, which further degrades the mechanical properties to a higher level. It needs to mention here that the hydrogen contents shown above indicate the total amount of hydrogen, which includes the hydrogen dissolved in interstitial sites and trapped in both reversible and irreversible trapping sites.

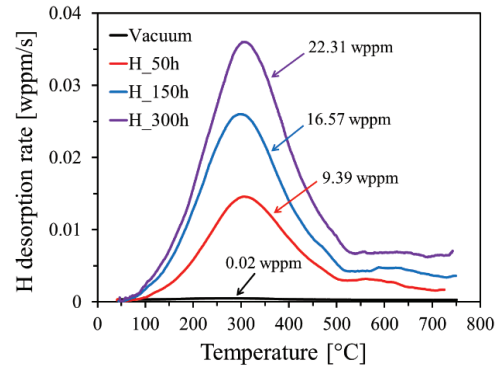

Fig. 5. Hydrogen desorption rate curves of hydrogen uncharged and charged samples.

Table 3

Properties of the studied materials under different hydrogen charging condition.

Charging time (h)	Fracture elongation (%)	Ultimate tensile strength (MPa)	EF (%)	Brittle depth (μm)	Hydrogen content (wppm)
0	77.2	828.1	0	0	0.02
50	62.8	747.1	11.7	57.6	9.39
150	49.1	622.7	36.4	102.2	16.57
300	29.6	477.4	61.7	148.5	22.31

3.3 Fracture surface and gauge surface characterization

The fracture surfaces after failure are summarized in Fig. 6. Fig. 6a1 shows the fracture surface of the uncharged specimen and Fig. 6a2 is the magnified image of the highlighted area in Fig. 6a1. A notable ductile fracture surface can be observed on the uncharged sample from gauge surface to the center region with fully covered dimple structure. The fracture surface after hydrogen charging of 50, 150, and 300 h are exhibited in Fig. 6b1, 6c1, and 6d1, as well as in the magnified images of Fig. 6b2, 6c2, and 6d2, respectively. In contrast, brittle intergranular fracture surfaces were observed at the areas near sample surface. Clearly, the ductile fracture mode was transformed to intergranular fracture mode after hydrogen charging with an observable transition boundary marked as blue dashed lines in Fig. 6b1, 6c1, and 6d1. In addition, the intergranular fracture was more pronounced with a longer charging time. The depths of the intergranular zone were measured as 57.6, 102.2, and 148.5 μm after 50, 150, and 300 h hydrogen charging, respectively.

As exhibited in the in-situ tensile test videos in the supplementary document, the fracture happened with a crack initiated from one side of specimen edge and propagated to the other side as the main or primary crack. The direction of the main crack propagation was nearly perpendicular to the tensile direction. In addition, a considerable number of secondary cracks were formed parallel to the main crack on the hydrogen charged samples (Fig. 7b) after the yielding point. Fig. 7a summarizes the area fraction of secondary cracks at different charging conditions throughout the whole tensile tests. In this method, all secondary cracks larger than 1 μm^2 were considered. For each step, three areas of 1.5×1.5 mm^2 were analyzed to minimize the statistical discrepancy. There

was no detectable secondary crack on the uncharged sample (Fig. 4a and 4c), while the area fraction of secondary cracks on the charged samples increased with larger strain. Moreover, the crack area on the sample with longer charging time was larger than that with shorter charging time, and this difference became more pronounced along the tensile elongation.

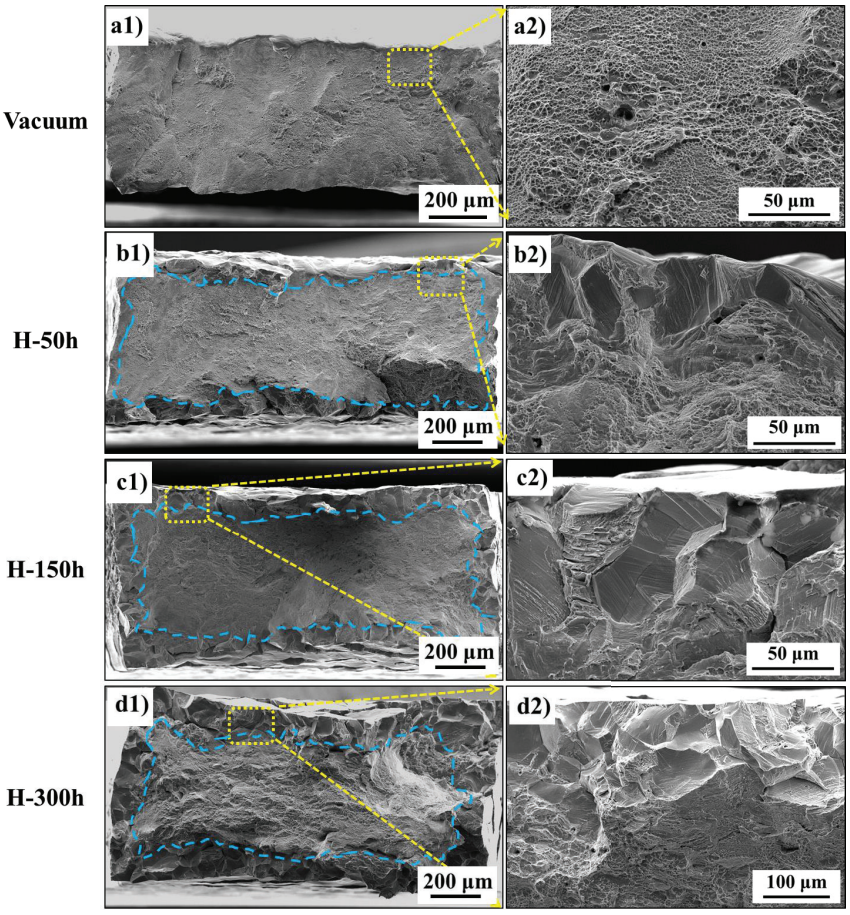

Fig. 6. Fracture surface of the tensile tested samples with and without hydrogen pre-charging. a) Fracture surface of reference sample without hydrogen charging. Fracture surface of samples after b) 50 h, c) 150 h, and d) 300 h hydrogen charging. a2), b2), c2) and d2) are the higher magnification details from the areas marked by the yellow rectangles in a1), b1), c1) and d1), respectively. The blue dashed lines in a1), b1), c1) and d1) describe the transition boundary between brittle and ductile fracture.

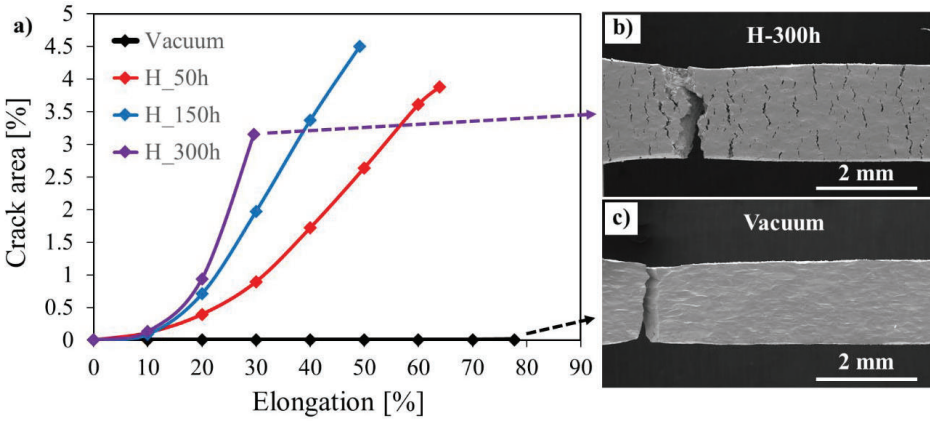

Fig. 7. (a) The evolution of secondary crack area at different charging conditions. The fracture gauge surface of sample with 300 h pre-charged hydrogen (b) and without pre-charging (c).

Fig. 8 shows the SEM image with the corresponding EBSD characterizations of typical secondary cracks on gauge surface after failure on the specimen with 300 h pre-charged hydrogen. The paths of secondary surface cracks are in general perpendicular to the global tensile direction. To investigate the secondary cracks at a microstructural level, EBSD scan was performed in the area highlighted in Fig. 8a. It can be seen from Fig. 8b that all the secondary cracks have been initiated at grain boundaries and propagated in an intergranular manner. No transgranular-type cracks can be detected. Fig. 8c shows the Kernel Average Misorientation (KAM) map of the same area. This method calculates the average misorientation from the surrounding points regarding the scanned point, and this criterion is used to evaluate the local deformation and local dislocation density of each scanned point. It can be seen from the map that a higher KAM value is always found at grain boundaries, implying that grain boundary is a favored place for deformation concentration. Along cracked boundaries, the KAM value is not significantly higher than the deformation-concentrated areas along non-cracked boundaries and the area with higher KAM value is rather confined to the cracks, suggesting a brittle cracking manner with limited plastic deformation mechanism. Fig. 8d shows the boundary map over the same area with high angle grain boundaries (HAGBs, >15°), low angle grain boundaries (LAGBs, 2-15°) and twin boundaries. The LAGBs appear at the places roughly the same as the deformation-concentrated areas revealed by the KAM map, indicating a deformation-nature of the LAGBs. An interesting feature is that most of the intergranular cracks

are connected to some twin boundaries. Most of the intersecting twins are mechanical twins since they appear as thin bands. No clear dependency can be found on the annealing twins.

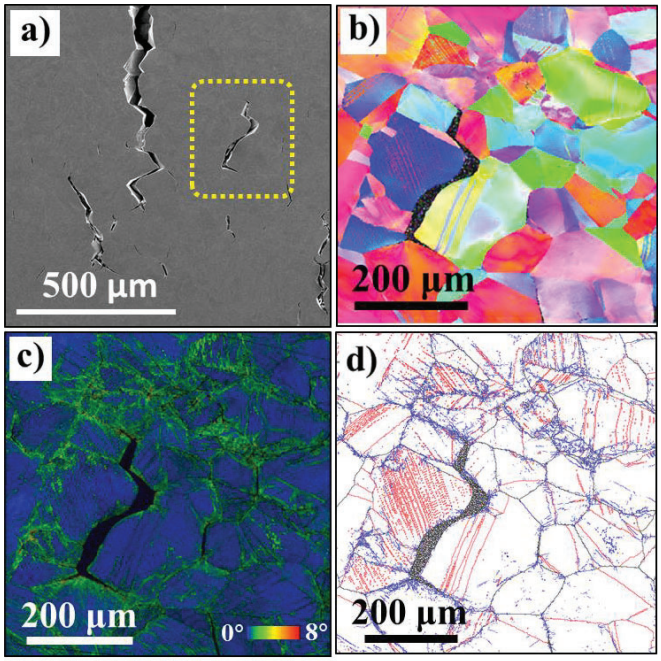

Fig. 8. a) SEM image showing surface cracks; b) ND-IPF map; c) KAM map and d) boundary map with black lines showing HAGB, blue lines showing LAGB and red lines showing twin boundary. b)-d) are the same area as highlighted in a). The tensile direction is horizontal for all images.

4. Discussion

4.1 Hydrogen influence on the strength

The general hydrogen influence on the mechanical performance of metallic materials is a decrease in the ductility, referred as embrittlement effect. However, the hydrogen influence on the strength is not clear yet. Different studies have shown different effects including both hardening [36, 37] and softening [38, 39]. But a common agreement has not been reached yet.

To estimate the effect of hydrogen on the strength of the material in the current study, true stress - true strain curves are needed. The solid curves in Fig. 9 are the calculated true stress - true strain curves based on the conventional approach by assuming a constant gauge volume during tension. From the solid curves, a decreasing true stress is displayed for all three hydrogen-charged specimens, showing a softening-like behavior. However, since the hydrogen-induced crack formation on the gauge surface during tension is detected (as shown in the video 2-4 in the supplementary document), which makes the estimated cross-section area larger than the real case, the conventional method of calculating true stress is not an appropriate approach. As a result, the calculated true stress values would be underestimated. To improve the accuracy of the estimation, correct load and correct area of the cross-section are needed. An assumption is thus made here: the ductile area on the fracture surface indicates the contact area at the maximum load, while the brittle area on the fracture surface has been developing before reaching the maximum load. Therefore, we took the maximum load divided by the ductile fracture area as the true UTS value. By this method, the calibrated true UTS values are shown as solid diamonds in Fig. 9. Worthy of note, the true UTS value of the hydrogen-free specimen from this method shows good agreement with the value from conventional method. However, the hydrogen-charged cases show higher true UTS values than the conventional curves. The dashed curves are plotted to estimate the true stress in the intermediate stage. Though these curves cannot correctly reflect the real true stress, they can be used to express the continuous evolution of the values in this stage. Based on these curves, surprisingly, a hardening effect of hydrogen instead of softening is clearly observed at a same strain level. With the increasing hydrogen-charging time (referring to a higher hydrogen content), the hardening effect becomes more significant. Recently, the effect of hydrogen on strength has also been studied by fatigue crack growth testing showing a hydrogen-restricted plasticity evolution [40, 41] and nanoindentation testing showing a hydrogen-enhanced lattice friction [11]. These studies as well as the current work show a similar hardening effect of hydrogen.

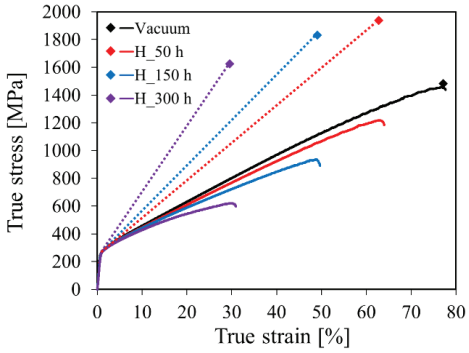

Fig. 9. True stress - true strain curves of specimens with different pre-charged hydrogen.

4.2 Hydrogen induced fracture mode transition

The hydrogen contents after different pre-charging time were measured by TDS tests and the corresponding values are shown in Fig. 5. The concentration of hydrogen on the sample surface C_s can be estimated based on the total dissolved hydrogen content according to the method proposed by Pontini and Hermida [42] as follows:

$$C_s = \frac{\omega C_M}{4}\sqrt{\frac{\pi}{Dt}} \tag{2}$$

where ω is the sample thickness, C_M is the total dissolved hydrogen content measured by TDS tests, t is the hydrogen pre-charging time, and D is the hydrogen diffusion coefficient at the charging temperature of 80 °C. The D value used in Eq. 2 was calculated as 4.36×10^{-15} m^2/s by setting diffusion activation energy as 30.4 kJ/mol [43] and diffusion coefficient value at room temperature as 5.24×10^{-16} m^2/s [15]. The surface contents C_s after 50, 150, and 300 h pre-charging were calculated as 145.6, 151.3, and 152.7 wppm, respectively. These values were similar with each other with a difference less than 5%. The hydrogen concentration $C(x,t)$ after different charging time t at the depth of x can be further calculated by using the Fick's law-based "semi-infinite" model [44]:

$$\frac{C(x,t)-C_0}{C_s-C_0} = 1-\mathrm{erf}\left(\frac{x}{\sqrt{4Dt}}\right) \tag{3}$$

$$\mathrm{erf}(u) = \frac{2}{\sqrt{\pi}} \int_0^u \exp(-u^2)\, du \tag{4}$$

where C_0 is the original hydrogen content dissolved in specimen as 0.02 wppm as shown in Fig. 5. Fig. 10 shows the hydrogen concentration profiles after different pre-charging conditions with respect to depth. The hydrogen concentration exhibits considerable decrease immediately below the sample surface, which is a common feature in FCC alloys during electrochemical hydrogen charging due to their low hydrogen diffusivity [45]. The longer charging time yields a richer hydrogen content at the same depth, and a deeper hydrogen penetration depth can also be obtained.

The brittle area after different pre-charging time can be measured from fractographies shown in Fig. 6 and the corresponding depths are marked as black vertical dashed lines in Fig. 10. By comparing the critical hydrogen content at the ductile-to-brittle transit boundary, a common value of 22 wppm can be found for each charging condition as the threshold value. This result means that the area below sample surface charged by hydrogen to a certain amount (22 wppm) and above would cause brittle failure upon further mechanical loading.

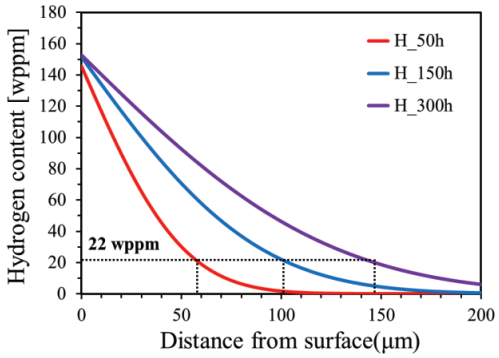

Fig. 10. Hydrogen concentration profiles of samples with different pre-charging time. The black dashed lines indicate the depth of brittle fracture with corresponding hydrogen content.

4.3 Hydrogen-assisted secondary crack during deformation

As illustrated in the tensile videos attached in the supplementary document as well as the fracture surfaces shown in Fig. 6, no detectable intergranular fracture was observed on the specimen without hydrogen pre-charging and the final fracture surface was pure ductile. As a contrast, the

failure of the hydrogen charged specimens showed a mixture of brittle intergranular fracture near surface and ductile transgranular dimples close to the center, and no evidence of apparent necking was detected before the failure. This behavior has been commonly observed in hydrogen embrittlement studies on other FCC alloys [9, 46]. In addition, a large number of secondary cracks were observed on the gauge surface of pre-charged samples during tensile tests. EBSD analysis (Fig. 8) shows that these secondary cracks are pure intergranular. The secondary cracks along both grain boundaries and twin boundaries were reported in the former studies [6, 47]. However, in the current study, all cracks were along grain boundaries and no cracks along twin boundaries were detected. This difference might come from different charging conditions and different heat treatments.

To illustrate the microstructural features on secondary crack initiation and propagation paths, we statistically analyzed the overall grain boundary distribution on the pre-charged specimens before test. Additionally, the grain boundary types of the initiated secondary cracks after 10% straining and after fracture were also analyzed to investigate the cracking preferences. Fig. 11 shows the results of the aforementioned analysis on the 300 h pre-charged sample. The grain boundary distribution was characterized by EBSD mapping on the gauge surface at three stages: before tensile test, at 10% strain, and after failure. Before tensile test (Fig. 11a) and after failure (Fig. 11c), more than 100 original grain boundaries and secondary cracks were measured. For the stage of tensile till 10% strain, all the initiated secondary cracks on the gauge surface were characterized. Fig. 11a-c show the SEM images of the three stages and Fig. 11d-f illustrate the corresponding distribution of grain boundary as a function of misorientation angle.

As shown in Fig. 11d, the initial microstructure contains 5.7% LAGBs and 94.3% HAGBs. Among the HAGB, a large fraction was detected between the misorientation angle of 40-45°. After 10% strain, a slightly larger fraction (97.4%) of cracks has been initiated at HAGBs, while only 2.6% of them has been initiated at LAGBs. In the fracture stage, 97.2% of the cracks have been propagating along HAGBs and 2.8% of them have been propagating along LAGBs, as shown in Fig. 11f. It is clear that less LAGBs have cracked but more HAGBs have cracked during the tensile loading. The similar statistically values from the 10% elongated specimen and the fractured specimen indicate that during crack propagation, the initiated cracks have not been significantly deflected to other type of GBs in a global sense. By comparing the fraction of cracks with the original microstructure, the LAGBs exhibited better resistance to both crack initiation and

propagation. No specific HAGB (regarding misorientation) can be determined as preferential cracking sites, since they showed a similar misorientation distribution as original microstructure. The observation of LAGB being crack initiation/propagation resistant has also been proposed in pure Ni by Bechtle et al. [48], who found that a higher proportion of LAGB reduces the hydrogen-induced intergranular embrittlement. This crack resistant property of LAGB might come from their more ordered structure, which leads to a lower local hydrogen diffusivity and thus impedes the hydrogen transportation and segregation [49]. As a result, the formation of new vacancies and the reduction of grain boundary cohesive strength are minimized. Another possible reason for the better crack resistance of LAGBs is their higher boundary separation energy [50], which makes these boundaries more resistant to fracture.

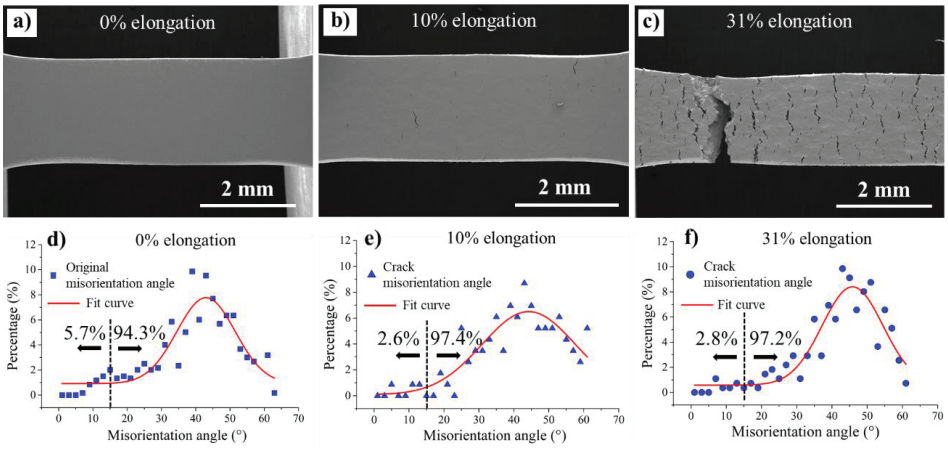

Fig. 11. SEM images of specimens after 300 h hydrogen pre-charging at different strains: (a) before tensile test with 0% elongation, (b) at 10% elongation, (c) after fracture at 31% elongation. Statistical analysis of secondary crack initiation and propagation: (d) the fraction of total grain boundary types. the fraction of grain boundary types that (e) initiate cracks and (f) susceptible to crack propagation. The black dotted line in (d), (e), and (f) are the dividing line between LAGBs and HAGBs.

4.4 Mechanism of secondary intergranular cracking

It has been seen from the EBSD analysis that most of the typical secondary cracks are intersecting with some mechanical twins (Fig. 8). However, since the step size of the EBSD scan was relatively large, some small-scale mechanical twins could not be correctly detected. To further investigate the interaction between the deformation twins and the cracked boundaries, ECCI was conducted near the cracked boundaries. Fig. 12 shows the ECC images demonstrating the initiated secondary cracks on the gauge surface of specimen with 50 h pre-charged hydrogen after 10% elongation. By tilting the specimen to an optimized contrast condition, the matrix background in ECC image appears as dark due to its low backscattering yield. While dislocations appear as white contrast on the dark background due to the interaction between dislocations and matrix surface, and the stacking faults appear as bright areas with a white straight line on one side, indicating the interaction between the stacking fault planes and the sample surface [51]. All the ECCI results show a clear intergranular crack as exhibited in Fig. 12a1, b1, and c1. The formed cracks were along grain boundaries with impinged thick deformation twinning bands at a relative perpendicular angle (measured as 78° and 98° in Fig. 12a2 and b2, respectively). The propagation of the crack with an increased opening angle can be detected at the intersections between crack and deformation twinning bands as shown in Fig. 12a2. Moreover, the intergranular crack propagation was stopped when no further deformation twinning bands intersect with the grain boundary, as shown in Fig. 12b2 and c2. Fig. 12b2 shows a stoppage of crack when the grain boundary intersect only with stacking faults, and Fig. 12c2 exhibits the grain boundary with no initiated cracks when only a small quantity of thin deformation twins was intersected. This indicates that the grain boundaries intersected with thick deformation twinning bands act as the preferential sites for crack initiation and propagation paths. In addition, the intersection angle between deformation twinning band and grain boundary is also a decisive factor for the crack initiation. As shown in Fig. 12c1, parallel twinning bands intersecting with a curved grain boundary at different angles. When the low intersect angle (28°) was applied, no initiated cracks can be detected even at the triple junction of grain boundaries, which were proposed to be more vulnerable to hydrogen-assisted intergranular cracking due to the stress concentration [52]. By contrast, cracks (Fig. 12c1) were observed when the intersection angle increased to a value that close to perpendicular angle. Specifically, a crack was detected at the high intersect angle (76°) within the same system containing a same grain boundary and an even thinner deformation band compared with the non-crack sites shown above.

The stress concentration together with the hydrogen effect on grain boundaries intersecting with thick deformation twins are the reasons for the crack initiation and propagation. The deformation twin induced grain boundary failure has been demonstrated by both experimental work [53] and molecular dynamics simulation [54]. It proposed that high stress concentration, high dislocation density, and high lattice rotation would be developed at the grain boundaries intersected with deformation twins due to the incompatible plastic deformation. A recent study has shown that the stress concentration induced by mechanical twinning intercepting with GBs is high enough to initiate the plastic deformation both in the original grain and in the neighboring grain [55]. Moreover, a thicker deformation twin results in a higher concentrated stress, leading to intergranular cracking by nucleation of microcracks and coalescence of voids. On the other hand, grain boundaries are known as preferential sites for hydrogen trapping and segregation [56]. The large amount of segregated hydrogen on the grain boundary would promote the vacancies formation [57] and reduce the grain boundary cohesive energy [58], which further results in intergranular failure.

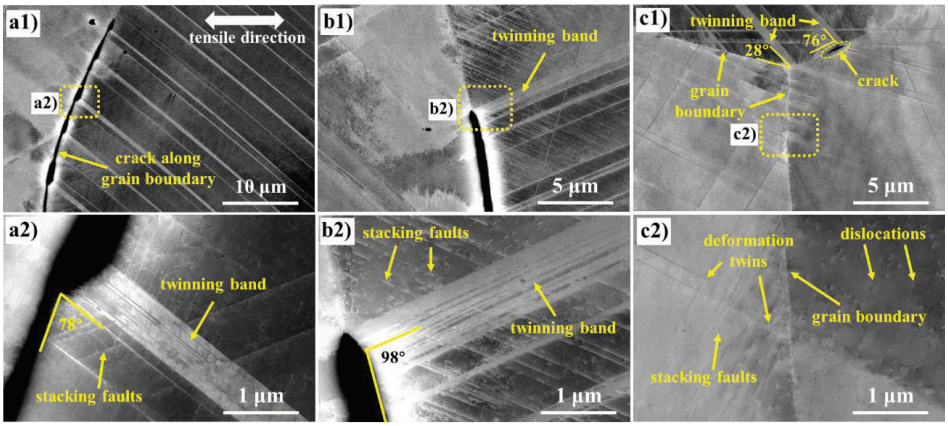

Fig. 12. ECC images showing the intergranular secondary cracks on the gauge surface of specimen with 50 h pre-charged hydrogen at 10% strain. The tensile direction is along horizontal direction for all images. a2), b2), and c2) show the areas highlighted by yellow rectangles in a1), b1), and c1), respectively.

5. Conclusion

In this study, the susceptibility of hydrogen embrittlement on Fe-22Mn-0.6C TWIP steel was investigated by tensile tests with in-situ SEM observation. The tests were performed on non-charged specimen and on hydrogen pre-charged specimens with different pre-charging time (50, 150, and 300 h). By further TDS hydrogen content measurement and post-mortem SEM, EBSD and ECCI characterizations, some conclusions can be drawn as follows:

1. The presence of hydrogen has a strong detrimental effect on both the tensile strength and fracture elongation. The fracture surface of the uncharged sample was pure ductile with fully-covered dimple structure. By contrast, brittle intergranular fracture surface was observed in the vicinity of sample surface on hydrogen charged samples. Moreover, a longer charging time results in a higher dissolved hydrogen content. The different amount of charged hydrogen showed an accumulatively effect on the mechanical property degradation and led to a deeper ductile-to-brittle transition depth. A specific amount of hydrogen (22 wppm) was determined as the threshold value for this ductile-to-brittle transition.

2. During the tensile tests, the secondary cracks on gauge surface were detected only on the charged specimens. All these cracks were nucleated on the grain boundaries and propagated in an intergranular manner. The amount and area occupation of secondary cracks increased as the increasing of charging time and tensile elongation. By further statistical analysis on the secondary cracks, it shows that the LAGBs have a better resistance to crack initiation and propagation compared with the HAGBs.

3. The grain boundaries that intersect with thick deformation twins are the preferential crack initiation sites and propagation paths. This is due to the stress concentration at these intersecting points in combination with the intrinsic hydrogen effect on grain boundaries. The intersecting angle can influence the stress concentration and thus influence the cracking behaviors.

Acknowledgements

The authors are grateful for the support provided by Research Council of Norway through the HyF-Lex (244068/E30) project and the promotion of scientific exchange by German Research Foundation in the framework of Collaborative Research Center SFB 761 “Steel - ab initio.”. The

author (Dong Wang) would like to acknowledge the financial support from the China Scholarship Council.

References

[1] B.C. De Cooman, Y. Estrin, S.K. Kim, Twinning-induced plasticity (TWIP) steels, Acta Mater. 142 (2018) 283-362.
[2] O. Grassel, L. Kruger, G. Frommeyer, L.W. Meyer, High strength Fe-Mn-(Al, Si) TRIP/TWIP steels development-properties-application, Int. J. Plast. 16(10-11) (2000) 1391-1409.
[3] S. Curtze, V.T. Kuokkala, Dependence of tensile deformation behavior of TWIP steels on stacking fault energy, temperature and strain rate, Acta Mater. 58(15) (2010) 5129-5141.
[4] D.T. Pierce, J.A. Jiménez, J. Bentley, D. Raabe, J.E. Wittig, The influence of stacking fault energy on the microstructural and strain-hardening evolution of Fe–Mn–Al–Si steels during tensile deformation, Acta Mater. 100 (2015) 178-190.
[5] M. Koyama, E. Akiyama, Y.K. Lee, D. Raabe, K. Tsuzaki, Overview of hydrogen embrittlement in high-Mn steels, Int. J. Hydrog. Energy 42(17) (2017) 12706-12723.
[6] M. Koyama, E. Akiyama, K. Tsuzaki, D. Raabe, Hydrogen-assisted failure in a twinning-induced plasticity steel studied under in situ hydrogen charging by electron channeling contrast imaging, Acta Mater. 61(12) (2013) 4607-4618.
[7] Q.L. Liu, Q.J. Zhou, J. Venezuela, M.X. Zhang, J.Q. Wang, A. Atrens, A review of the influence of hydrogen on the mechanical properties of DP, TRIP, and TWIP advanced high-strength steels for auto construction, Corros. Rev. 34(3) (2016) 127-152.
[8] Y. Bai, Y. Momotani, M.C. Chen, A. Shibata, N. Tsuji, Effect of grain refinement on hydrogen embrittlement behaviors of high-Mn TWIP steel, Mater. Sci. Eng. A 651 (2016) 935-944.
[9] M. Koyama, E. Akiyama, K. Tsuzaki, Hydrogen embrittlement in a Fe-Mn-C ternary twinning-induced plasticity steel, Corros. Sci. 54 (2012) 1-4.
[10] K.G. Chin, C.Y. Kang, S.Y. Shin, S. Hong, S. Lee, H.S. Kim, K.H. Kim, N.J. Kim, Effects of Al addition on deformation and fracture mechanisms in two high manganese TWIP steels, Mater. Sci. Eng. A 528(6) (2011) 2922-2928.
[11] D. Wang, X. Lu, Y. Deng, X. Guo, A. Barnoush, Effect of hydrogen on nanomechanical properties in Fe-22Mn-0.6C TWIP steel revealed by in-situ electrochemical nanoindentation, Acta Mater. 166 (2019) 618-629.
[12] X. Lu, D. Wang, Z. Li, Y. Deng, A. Barnoush, Hydrogen susceptibility of an interstitial equimolar high-entropy alloy revealed by in-situ electrochemical microcantilever bending test, Mater. Sci. Eng. A 762 (2019) 138114.
[13] N. Zan, H. Ding, X.F. Guo, Z.Y. Tang, W. Bleck, Effects of grain size on hydrogen embrittlement in a Fe-22Mn-0.6C TWIP steel, Int. J. Hydrog. Energy 40(33) (2015) 10687-10696.
[14] Y.J. Kwon, T. Lee, J. Lee, Y.S. Chun, C.S. Lee, Role of Cu on hydrogen embrittlement behavior in Fe-Mn-C-Cu TWIP steel, Int. J. Hydrog. Energy 40(23) (2015) 7409-7419.
[15] Y.J. Kwon, H.J. Seo, J.N. Kim, C.S. Lee, Effect of grain boundary engineering on hydrogen embrittlement in Fe-Mn-C TWIP steel at various strain rates, Corros. Sci. 142 (2018) 213-221.
[16] B. Bal, M. Koyama, G. Gerstein, H.J. Maier, K. Tsuzaki, Effect of strain rate on hydrogen embrittlement susceptibility of twinning-induced plasticity steel pre-charged with high-pressure hydrogen gas, Int. J. Hydrog. Energy 41(34) (2016) 15362-15372.
[17] H.K. Birnbaum, P. Sofronis, Hydrogen-enhanced localized plasticity—a mechanism for hydrogen-related fracture, Mater. Sci. Eng. A 176(1) (1994) 191-202.
[18] P. Ferreira, I. Robertson, H. Birnbaum, Hydrogen effects on the interaction between dislocations, Acta Mater. 46(5) (1998) 1749-1757.

[19] W. Gerberich, Modeling hydrogen induced damage mechanisms in metals, in: R.P. Gangloff, B.P. Somerday (Eds.), Gaseous Hydrogen Embrittlement of Materials in Energy Technologies, Woodhead Publishing2012, pp. 209-246.
[20] Z. Tarzimoghadam, M. Rohwerder, S.V. Merzlikin, A. Bashir, L. Yedra, S. Eswara, D. Ponge, D. Raabe, Multi-scale and spatially resolved hydrogen mapping in a Ni-Nb model alloy reveals the role of the δ phase in hydrogen embrittlement of alloy 718, Acta Mater. 109 (2016) 69-81.
[21] S.P. Lynch, Environmentally Assisted Cracking: Overview of Evidence for an Adsorption-Induced Localized-Slip Process, Acta Metall. 36(10) (1988) 2639-2661.
[22] S. Lynch, Hydrogen embrittlement phenomena and mechanisms, Corros. Rev. 30(3-4) (2012) 105-123.
[23] S. Hinotani, Y. Ohmori, F. Terasaki, Effect of Nickel on Hydride Formation and Hydrogen Embrittlement in Ni-Cr-Fe Alloys, Mater. Sci. Eng. 74(2) (1985) 119-131.
[24] M. Nagumo, Hydrogen related failure of steels - a new aspect, Mater. Sci. Technol. 20(8) (2004) 940-950.
[25] I.M. Robertson, The effect of hydrogen on dislocation dynamics, Eng. Fract. Mech. 68(6) (2001) 671-692.
[26] L.B. Pfeil, The effect of occluded hydrogen on the tensile strength of iron, Proceedings of the Royal Society of London. Series A, Containing Papers of a Mathematical and Physical Character 112(760) (1926) 182-195.
[27] A. Metsue, A. Oudriss, X. Feaugas, Trapping/detrapping kinetic rates of hydrogen around a vacancy in nickel and some consequences on the hydrogen-vacancy clusters thermodynamic equilibrium, Comp. Mater. Sci. 151 (2018) 144-152.
[28] M. Hatano, M. Fujinami, K. Arai, H. Fujii, M. Nagumo, Hydrogen embrittlement of austenitic stainless steels revealed by deformation microstructures and strain-induced creation of vacancies, Acta Mater. 67 (2014) 342-353.
[29] S. Zaefferer, N.N. Elhami, Theory and application of electron channelling contrast imaging under controlled diffraction conditions, Acta Mater. 75 (2014) 20-50.
[30] X. Lu, D. Wang, D. Wan, Z.B. Zhang, N. Kheradmand, A. Barnoush, Effect of electrochemical charging on the hydrogen embrittlement susceptibility of Alloy 718, Acta Mater. 179 (2019) 36-48.
[31] D. Wang, X. Lu, Y. Deng, D. Wan, Z. Li, A. Barnoush, Effect of hydrogen-induced surface steps on the nanomechanical behavior of a CoCrFeMnNi high-entropy alloy revealed by in-situ electrochemical nanoindentation, Intermetallics 114 (2019) 106605.
[32] D. Wang, X. Lu, D. Wan, Z. Li, A. Barnoush, In-situ observation of martensitic transformation in an interstitial metastable high-entropy alloy during cathodic hydrogen charging, Scr. Mater. 173 (2019) 56-60.
[33] S. Allain, P. Cugy, C. Scott, J.P. Chateau, A. Rusinek, A. Deschamps, The influence of plastic instabilities on the mechanical properties of a high-manganese austenitic FeMnC steel, Int. J. Mater. Res. 99(7) (2008) 734-738.
[34] J.E. Jin, Y.K. Lee, Strain hardening behavior of a Fe-18Mn-0.6C-1.5Al TWIP steel, Mater. Sci. Eng. A 527(1-2) (2009) 157-161.
[35] T. Depover, T. Hajilou, D. Wan, D. Wang, A. Barnoush, K. Verbeken, Assessment of the potential of hydrogen plasma charging as compared to conventional electrochemical hydrogen charging on dual phase steel, Mater. Sci. Eng. A 754 (2019) 613-621.
[36] C. Verpoort, D.J. Duquette, N.S. Stoloff, A. Neu, The Influence of Plastic-Deformation on the Hydrogen Embrittlement of Nickel, Mater. Sci. Eng. 64(1) (1984) 135-145.

[37] D.P. Abraham, C.J. Altstetter, The Effect of Hydrogen on the Yield and Flow Stress of an Austenitic Stainless Steel, Metall. Mater. Trans. A 26(11) (1995) 2849-2858.
[38] D.F. Teter, I.M. Robertson, H.K. Birnbaum, The effects of hydrogen on the deformation and fracture of beta-titanium, Acta Mater. 49(20) (2001) 4313-4323.
[39] G.M. Bond, I.M. Robertson, H.K. Birnbaum, Effects of Hydrogen on Deformation and Fracture Processes in High-Purity Aluminum, Acta Metall. 36(8) (1988) 2193-2197.
[40] D. Wan, A. Alvaro, V. Olden, A. Barnoush, Hydrogen-enhanced fatigue crack growth behaviors in a ferritic Fe-3wt%Si steel studied by fractography and dislocation structure analysis, Int. J. Hydrog. Energy 44(10) (2019) 5030-5042.
[41] D. Wan, Y. Deng, J.I.H. Meling, A. Alvaro, A. Barnoush, Hydrogen-enhanced fatigue crack growth in a single-edge notched tensile specimen under in-situ hydrogen charging inside an environmental scanning electron microscope, Acta Mater. 170 (2019) 87-99.
[42] A.E. Pontini, J.D. Hermida, X-ray diffraction measurement of the stacking fault energy reduction induced by hydrogen in an AISI 304 steel, Scr. Mater. 37(11) (1997) 1831-1837.
[43] I.J. Park, K.H. Jeong, J.G. Jung, C.S. Lee, Y.K. Lee, The mechanism of enhanced resistance to the hydrogen delayed fracture in Al-added Fe-18Mn-0.6C twinning-induced plasticity steels, Int. J. Hydrog. Energy 37(12) (2012) 9925-9932.
[44] V. Olden, C. Thaulow, R. Johnsen, Modelling of hydrogen diffusion and hydrogen induced cracking in supermartensitic and duplex stainless steels, Mater. Des. 29(10) (2008) 1934-1948.
[45] J.A. Ronevich, S.K. Kim, J.G. Speer, D.K. Matlock, Hydrogen effects on cathodically charged twinning-induced plasticity steel, Scr. Mater. 66(12) (2012) 956-959.
[46] K.E. Nygren, K.M. Bertsch, S. Wang, H. Bei, A. Nagao, I.M. Robertson, Hydrogen embrittlement in compositionally complex FeNiCoCrMn FCC solid solution alloy, Curr. Opin. Solid State Mater. Sci. 22(1) (2018) 1-7.
[47] M. Seita, J.P. Hanson, S. Gradecak, M.J. Demkowicz, The dual role of coherent twin boundaries in hydrogen embrittlement, Nat. Commun. 6 (2015).
[48] S. Bechtle, M. Kumar, B.P. Somerday, M.E. Launey, R.O. Ritchie, Grain-boundary engineering markedly reduces susceptibility to intergranular hydrogen embrittlement in metallic materials, Acta Mater. 57(14) (2009) 4148-4157.
[49] A. Oudriss, J. Creus, J. Bouhattate, E. Conforto, C. Berziou, C. Savall, X. Feaugas, Grain size and grain-boundary effects on diffusion and trapping of hydrogen in pure nickel, Acta Mater. 60(19) (2012) 6814-6828.
[50] T. Watanabe, The impact of grain boundary character distribution on fracture in polycrystals, Mater. Sci. Eng. A 176(1) (1994) 39-49.
[51] I. Gutierrez-Urrutia, S. Zaefferer, D. Raabe, Electron channeling contrast imaging of twins and dislocations in twinning-induced plasticity steels under controlled diffraction conditions in a scanning electron microscope, Scr. Mater. 61(7) (2009) 737-740.
[52] B.A. Wilcox, G.C. Smith, Intercrystalline fracture in hydrogen-charged nickel, Acta Metall. 13(3) (1965) 331-343.
[53] H. Abdolvand, A.J. Wilkinson, Assessment of residual stress fields at deformation twin tips and the surrounding environments, Acta Mater. 105 (2016) 219-231.
[54] Y. Zhang, P.C. Millett, M. Tonks, B. Biner, Deformation-twin-induced grain boundary failure, Scr. Mater. 66(2) (2012) 117-120.
[55] D. Wan, A. Barnoush, Plasticity in cryogenic brittle fracture of ferritic steels: Dislocation versus twinning, Mater. Sci. Eng. A 744 (2019) 335-339.

[56] A. Oudriss, S. Le Guernic, Z. Wang, B. Osman Hoch, J. Bouhattate, E. Conforto, Z. Zhu, D.S. Li, X. Feaugas, Meso-scale anisotropic hydrogen segregation near grain-boundaries in polycrystalline nickel characterized by EBSD/SIMS, Mater. Lett. 165 (2016) 217-222.
[57] A. Metsue, A. Oudriss, X. Feaugas, Hydrogen solubility and vacancy concentration in nickel single crystals at thermal equilibrium: New insights from statistical mechanics and ab initio calculations, J. Alloys Compd. 656 (2016) 555-567.
[58] R.A. Oriani, P.H. Josephic, Equilibrium Aspects of Hydrogen-Induced Cracking of Steels, Acta Metall. 22(9) (1974) 1065-1074.

Paper II

Effect of hydrogen on nanomechanical properties in Fe-22Mn-0.6C TWIP steel revealed by in-situ electrochemical nanoindentation

Dong Wang, Xu Lu, Yun Deng, Xiaofei Guo, Afrooz Barnoush

Acta Mater. 166 (2019) 618-629.

Effect of hydrogen on nanomechanical properties in Fe-22Mn-0.6C TWIP steel revealed by in-situ electrochemical nanoindentation

Dong Wang, Xu Lu, Yun Deng, Xiaofei Guo, Afrooz Barnoush

Abstract: In-situ electrochemical nanoindentation was applied to study the effect of hydrogen on the mechanical properties of Fe-22Mn-0.6C TWIP steel at the nanoscale. Distinctive behaviors in three defined grain orientations: (001), (101), and (111) were investigated in a sequence of air, hydrogen ingress, and hydrogen egress processes. The obvious pop-in load drop caused by introducing hydrogen was analyzed using the classical dislocation theory in combination with the "Defactants" model, wherein hydrogen-enhanced homogenous dislocation nucleation through the reduction of the dislocation line energy and the stacking fault energy were proposed as the reasons. The dependence of pop-in behaviors on the crystallographic orientations was also discussed. Tabor relation-based models were applied to analyze the nanohardness increment, which was related to the hydrogen-enhanced lattice friction and the hydrogen-reduced plastic zone size. The different recovery behaviors of the pop-in load and nanohardness during hydrogen egress were assessed according to the different amounts of residual hydrogen in the corresponding affected zone.

Keywords: Hydrogen embrittlement; Electrochemical nanoindentation; TWIP steel; Dislocation nucleation; Nanohardness

1. Introduction

High-Mn twinning-induced plasticity (TWIP) steels have been intensively studied for years owing to their outstanding mechanical properties, including high strength and good ductility [1, 2]. With a pure austenite microstructure, the main strengthening mechanisms of TWIP steels consist of both plasticity-induced dislocation slip and the twinning effect due to their low stacking fault energy (SFE) [3-5]. Therefore, TWIP steels are promising material for cold-forming components in the automotive industry and other energy-related infrastructures. However, this steel is susceptible to unexpected mechanical degradation when exposed to hydrogen-containing environments owing to hydrogen embrittlement (HE) [6-8], which is in accordance with the concept of hydrogen-induced degradation of metals with a transition from ductile to brittle behavior [9]. Although substantial research has been performed to elucidate the mechanism of hydrogen-induced premature failure,

no consensus has been reached. Several mechanisms, including hydrogen-enhanced decohesion (HEDE), hydrogen-enhanced localized plasticity (HELP), adsorption-induced dislocation emission (AIDE), and the "Defactants" model, have been proposed according to microscopic observations.

The HEDE mechanism, which was proposed by Troiano [10], involves the accumulation of dissolved hydrogen atoms at trapping sites such as cracks or interfaces, which reduces the cohesive energy of atomic planes or grain boundaries. When the applied stress exceeds the cohesive stress, cracks occur and propagate, resulting in cleavage failure [11, 12], which is widely accepted for explaining intergranular fracture [13, 14]. The HELP mechanism is primarily based on in-situ environmental transmission electron microscopy (TEM) observations of the enhanced dislocation motion and the decreased dislocation interactions in hydrogen-charged samples [15-17]. The enhanced dislocation mobility causes material softening, which is supported by observations of the reduction of the yield stress and flow stress in hydrogenated materials through tensile test [18, 19]. The subdued dislocation interactions are explained by the shielding effect of hydrogen, which facilitates planar slip and promotes pile-up phenomena based on the elastic theory [20, 21]. Besides, the HELP mechanism is also supported by the appearance of quasi-cleavage fracture and surface slip line rearrangement in hydrogen charged samples [22-25]. It is further proved by atomistic simulation [26], and thermodynamic calculations [27-29]. However, contradictory results showing the increase of the flow stress due to the presence of hydrogen are common in aluminum alloys and austenitic steels at high strain levels [30, 31]. Similarly, hydrogen hardening effect were also reported in bcc iron through both experimental and simulation work [32-35]. Moreover, Song and Curtin proposed that hydrogen provides no shielding effect for dislocation interactions and even weakens the dislocation mobility instead of facilitating it, which is consistent with the solute drag theory based on atomic simulations [36, 37]. The AIDE theory states that the dislocation formation energy is reduced by hydrogen at the crack tips and that the crack propagation is therefore enhanced by easier dislocation emission from the crack tip at relatively low stresses [38, 39]. The "Defactants" concept, which relies on thermodynamics, involves the reduction of the formation energy of defects (such as dislocations) in the presence of defactant solutes, such as hydrogen [27, 28, 40, 41]. In fact, HE is a complex process depending heavily on the material and environment, no aforementioned mechanisms can apply exclusively. For example, in the process of hydrogen-induced crack propagation, dislocations first nucleate at the crack tip based on AIDE and then

steady move away due to the enhanced mobility according to HELP [42]. Furthermore, these mechanisms are not completely distinct but with some overlap between each other. AIDE and "Defactants" contain aspects that are also described in HELP is a case in point [29, 39]. To date, most studies on TWIP steels have been dedicated to understanding the mechanisms of HE by altering the alloying elements, microstructure, and testing parameters. As the most common alloying element in TWIP steels, aluminum was proven to improve the resistance to hydrogen delayed fracture by forming an aluminum oxide layer during electrochemical charging, which prevents hydrogen absorption [43]. The addition of aluminum was also reported to enhance the resistance to HE by reducing the hydrogen mobility [33]. However, controversial results showed that aluminum addition has a beneficial effect only in high-strain rate tensile tests, while it is detrimental and promotes crack formation during low-cycle fatigue tests [34]. Copper was reported to have a similar effect to aluminum, while titanium had a negative effect on the HE resistance [44, 45]. Grain refinement was also proposed as a method for enhancing the resistance to HE in TWIP steels by suppressing the ductile-to-brittle transition through the reduction of twin-related boundaries and junctions [46]. In addition, the effect of the strain rate on the HE was analyzed for pre-charged TWIP steels, revealing that the HE becomes more pronounced at a lower strain rate, which enhances the twin-slip interaction by thinning the twins and results in quasi-cleavage fracture [47]. Most investigations focused on macroscopic mechanical testing, which reflects the combined effects of different lattice defects, whereby it is difficult to clarify the intrinsic influence of dislocations, stacking faults, twinning nucleation, etc. Therefore, investigation at the microscale is needed for a better understanding of the degradation process. Recently, the in-situ hydrogen charging technique showed advantages in studying the HE behavior by eliminating the hydrogen diffusion during tests, especially for body-centered cubic metals that have a high hydrogen diffusion rate [6, 7]. Therefore, it is necessary to integrate in-situ hydrogen charging into the microscale testing.

The electrochemical nanoindentation (ECNI) technique, which was proposed by Barnoush [48], has proven to be suitable for probing the hydrogen effect on the mechanical properties of metals in-situ [49, 50]. With the recorded high-resolution load–displacement (L-D) data, not only can the mechanical properties, such as the Young's modulus and nanohardness, be calculated, but also the discrete events, including dislocation nucleation and phase transformation, can be detected in the process of hydrogen charging [49, 51]. In the present study, ECNI tests were performed within

single crystals with three defined grain orientations: (001), (101), and (111) to understand the effects of hydrogen absorption and desorption on the mechanical behaviors of TWIP steel and the associated HE mechanisms.

2. Experimental

2.1 Materials and sample preparation

The studied material was Fe-22Mn-0.6C (wt. %) TWIP steel with the chemical composition shown in Table 1. The material was ingot casted, hot rolled, and cold rolled to a thickness of 1.0 mm, followed by grain growth annealing at 1,150 °C for 5 h in an argon atmosphere. The samples used for the ECNI tests were cut via electrical discharge machining into discs with a diameter of 12 mm. The samples were ground sequentially using 220–4,000 grit SiC papers and then polished to 1 μm, followed by additional polishing with a 40-nm colloidal silica suspension for 20 min to remove the deformation layer. The surface quality was checked by using the scanning mode of the nanoindenter, and the final surface root-mean-square roughness was <1 nm over 64 μm^2.

Table 1
Chemical composition of the investigated Fe-22Mn-0.6C TWIP steel

Element	C	Mn	Al	Nb	Ti	V	N	Fe
wt. %	0.63	22.60	0.008	0.03	0.03	0.108	0.016	Bal.

The microstructure of the studied material was analyzed using a high-resolution scanning electron microscope (SEM, Quanta FEG 650 ESEM, FEI Inc.) with a backscatter electron (BSE) detector. Fig. 1(a) shows the microstructure of the tested material, which consisted of grains with an equiaxed morphology and annealing twins. The electron backscatter diffraction (EBSD) technique was used to eliminate the influence of different grain orientations by choosing three defined grains with orientations close to (001), (101), and (111) (i.e. [001], [101], [111] // ND, respectively) as shown in the normal direction-inverse pole figure (ND-IPF) in Fig. 1(b). The measured Euler angles (Bunge definition) of the chosen grains are (41°, 2°, 46°), (88°, 92°, 47°), and (11°, 52°, 46°), respectively, which meet the aforementioned orientation expectations. These ND orientations

are also the uniaxial indentation directions during the tests. For simplicity and more explicit description, only Miller indices are used hereafter. The studied material had an average grain size of 85 μm, which was large enough for performing repeated ECNI tests under all charging conditions within a single grain to exclude the influences of the grain size and grain orientation.

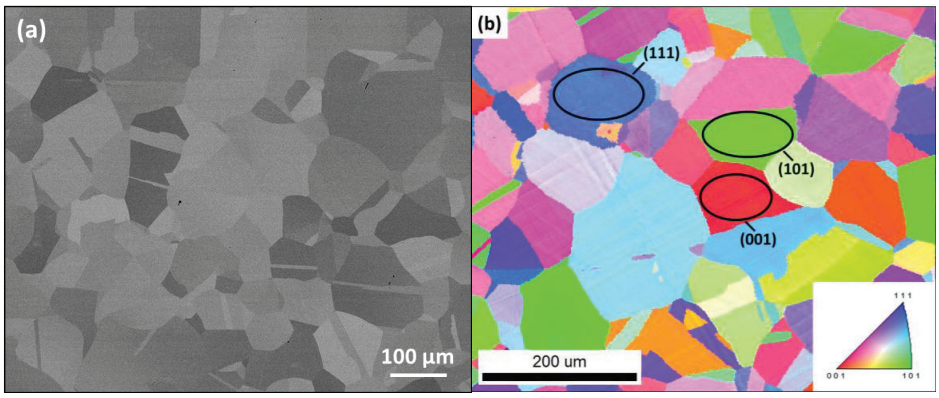

Fig. 1. (a) BSE image showing the microstructure of the investigated sample. (b) ND-IPF map of the tested sample with marked (001), (101), and (111) grains.

2.2 Polarization curve

To determine the appropriate charging potentials for the ECNI tests, the polarization curve was measured before the ECNI tests. The electrolyte used for the polarization curve measurement and the following in-situ ECNI test was a glycerol-based solution. The solution consisted of 600 g of Borax (sodium tetraborate decahydrate) dissolved in 1 L of glycerol and diluted with 20% distilled water [52]. In addition, 0.002 M $Na_2S_2O_3$ was added to promote hydrogen absorption [53]. The extremely low solubility and diffusivity of oxygen in the developed electrolyte gave it the advantage of preserving the surface integrity throughout the ECNI test. A three-electrode electrochemical cell consisting of a platinum counter electrode and a $Hg/HgSO_4$ reference electrode was built. Additional details regarding the in-situ setup are presented in Ref. [41]. The polarization curve was measured with a scanning rate of 1 mV/s from -2,500 to 1,000 mV.

The polarization curve is presented in Fig. 2(a), with three chosen potentials highlighted by horizontal dashed lines. The sample exhibited cathodic behavior from -2,500 to -1,100 mV, where hydrogen was produced as the main reaction and diffused into the material. A more negative cathodic potential resulted in a higher current density. The anodic branch started when the potential was higher than -1,100 mV, where a passive region between -500 and 500 mV was obtained. In this test, -1,250 and -2,000 mV were chosen as cathodic polarization potentials to charge the sample, and 0 mV was chosen as the anodic potential, at which hydrogen diffused out but the sample surface could be kept free of corrosion.

2.3 In-situ ECNI test

In-situ ECNI tests were performed using Hysitron Tribo-Indenter TI 950 with a Berkovich diamond tip, which was also used to scan the sample surface after each group of indentations. The surface topography images were analyzed using Gwyddion software to trace the change of the surface roughness.

The sample was first tested in air, followed by a sequence of -1,250 and -2,000 mV cathodic charging and 0 mV anodic discharging. Before ECNI tests at each cathodic potential, the sample was charged for 2 h for enough hydrogen to be absorbed into the sample. During anodic discharging, the indentations were performed after 2 and 20 h to capture the time-effect of the nanomechanical properties. At least 27 indentations were performed in each condition to guarantee the reproducibility of the results.

The load function used for the test is shown in Fig. 2(b). It consists of a loading segment with an 8,000 μN/s loading rate until the peak load of 2,000 μN is reached, with a holding time of 0.45 s, followed by an 8,000 μN/s unloading segment until 10% of the peak value is reached, with holding for 0.25 s for drift correction.

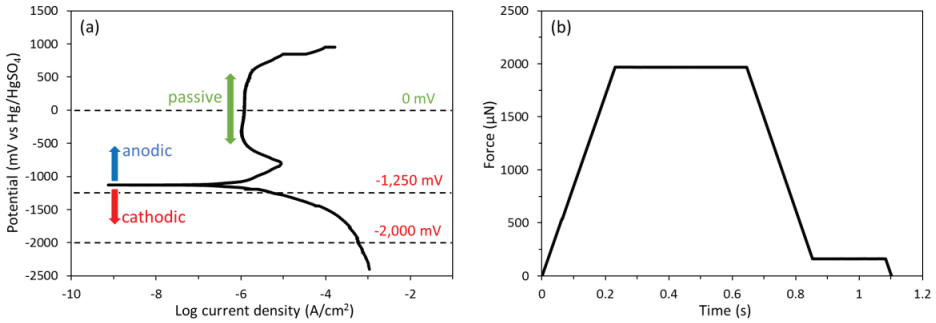

Fig. 2. (a) Polarization curve of the investigated TWIP sample. The horizontal dashed lines represent the chosen potentials for the ECNI tests. (b) Curve of the load function used for the test.

2.4 Electron channeling contrast imaging (ECCI)

After the nanoindentation (NI) test, the sample was carefully cleaned with distilled water and ethanol. Postmortem analysis was performed using an SEM via the ECCI technique. ECCI has been established as an excellent SEM method based on the controlled diffraction condition with an enhanced contrast [4, 54]. It allowed us to examine the complex deformation microstructure and crystal defects, such as dislocations and stacking faults within the visibility depth below the surface of the metallic materials. In this test, ECCI observations were used to probe the plastic zone produced by the NI test. The test was performed at an acceleration voltage of 30 kV with a working distance of 6 mm, and the sample was properly tilted to a certain angle to obtain a good channeling condition according to the EBSD adjustment.

3. Results

3.1 Hydrogen effect on nanomechanical properties

The representative L-D curves of the tested grains under different testing conditions are shown in Figs. 3(a)–3(c). All the L-D curves in (101) and (111) grains clearly show four stages: initial elastic loading; an excursion in depth (pop-in), which refers to the onset of plasticity due to homogenous dislocation nucleation (HDN); subsequent elastoplastic loading; and elastic unloading. However, the unique multiple pop-in phenomenon is observed in (001) grain in each testing condition, where

the higher pop-ins are proven to result from the nucleation of twins [55]. Except for the initial elastic loading, all the loading stages show differences among different testing conditions. A reduced pop-in load and width, as well as hardening behavior, are observed in the cathodic charging conditions, and the alteration becomes more obvious with the increase of the charging potentials. After the potential is switched to 0 mV, fast recovery of the pop-in behavior and steady recovery of the hardness are observed. During the whole test, the surface roughness that was continuously inspected exhibited no alteration, as shown in Figs. 3(d)–3(g). Therefore, the observed changes of the mechanical properties under different conditions were not due to the change in the surface condition by the electrolyte, but rather due to the dissolved hydrogen.

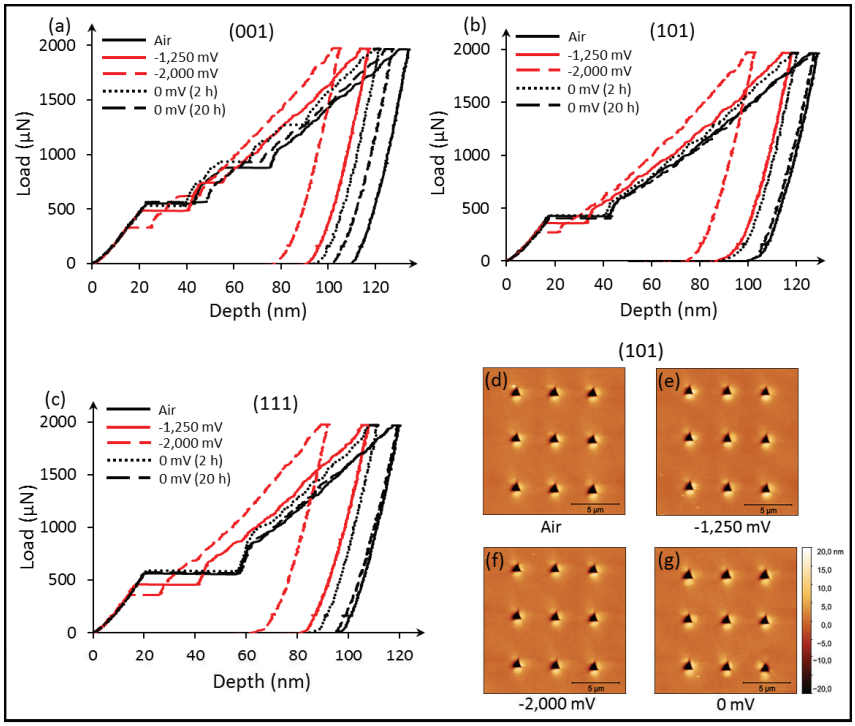

Fig. 3. Representative L-D curves for (a) (001) grain, (b) (101) grain, and (c) (111) grain tested in air, under two charging conditions and two anodic conditions. (d–g) Representative topographies after indentation in (d) air and at (e) -1,250 mV, (f) -2,000 mV, and (g) 0 mV (after 20 h) in (101) grain.

In the case of pop-in load, which indicates the onset of plasticity, the effects of hydrogen for each grain orientation are detailed in Figs. 4(a) and 4(b). For (111) grain, the average pop-in load in air was 544 μN, and the pop-in load decreased to 450 μN (reduction of 17.3%) when the sample was cathodically charged at -1,250 mV. The pop-in load further decreased to 380 μN (reduction of 30.1%) at -2,000 mV. After switching to anodic discharging condition, the average pop-in load recovered to the air-value within 2 h and remained unchanged till 20 h of discharging. The amount of hydrogen dissolved into the material in the processes of cathodic charging and anodic discharging will be discussed in detail in section 4.3. Compared with (111) orientation, the pop-in load for (101) orientation exhibited the same trend during the adsorption and desorption of hydrogen, except with different values and a slightly less pronounced effect of hydrogen. In contrast to the single pop-in in (101) and (111) grains, (001) grain exhibited multiple pop-in behavior. Fig. 4(b) shows the cumulative frequency distribution of the first and second pop-ins in (001) grain. Here, we observe a clear drop in both cases when hydrogen was introduced and a recovery of the pop-in load when the hydrogen was removed.

To further analyze the effect of hydrogen on the mechanical properties of the studied material, the nanohardness of the elastic unloading parts was determined using the Oliver–Pharr method [56]:

$$\mathrm{H} = \frac{P_{max}}{A_c}, \tag{1}$$

where P_{max} is the maximum load during the NI test, and A_c is the projected contact area according to the tip area function and the tip contact depth h_c, which can be calculated as follows:

$$h_c \cong h_{max} - 0.75\frac{P_{max}}{S}. \tag{2}$$

Here, h_{max} is the maximum displacement during the NI test, and S is the stiffness extracted from the initial unloading slope of the L-D curve. Clearly, the hardness is increased by introducing hydrogen under cathodic charging and is increased continuously by increasing the cathodic potential. However, in contrast to the pop-in behavior, which recovers in 2 h with the removal of hydrogen, the hardness recovers gradually, exhibiting a time-effect. Taking (101) grain as an example, the hardness value in air is 3.68 GPa, and it increases by 19.0% to 4.38 GPa and by 46.2% to 5.38 GPa at -1,250 and -2,000 mV, respectively. After switching to anodic discharging for 2 h,

the hardness first decreases to 4.27 GPa, which is still 16.0% higher than that in air. It decreases to 3.83 GPa after 20 h of discharging. (001) and (111) grains show the same hardness time-effect.

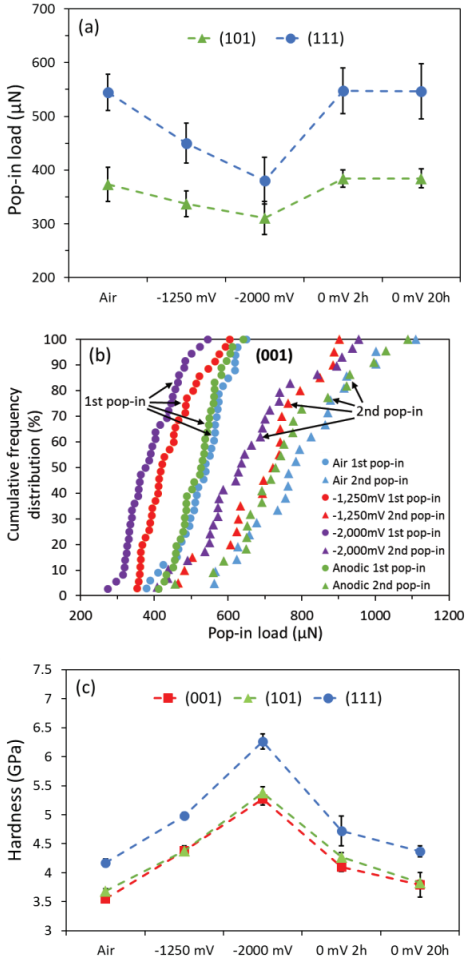

Fig. 4. Pop-in load of (a) (101) and (111) grains and (b) (001) grain; hardness values (c) under different hydrogen absorption and desorption conditions.

3.2 Microstructure after indentation

The representative electron channeling contrast (ECC) images of the indents that were tested in air and under two charging conditions for (101) grain are shown in Figs. 5(a1)–5(a3) and 5(b1)–5(b3).

With the applied electron acceleration voltage and the activated diffraction vector, the visibility depth was theoretically 80–100 nm [57]. The dislocations appear as white curved lines or dots on the dark background, while the stacking faults appear as bright areas with a white straight line on one side, indicating the interaction between the stacking fault plane and the sample surface [54]. In the ECC images, both the dislocations and the stacking faults produced in the NI test are clearly observed. Therefore, the contact radius a_c and the plastic zone radius a_{pz} can be estimated. According to a finite-element simulation [58], the plastic zone is designated as the area with more than 1%–2% plastic strain. Thus, the single dislocations or stacking faults that reside far away from the indent center are precluded owing to their negligible effect on the material strength. This is also proved by Choi et al. [59] suggesting that the area of highest dislocation densities used for counting the plastic zone is measured up to a radius approximately half as large as the radius of the total dislocation area. Magnified images of the highlighted indents are shown in Figs. 5(b1)–5(b3), where the radius of the solid circles is a_c and the radius of the dashed circles is a_{pz}. According to our measurement, the average sizes of both a_c and a_{pz} were reduced after electrochemical charging. The effect of hydrogen on the plasticity zone size can be expressed by the ratio of a_{pz} to a_c, which was calculated as 1.63, 1.52, and 1.40 in air and at -1,250 and -2,000 mV, respectively, showing that the plastic zone area detected via ECCI was reduced in the presence of hydrogen. The localized plasticity is also indicated by the topography and pile-up. Figs. 5(c1)–5(c3) present the two-dimensional (2D) color-filled contour images for different charging conditions, and Figs. 5(d1)–5(d3) show the height data for the three dashed lines in Figs. 5(c1)–5(c3). The height of the pile-ups increased from 10 nm in air to 13 and 15 nm in -1,250 and -2,000 mV cathodic charging conditions, respectively. Normally, in a load-controlled NI test, the total deformation is reflected by the summation of the plastic zone and pile-up. Additionally, the deformation degree should be proportional to the maximum indentation depth. Fig. 3(b) shows that the maximum indentation depth in (101) grain was smaller in cathodic charging condition than in air or anodic charging condition, which indicates less deformation in the presence of hydrogen. Thus, more pile-ups in the charging condition confirmed more pronounced shrinkage of the plastic zone surrounding the indents. The more confined plastic zone in the hydrogen charging condition proves that hydrogen dragged dislocation motion and restricted the dislocation cross slip due to the enhanced slip planarity in the frame of the HELP mechanism.

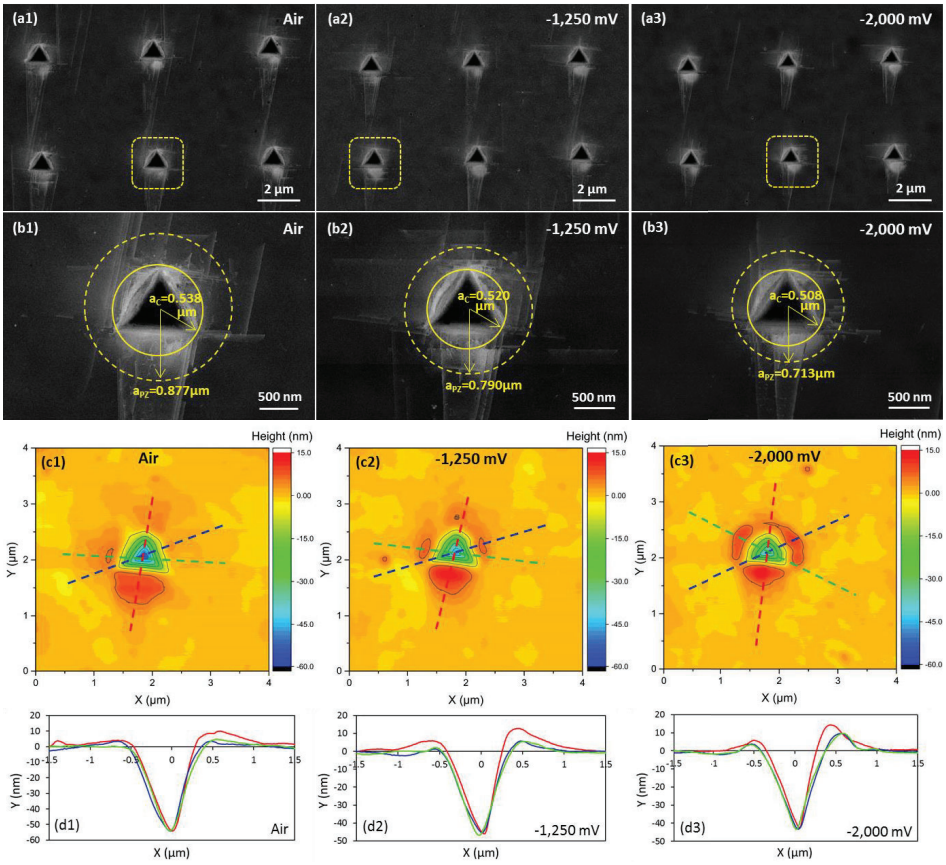

Fig. 5. Groups (a) and (b) contain ECC images of the representative indents. Group (b) contains magnified images of the indents indicating the contact area and the plastic zone. Group (c) contains the 2D color-filled contour plots showing the surface topography, and group (d) contains plots of the related pile-up data. The numbers (1), (2), and (3) represent the different testing conditions: air, -1,250 mV, and -2,000 mV, respectively. All the images are for the (101) grain.

4 Discussion

4.1 Hydrogen effect on dislocation and twin nucleation

To understand the effect of hydrogen on the elastic behavior of the material, the Hertzian contact theory was applied to model the elastic interactions between the indenter and the surface [60]:

$$\mathrm{P} = \frac{4}{3} E_r \sqrt{R h^3} \ , \tag{3}$$

where P is the applied load, h is the indentation depth, R is the radius of the tip curvature, and E_r is the reduced modulus. According to the Oliver–Pharr method [56], the reduced modulus can be measured by analyzing the elastic unloading part of the L-D curve, as follows:

$$E_r = \frac{\sqrt{\pi}}{2} \frac{1}{\beta} \frac{S}{\sqrt{A_c}}, \tag{4}$$

where β is a correction factor based on the geometry of the indenter tip (1.034 for Berkovich indenter). Using the calculated E_r values, it is possible to estimate the radius of the tip curvature by applying the Hertzian fit according to Eq. (3). In the present study, the Berkovich tip radius was 1.0 μm.

According to the contact mechanics, the elastic loading starts from the contact between the tip and the surface until the first dislocation nucleation and motion occur, which indicates the onset of plasticity [41, 60]. For an annealed metallic material, the typical dislocation density is in the range of 10^{10}–10^{14} m^{-2}, which means that dislocations are separated by 1–10 μm. Because the elastic region probes a depth of approximately 20 nm before the occurrence of pop-in phenomena, as shown in Fig. 3, the indented volume in the elastic area is 100 times smaller than the average dislocation space. Thus, it is reasonable to assume that the areas where the indents are performed contain no pre-existing dislocations. The absence of pre-existing dislocations means that the elastic loading continues until the shear stress beneath the tip reaches the theoretical shear stress, where the HDN occurs with the pop-in phenomena, followed by subsequent dislocation gliding and other motion events [49, 60].

According to the classical dislocation theory [61], the free energy required to form a dislocation loop with a radius of r is described as

$$\Delta \mathrm{G} = 2\pi r W_{dis} + \pi r^2 \gamma - \pi r^2 b \tau_{max} \ , \tag{5}$$

where W_{dis} is the line energy of the newly formed dislocation loop, γ is the SFE, which is 0.023 J/m^2 for the studied steel [59], and b is the Burgers vector of partial dislocation (0.15 nm) [5]. The term $2\pi r W_{dis}$ represents the line energy of the whole dislocation loop, the term $\pi r^2 \gamma$ represents

the formation energy of a stacking fault, and the last term represents the work needed for expanding the dislocation loop.

For visualizing the energy needed to generate a dislocation loop, the maximum shear stress τ_{max} for HDN [62, 63] and the line energy W_{dis} of a circular dislocation loop in an infinite isotropic elastic solid [61] can be obtained as follows:

$$\tau_{max} = 0.31\left(\frac{6E_r^2}{\pi^3 R^2}P\right)^{\frac{1}{3}} \tag{6}$$

$$W_{dis} = \frac{2-\upsilon}{1-\upsilon}\frac{\mu b^2}{8\pi}\left(\ln\frac{4r}{\psi} - 2\right), \tag{7}$$

where υ is the Poisson's ratio (0.27), μ is the shear modulus, and ψ is the dislocation core radius ($\sim\frac{b}{2}$). The shear modulus μ can be calculated using the Poisson's ratio υ and the elastic modules E as follows: $\mu = E/2(1+\upsilon)$. The elastic modulus is given by

$$\frac{1}{E_r} = \frac{1-\upsilon_1^2}{E_1} + \frac{1-\upsilon_2^2}{E_2}. \tag{8}$$

Here, the subscripts 1 and 2 represent the sample and the tip, respectively. For a diamond tip, the elastic modulus is 1,140 GPa, and the Poisson's ratio is 0.07. By combining Eqs. (6) and (7), the free energy of dislocation loop formation can be expressed as

$$\Delta G = \frac{2-\upsilon}{1-\upsilon}\frac{\mu b^2 r}{4}\left(\ln\frac{4r}{\psi} - 2\right) + \pi r^2\gamma - \pi r^2 b\tau_{max}\,. \tag{9}$$

Fig. 6 shows the free energy of HDN as a function of the dislocation loop radius in different charging conditions for the defined orientations. All the free-energy curves pass through a maximum value ΔG^* at the critical loop radius r^*, where ΔG^* is defined as the activation energy for HDN and can be calculated by setting $\frac{\delta\Delta G}{\delta r} = 0$. To obtain a stabilized dislocation loop, the activation energy must overcome the energy barrier, ΔG^* in this case, for the dislocation to grow larger than r^*. It was reported that the available thermal energy at room temperature is 0.0026 eV [41]. Therefore, the dislocation loop is nucleated spontaneously and the pop-in can be observed only for a maximum free energy ΔG^* lower than 0.0026 eV. This is exactly what occurred during the NI test in the air and anodic conditions. When the sample was charged with hydrogen, the

calculated ΔG^* was significantly higher than 0.0026 eV in all cases. According to the previous thermodynamic assumptions, the dislocation loop is not supposed to nucleate. Nonetheless, all the recorded L-D curves for the cathodic conditions clearly exhibit pop-in phenomena, which means that the existing energy barriers at the cathodic potentials were somehow overcome by the dissolved hydrogen. This can be explained by the "Defactants" model, which proposes that hydrogen can reduce the formation energy of defects, such as dislocations and stacking faults, and enhance the defect formation [27, 28, 40]. For a linear dislocation, the hydrogen segregation around the dislocation line can effectively increase the dislocation core radius [64, 65], reducing the line energy of the dislocation according to Eq. (7). The reduction of the SFE by hydrogen has been demonstrated via both experiment and simulation [66, 67]. Therefore, the dissolved hydrogen results in easier formation of the dislocation loop and stacking fault during NI, which is reflected by the reduction of the pop-in load in the L-D curves. This defect-reduction phenomenon becomes more pronounced with more absorbed hydrogen, as shown in Fig. 4.

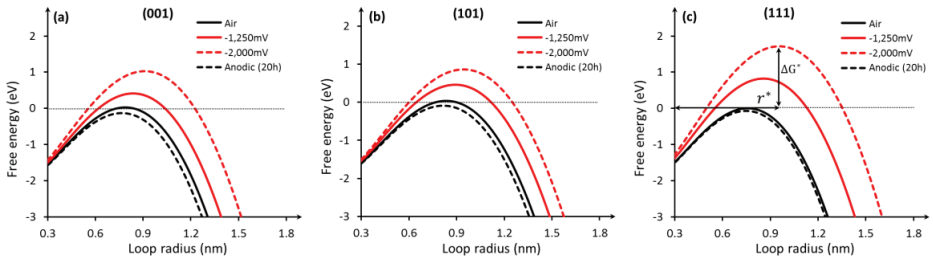

Fig. 6. Free energy of HDN with respect to the dislocation loop radius (r) for (001) (a), (101) (b), and (111) (c) grain orientations. The activation energy for HDN (ΔG^*) and the critical loop radius (r^*) in the -2,000 mV charging condition are shown in (c).

Additionally, the crystallographic orientation is an important factor determining the mechanical properties and deformation behaviors of crystalline alloys. According to Fig. 4, the orientation-dependent pop-in behaviors can be summarized as follows. 1) The L-D curves in (001) grain are more complicated with multiple pop-ins. 2) The average pop-in load in (111) grain is higher than that in (101) grain under all testing conditions. The orientation dependence of the uniaxial yield stress can be expressed by the variation of Schmid factors in different slip planes. Normally for a tensile test, the slip system with the largest Schmid factor experiences the highest shear stress and

will be activated first when the critical shear stress is reached. Although the stress state beneath the indenter is not comparable to the uniaxial tensile test due to the complexity below the indenter tip, it is reasonable to consider the indentation process as an uniaxial compression for simplicity [68] and use Schmid factor to help understanding the dislocation slip behavior in each grain orientation. The maximum Schmid factors for dislocation slip system {111}<110> and mechanical twinning system {111}<112> are presented in Table 2 [69]. The Schmid factor for mechanical twinning in (001) grain is approximately two times higher than that for (101) and (111) grains; thus, mechanical twinning occurs more easily. Considering the multiple pop-in behavior in (001) grain, it is reasonable to propose that the second and subsequent pop-ins are related to the nucleation of deformation twins. It needs to mention here that mechanical twinning can only occur after the activation of multiple slip systems although the highest Schmid factor for twinning is larger than that for slip as in (001) grain [70, 71]. Gutierrez-Urrutia et.al. [72] reported the evidence in TWIP steel that once multiple slip is activated, twinning occurs readily. Furthermore, the association between the pop-ins and deformation twins in TWIP steel was also proposed by Misra [55], who performed TEM analysis indicating that the first pop-in is nucleation of dislocation, while subsequent pop-ins are related to deformation twinning. For (101) and (111) grains, with lower Schmid factors for mechanical twinning compared with that for slip, dislocation slip is more favorable, which results in single pop-ins on L-D curves, indicating dislocation nucleation. However, the Schmid factor for dislocation slip is 0.41 in (101) grain, which is 1.464 times higher than that in (111) grain (0.28). Therefore, the critical resolved shear stress for slip is expected to be reached earlier with a lower pop-in load in (101) grain than in (111) grain. According to the data in Fig. 4, the average pop-in loads in air are 373.16 GPa in (101) grain and 544.41 GPa in (111) grain, differing by a factor of 1.459, which perfectly matches the ratio of their Schmid factors.

Table 2
Maximum Schmid factors of different orientations under compression for preferred dislocation slip system {111}<110> and mechanical twinning system {111}<112> [69]

Deformation mode	Orientation		
	(001)	(101)	(111)
Dislocation slip	0.41	0.41	0.28
Mechanical twinning	0.47	0.25	0.16

4.2 Hydrogen effect on lattice friction

As shown in Fig. 3, the dissolved hydrogen not only reduces the pop-in load but also influences the elastoplastic part of the L-D curves, with a hardening effect. To elucidate this effect, the models developed by Nix-Gao and Durst are introduced [73, 74]. The elastoplastic curve can be described by the models according to the Tabor relation:

$$\mathrm{P} = \mathrm{H}_0 A_c \,, \tag{10}$$

where A_c is the contact area used in Section 3.1, and H_0 is the depth-independent hardness of the material obtained from the NI test, which can be expressed as follows.

$$\mathrm{H}_0 = \mathrm{C}\sigma \,. \tag{11}$$

Here, C is the Tabor factor transforming the complex stress state beneath the indenter into a uniaxial stress state [60]. In the current study, the Tabor factor C is assumed as 3 [75]. Because the NI test was performed on defined grains that can be treated as a single crystal, the hardening mechanisms induced by the grain boundaries and phase boundaries are ignored. Hence, the stress σ is assumed to be influenced only by the lattice friction (σ_{Fric}) and the interaction between dislocations, which is described as Taylor stress (σ_{Taylor}). W. S. Choi et al. [59] found that the lattice friction stress σ_{Fric} in polycrystalline Fe-22Mn-0.6C TWIP steel was 242 MPa by considering the solid solution strengthening effect. The Taylor stress (σ_{Taylor}) is described by the Taylor relation [74]:

$$\sigma_{Taylor} = M\alpha\mu b\sqrt{\rho_{dis}} \,, \tag{12}$$

where M is the Taylor factor, which is reported to be 3.06 [59], and α is an empirical factor depending on the dislocation structure. Owing to the complex stress field beneath the indenter, a constant value of $\alpha = 0.5$ is chosen [73]. The dislocation density ρ_{dis} consists of the statistically stored dislocation (SSD) density, ρ_{SSD}, and the geometrically necessary dislocation (GND) density, ρ_{GND}. For our annealed sample with a deformation-free surface, it is reasonable to assume that the ρ_{SSD} value is 10^{12} m^{-2}. GNDs are accumulated in strain gradient fields caused by geometrical constraints of the crystal lattice, and the density is described according to the Nix-Gao model [74]:

$$\rho_{GND} = \frac{3}{2}\frac{1}{f^3}\frac{\tan^2\theta}{bh} \,, \tag{13}$$

where θ is the angle between the sample surface and the indenter, which is 24.63° for the Berkovich tip, and f is the ratio of the plastic zone radius to the contact area radius (a_{pz}/a_c) described in Section 3.2. By combining Eqs. (10)–(13), the elastoplastic regime can be described as follows.

$$\mathrm{P} = \mathrm{CM}\alpha\mu\mathrm{b}A_c\sqrt{\rho_{SSD} + \frac{3}{2}\frac{1}{f^3}\frac{\tan^2\theta}{bh}} + \mathrm{C}\sigma_{Fric}A_c\,. \tag{14}$$

The results are shown in Fig. 7, where the fitting curves obtained using Eq. (14) by inserting the f value of 1.63 obtained from Section 3.2 are fully consistent with the experimental data obtained in air. To explain the hydrogen effect on the elastoplastic regime, we assume that the dissolved hydrogen has an influence on both σ_{Fric} and σ_{Taylor}. As mentioned previously, the electrochemical hydrogen charging process was performed such that the formation of defects was avoided. Therefore, it is reasonable to assume that the dissolved hydrogen has no effect on ρ_{SSD} but influences σ_{Fric} and ρ_{GND}. Eq. (14) can therefore be rearranged as

$$\mathrm{P} = \mathrm{CM}\alpha\mu\mathrm{b}A_c\sqrt{\rho_{SSD} + \frac{3}{2}\frac{1}{{f_H}^3}\frac{\tan^2\theta}{bh}} + \mathrm{C}(\sigma_{Fric} + \sigma_H)A_c\,, \tag{15}$$

where σ_H is the contribution of the dissolved hydrogen to the lattice friction, and f_H is the hydrogen-affected ratio of the plastic zone radius to the contact radius, which can be obtained from the ECCI results in Section 3.2. The value of σ_H can be quantitatively calculated by fitting the experimental data in the hydrogen-charged condition using Eq. (15). The fitted σ_H values in different conditions together with the most relevant parameters used for the simulation are presented in Table 3. In the case of (101) grain orientation, with the introduction of hydrogen, the lattice friction shows an increment of 45 MPa at -1,250 mV and increases to 210 MPa at -2,000 mV. The same trend is observed for (111) grain orientation, with values of 75 and 340 MPa, respectively. The lattice friction in (001) grain cannot be determined, owing to the limited elastoplastic part with multiple pop-ins, which makes it difficult to fit using Eq. (15). Regardless, it is reasonable to infer that the increment of the lattice friction is due to the interactions between dislocations and dissolved hydrogen atoms. Because the depth of indents is limited to ~100 nm, the dissolved hydrogen in this area is sufficient to generate Cottrell atmospheres around the moving dislocations, resulting in a resistance to dislocation motion, which is consistent with the

solute drag theory [61]. This idea is supported by the atomistic simulation results of Song and Curtin [37]. Therefore, the hardening effect of hydrogen can be explained by the increment of the lattice friction and the reduction of f. A larger amount of hydrogen generated by adjusting the cathodic potential yielded a more pronounced hardening effect, as shown in Fig. 4(c).

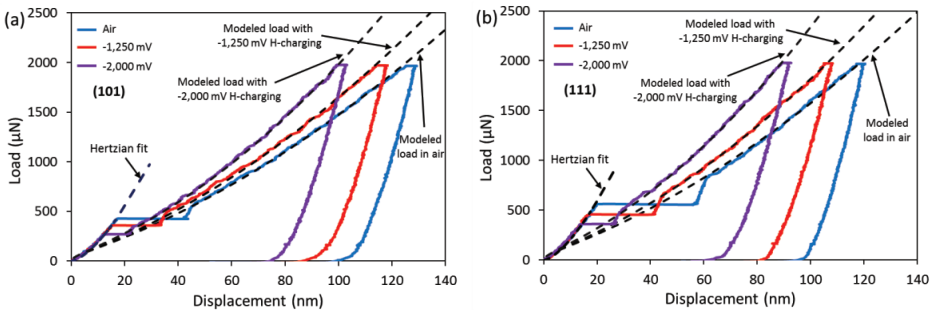

Fig. 7. Typical L-D curves of the (a) (101) grain and (b) (111) grain obtained in air and different H-charging conditions. The elastic regimes are fitted by Hertzian model. The elastoplastic parts are modeled according to Eqs. (14) and (15).

Table 3. Sets of parameters used for modeling the L-D curves

	Values	Physical meaning
C	3	Tabor factor
M	3.06	Taylor factor
α	0.5	Empirical factor
b	0.15 nm	Burgers vector partial dislocation
ρ_{SSD}	10^{12} m^{-2}	SSD
σ_{Fric}	242 MPa	Lattice friction
θ	24.63°	Indenter factor
μ	61 GPa (101)	Shear modulus
	66 GPa (111)	
f	1.63 (air)	$\frac{\text{Plastic zone radius}}{\text{Contact area radius}}$
	1.52 (-1,250 mV)	
	1.40 (-2,000 mV)	
σ_H (101)	45 MPa (-1,250 mV)	Hydrogen contribution to lattice friction
	210 MPa (-2,000 mV)	
σ_H (111)	75 MPa (-1,250 mV)	
	340 MPa (-2,000 mV)	

4.3 Anodic time-effect on nanohardness

The results in Fig. 4 show the unambiguous effect of hydrogen on the pop-in behavior and the hardness of TWIP steel. Generally, with dissolved hydrogen, the pop-in load decreases and the hardness increases. However, an interesting feature is observed when the hydrogen desorption begins. With anodic charging for 2 h, the pop-in loads recover to values that are consistent with the data obtained in air (Figs. 4(a) and 4(b)). In contrast, the hardness recovers slowly, exhibiting a time-effect (Fig. 4(c)): after 2 h of discharging, the hardness for (001), (101), and (111) grain orientations show only 68.4%, 65.3%, and 73.8% recovery, and after 20 h of discharging, the hardness values recover by 88.3%, 91.6%, and 90.5%, respectively. The variation of the recovery behaviors for the pop-in load and hardness is attributed to the different affecting depths beneath the indenter. According to continuum mechanics, the maximum shear stress for pop-in during an NI test occurs below the sample surface, within a distance of 0.48 times the contact radius r_c [60]. The contact radius r_c and the position of the maximum shear stress $Z_{\tau(max)}$ are calculated as follows [76].

$$r_c = \left(\frac{3PR}{4E_r}\right)^{\frac{1}{3}}. \tag{16}$$

$$Z_{\tau(max)} = 0.48 r_c = 0.48\left(\frac{3PR}{4E_r}\right)^{\frac{1}{3}}. \tag{17}$$

By substituting the tip radius of 1 μm, the pop-in load, and the reduced modulus into the above equations, the affected maximum shear stress depth $Z_{\tau(max)}$, which is in the range of 60 ± 3 nm, can be calculated. Therefore, the energy for the onset of dislocation, i.e., the HDN, is determined by the perceptive stress in this depth range.

On the contrary, the hardness response of the sample is determined by the aforementioned lattice friction and the Taylor stress. The hardness is dominated by the plastic zone beneath the indenter. Several models for probing the plastic zone size have been proposed [58, 77, 78]. Among them, the model developed by Lawn et al. [79] relates the plastic zone radius r_{pz} to the residual indentation depth h_f:

$$r_{pz} = \varphi \left(\frac{E}{H}\right)^{n} tan^{\frac{1}{3}}(\theta) h_f \,, \tag{18}$$

where φ is the geometry constant (3.64 for Berkovich [80]). E is the elastic modulus calculated from the reduced modulus based on Eq. (8). θ takes the same value as in Eq. (13). The constant n was originally suggested to be 1/2 and was optimized as 1/3 [81]. By substituting the calculated $\frac{E}{H}$ values in different conditions, r_{pz} is calculated in the range of 835 ± 25 nm. Notably, the radius of the plastic zone measured from the ECC images is between 790 and 877 nm, which agrees with the Lawn model. Therefore, during the ECNI tests, the dissolved hydrogen depth influencing the hardness was significantly larger than that affecting the pop-in load.

To further analyze the variation of the hydrogen concentration during charging and discharging, Fick's law is used to describe the diffusion process beneath the sample surface. During cathodic charging, the exit side of the sample has marginal or no influence on the hydrogen concentration. We can consider the diffusion process by using "the thick plate solution" model [82]:

$$\frac{C(x,t) - C_0}{C_i - C_0} = 1 - \mathrm{erf}\left(\frac{x}{\sqrt{4Dt}}\right) \tag{19}$$

$$\mathrm{erf}(u) = \frac{2}{\sqrt{\pi}} \int_0^u \exp(-u^2)\, du \,, \tag{20}$$

where $C(x,t)$ is the concentration of hydrogen in the sample, C_i is the constant surface hydrogen concentration, C_0 is the uniform initial bulk hydrogen distribution, and D is the hydrogen diffusion coefficient, which is chosen as $1.8 \times 10^{-16}\ m^2/s$ in accordance with Ref. [82].

For simplicity, we assume the surface hydrogen concentration to be a constant value C_s for all the charging conditions and assume the initial bulk hydrogen concentration to be 0. The results are presented by the ratio of $C(x,t)$ to C_s. Therefore, after 12 h (43,200 s) of cathodic charging in the NI test, the hydrogen concentration in the sample can be expressed as follows.

$$\frac{C(x, 43{,}200s)}{C_s} = 1 - \mathrm{erf}\left(\frac{x}{\sqrt{4Dt}}\right) \tag{21}$$

In the case of hydrogen desorption during anodic discharging, the situation is more complex, owing to the non-constant initial hydrogen concentration beneath the sample surface, which does

not fulfill the boundary conditions of Eq. (19). Therefore, the non-steady state equation with a constant surface concentration and initial distribution $f(x)$ is used [83]:

$$C(x,t) = C_1 + (C_2 - C_1)\frac{x}{l} + \frac{2}{\pi}\sum_{1}^{\infty}\frac{C_2\cos n\pi - C_1}{n}\sin\frac{n\pi x}{l}\exp\left(-\frac{Dn^2\pi^2 t}{l^2}\right) + \frac{2}{l}\sum_{1}^{\infty}\sin\frac{n\pi x}{l}\exp\left(-\frac{Dn^2\pi^2 t}{l^2}\right)\int_0^l f(x')\sin\frac{n\pi x'}{l}dx' , \quad (22\text{-}1)$$

where

$$C = C_1, \quad x = 0, \quad t \geq 0, \quad (22\text{-}2)$$

$$C = C_2, \quad x = l, \quad t \geq 0, \quad (22\text{-}3)$$

$$C = \frac{C(x, 43{,}200s)}{C_s} = 1 - \mathrm{erf}\left(\frac{x}{\sqrt{4Dt}}\right), \quad 0 < x < l, \quad t = 0\,. \quad (22\text{-}4)$$

According to the foregoing models, the hydrogen concentration distribution in each condition is schematically shown in Fig. 8. After cathodic charging, a hydrogen concentration gradient clearly exists beneath the surface, as indicated by the red line. At the beginning of the discharging, we assume the boundary condition $C_1 = 0$ at the sample surface ($x = 0$) and $C_2 = 0$ at the depth of 10,000 nm, according to the cathodic curve highlighted by the red line in Fig. 8. In accordance with Eq. (22), the calculated hydrogen concentrations after 2 and 20 h (7,200 and 72,000 s) of anodic discharging are indicated by the black dashed line and black solid line in Fig. 8, respectively.

With reference to the constant surface hydrogen concentration C_s, the sample is deemed to be saturated with hydrogen at the depth of 60 ± 3 nm during electrochemical charging, which corresponds to the depth controlling the pop-in load. On the other hand, the hydrogen concentration at the depth of 835 nm, which significantly affects the hardness, reaches 83.1% C_s. It has been concluded that the dissolved hydrogen at the aforementioned two depths leads to the reduction of the pop-in load and the increase of the hardness. After 2 and 20 h of discharging, the dissolved hydrogen is almost imperceptible at the depth of 60 ± 3 nm. Therefore, pop-in loads obtained at two anodic discharging conditions are both controlled by a hydrogen-free region leading to the same pop-in load as in air. However, there is still 24.3% C_s hydrogen left at the depth of 835 nm after 2 h of discharging, as shown in Fig. 8. This means that 29.2% of the pre-

existing hydrogen (considering the original hydrogen concentration to be 83.1% C_s) in this depth range remains, resulting in a hardening effect and delayed hardness recovery. According to the data shown in Table 4, the concentration of the remaining hydrogen (29.2%) fits perfectly with the calculated percentage of hardness recovery after 2 h of anodic discharging. Moreover, the remaining hydrogen concentration decreases to 3.1% (2.57% C_s) after 20 h, in which case the hardness recovers to 91.6%. Therefore, it can be concluded that the fast recovery of the pop-in load and slow recovery of the hardness in the anodic condition are caused by the different amounts of remaining hydrogen at the corresponding affected depths.

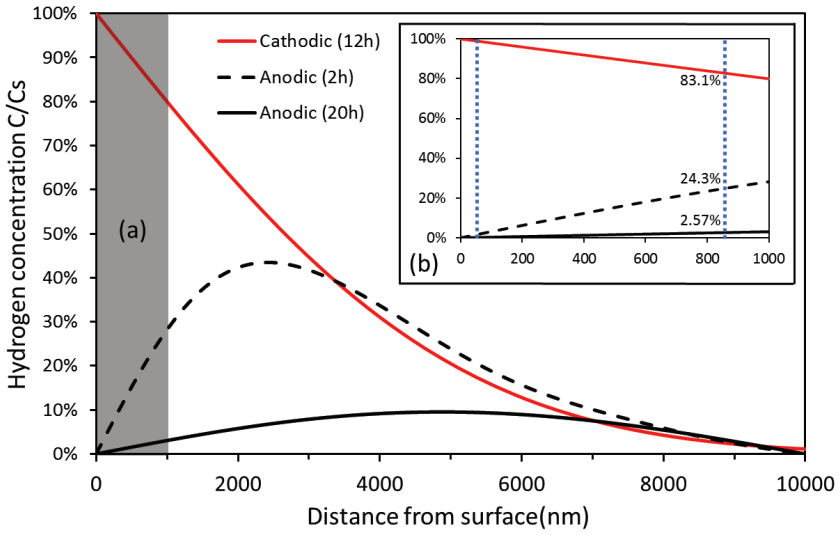

Fig. 8. (a) Hydrogen concentration profiles in different charging and discharging conditions. The red line represents the hydrogen concentration after cathodic charging. The black dashed line and black solid line indicate the hydrogen concentrations after 2 h and 20 h anodic discharging, respectively. (b) Enlarged area in (a) with two blue dotted lines indicating the depths of 63 and 835 nm beneath the sample surface.

Table 4.
Correlation between the hardness and the hydrogen concentration at the depth of 835 nm

	Remaining hydrogen	Discharged hydrogen	Hardness recovery (001)	Hardness recovery (101)	Hardness recovery (111)
Anodic 2 h	29.2%	70.8%	68.4%	65.3%	73.8%
Anodic 20 h	3.1%	96.9%	88.3%	91.6%	90.5%

5. Conclusion

The effect of hydrogen on the nanomechanical properties of Fe-22Mn-0.6C TWIP steel was investigated for three different grain orientations using the in-situ ECNI technique. Changes of the pop-in load and nanohardness were observed in the process of charging and discharging. The effects of hydrogen on the HDN, plastic zone size, and lattice friction were analyzed. The main conclusions are as follows.

1. The introduction of hydrogen reduced the pop-in load, which is attributed to the hydrogen-assisted HDN. The classical dislocation theory was used to calculate the required free energy for the HDN, and the results indicated that the dissolved hydrogen acted as defactant solute and substantially reduced the dislocation formation energy.

2. While single pop-in was observed in (101) and (111) grains, multiple pop-in behavior was detected in (001) grain. The second and subsequent pop-ins in (001) grain are attributed to the nucleation of deformation twins, which is consistent with the high Schmid-factor values for twin nucleation.

3. Under the exposure of hydrogen, enhanced hardening behavior was observed in the elastoplastic region, which increased the nanohardness. This phenomenon was related to the enhanced retarding stress on the dislocation motion caused by the reduced plastic zone size and the increased lattice friction between the dislocations and hydrogen.

4. During anodic discharging, the pop-in load exhibited fast recovery; however, the nanohardness showed a time-effect. Due to their different affecting depths, the discrepancy in the amount of residual hydrogen at corresponding depths explains the different recovery speeds.

Acknowledgements

The authors are grateful for the support provided by the Research Council of Norway through the HyF-Lex (244068/E30) project, the China scholarship council, and the promotion of scientific exchange by the German Research Foundation (DFG) in the framework of the Collaborative Research Center SFB 761 “Steel - ab initio.” The authors are also thankful to Prof. Jianying He of the Department of Structural Engineering (NTNU) for the helpful discussion.

Reference:

[1] O. Grassel, L. Kruger, G. Frommeyer, L.W. Meyer, High strength Fe-Mn-(Al, Si) TRIP/TWIP steels development-properties-application, Int. J. Plast. 16(10-11) (2000) 1391-1409.
[2] B.C. De Cooman, Y. Estrin, S.K. Kim, Twinning-induced plasticity (TWIP) steels, Acta Mater. 142 (2018) 283-362.
[3] O. Bouaziz, S. Allain, C.P. Scott, P. Cugy, D. Barbier, High manganese austenitic twinning induced plasticity steels: A review of the microstructure properties relationships, Curr. Opin. Solid State Mater. Sci. 15(4) (2011) 141-168.
[4] I. Gutierrez-Urrutia, D. Raabe, Dislocation and twin substructure evolution during strain hardening of an Fe-22 wt.% Mn-0.6 wt.% C TWIP steel observed by electron channeling contrast imaging, Acta Mater. 59(16) (2011) 6449-6462.
[5] D.R. Steinmetz, T. Japel, B. Wietbrock, P. Eisenlohr, I. Gutierrez-Urrutia, A. Saeed-Akbari, T. Hickel, F. Roters, D. Raabe, Revealing the strain-hardening behavior of twinning-induced plasticity steels: Theory, simulations, experiments, Acta Mater. 61(2) (2013) 494-510.
[6] M. Koyama, E. Akiyama, K. Tsuzaki, D. Raabe, Hydrogen-assisted failure in a twinning-induced plasticity steel studied under in situ hydrogen charging by electron channeling contrast imaging, Acta Mater. 61(12) (2013) 4607-4618.
[7] M. Koyama, E. Akiyama, K. Tsuzaki, Hydrogen embrittlement in a Fe-Mn-C ternary twinning-induced plasticity steel, Corros. Sci. 54 (2012) 1-4.
[8] N. Zan, H. Ding, X.F. Guo, Z.Y. Tang, W. Bleck, Effects of grain size on hydrogen embrittlement in a Fe-22Mn-0.6C TWIP steel, Int. J. Hydrog. Energy 40(33) (2015) 10687-10696.
[9] M. Nagumo, Fundamentals of hydrogen embrittlement, Springer, Singapore, 2016.
[10] A.R. Troiano, R. Gibala, R. Hehemann, Hydrogen embrittlement and stress corrosion cracking: a Troiano Festschrift, ASM International, Ohio, 1984.
[11] R.A. Oriani, P.H. Josephic, Equilibrium Aspects of Hydrogen-Induced Cracking of Steels, Acta Metall. 22(9) (1974) 1065-1074.
[12] Y.F. Wang, J.M. Gong, W.C. Jiang, A quantitative description on fracture toughness of steels in hydrogen gas, Int. J. Hydrog. Energy 38(28) (2013) 12503-12508.
[13] Z. Tarzimoghadam, M. Rohwerder, S.V. Merzlikin, A. Bashir, L. Yedra, S. Eswara, D. Ponge, D. Raabe, Multi-scale and spatially resolved hydrogen mapping in a Ni-Nb model alloy reveals the role of the δ phase in hydrogen embrittlement of alloy 718, Acta Mater. 109 (2016) 69-81.
[14] A. Laureys, T. Depover, R. Petrov, K. Verbeken, Influence of sample geometry and microstructure on the hydrogen induced cracking characteristics under uniaxial load, Mater. Sci. Eng. A 690 (2017) 88-95.
[15] D. Shih, I. Robertson, H. Birnbaum, Hydrogen embrittlement of α titanium: in situ TEM studies, Acta Metall. 36(1) (1988) 111-124.
[16] M.L. Martin, P. Sofronis, I.M. Robertson, T. Awane, Y. Murakami, A microstructural based understanding of hydrogen-enhanced fatigue of stainless steels, Int. J. Fatigue 57 (2013) 28-36.
[17] I.M. Robertson, P. Sofronis, A. Nagao, M.L. Martin, S. Wang, D.W. Gross, K.E. Nygren, Hydrogen Embrittlement Understood, Metall. Mater. Trans. A 46a(6) (2015) 2323-2341.
[18] D.F. Teter, I.M. Robertson, H.K. Birnbaum, The effects of hydrogen on the deformation and fracture of beta-titanium, Acta Mater. 49(20) (2001) 4313-4323.
[19] G.M. Bond, I.M. Robertson, H.K. Birnbaum, Effects of Hydrogen on Deformation and Fracture Processes in High-Purity Aluminum, Acta Metall. 36(8) (1988) 2193-2197.

[20] J.P. Chateau, D. Delafosse, T. Magnin, Numerical simulations of hydrogen-dislocation interactions in fcc stainless steels. Part II: hydrogen effects on crack tip plasticity at a stress corrosion crack, Acta Mater. 50(6) (2002) 1523-1538.
[21] H.K. Birnbaum, P. Sofronis, Hydrogen-enhanced localized plasticity—a mechanism for hydrogen-related fracture, Materials Science and Engineering: A 176(1) (1994) 191-202.
[22] M.L. Martin, J.A. Fenske, G.S. Liu, P. Sofronis, I.M. Robertson, On the formation and nature of quasi-cleavage fracture surfaces in hydrogen embrittled steels, Acta Mater. 59(4) (2011) 1601-1606.
[23] T. Neeraj, R. Srinivasan, J. Li, Hydrogen embrittlement of ferritic steels: Observations on deformation microstructure, nanoscale dimples and failure by nanovoiding, Acta Mater. 60(13-14) (2012) 5160-5171.
[24] W.A. Mcinteer, A.W. Thompson, I.M. Bernstein, The Effect of Hydrogen on the Slip Character of Nickel, Acta Metall. 28(7) (1980) 887-894.
[25] E. Lunarska, V. Novak, N. Zarubova, S. Kadeckova, Effect of Electrolytic Hydrogen Charging on Flow-Stress and Slip Line Pattern in Iron Single-Crystals, Scr. Metall. Mater. 17(6) (1983) 705-710.
[26] G. Lu, Q. Zhang, N. Kioussis, E. Kaxiras, Hydrogen-enhanced local plasticity in aluminum: An ab initio study, Phys. Rev. Lett. 87(9) (2001) art. no.-095501.
[27] R. Kirchheim, Reducing grain boundary, dislocation line and vacancy formation energies by solute segregation. I. Theoretical background, Acta Mater. 55(15) (2007) 5129-5138.
[28] R. Kirchheim, Reducing grain boundary, dislocation line and vacancy formation energies by solute segregation II. Experimental evidence and consequences, Acta Mater. 55(15) (2007) 5139-5148.
[29] R. Kirchheim, Revisiting hydrogen embrittlement models and hydrogen-induced homogeneous nucleation of dislocations, Scr. Mater. 62(2) (2010) 67-70.
[30] C. Verpoort, D.J. Duquette, N.S. Stoloff, A. Neu, The Influence of Plastic-Deformation on the Hydrogen Embrittlement of Nickel, Mater. Sci. Eng. 64(1) (1984) 135-145.
[31] D.P. Abraham, C.J. Altstetter, The Effect of Hydrogen on the Yield and Flow Stress of an Austenitic Stainless Steel, Metall. Mater. Trans. A 26(11) (1995) 2849-2858.
[32] M. Itakura, H. Kaburaki, M. Yamaguchi, T. Okita, The effect of hydrogen atoms on the screw dislocation mobility in bcc iron: A first-principles study, Acta Mater. 61(18) (2013) 6857-6867.
[33] T. Depover, E. Wallaert, K. Verbeken, On the synergy of diffusible hydrogen content and hydrogen diffusivity in the mechanical degradation of laboratory cast Fe-C alloys, Mater. Sci. Eng. A 664 (2016) 195-205.
[34] Y. Tobe, W.R. Tyson, Effect of Hydrogen on Yield of Iron, Scr. Metall. Mater. 11(10) (1977) 849-852.
[35] W.B. Xie, X.Y. Liu, W.X. Chen, H. Zhang, Hydrogen hardening effect in heavily deformed single crystal alpha-Fe, Comp. Mater. Sci. 50(12) (2011) 3397-3402.
[36] J. Song, W.A. Curtin, A nanoscale mechanism of hydrogen embrittlement in metals, Acta Mater. 59(4) (2011) 1557-1569.
[37] J. Song, W.A. Curtin, Mechanisms of hydrogen-enhanced localized plasticity: An atomistic study using alpha-Fe as a model system, Acta Mater. 68 (2014) 61-69.
[38] S.P. Lynch, Environmentally Assisted Cracking: Overview of Evidence for an Adsorption-Induced Localized-Slip Process, Acta Metall. 36(10) (1988) 2639-2661.
[39] S. Lynch, Hydrogen embrittlement phenomena and mechanisms, Corros. Rev. 30(3-4) (2012) 105-123.

[40] I.M. Robertson, The effect of hydrogen on dislocation dynamics, Eng. Fract. Mech. 68(6) (2001) 671-692.
[41] A. Barnoush, H. Vehoff, Recent developments in the study of hydrogen embrittlement: Hydrogen effect on dislocation nucleation, Acta Mater. 58(16) (2010) 5274-5285.
[42] O. Barrera, D. Bombac, Y. Chen, T.D. Daff, E. Galindo-Nava, P. Gong, D. Haley, R. Horton, I. Katzarov, J.R. Kermode, C. Liverani, M. Stopher, F. Sweeney, Understanding and mitigating hydrogen embrittlement of steels: a review of experimental, modelling and design progress from atomistic to continuum, J. Mater. Sci. 53(9) (2018) 6251-6290.
[43] I.J. Park, K.H. Jeong, J.G. Jung, C.S. Lee, Y.K. Lee, The mechanism of enhanced resistance to the hydrogen delayed fracture in Al-added Fe-18Mn-0.6C twinning-induced plasticity steels, Int. J. Hydrog. Energy 37(12) (2012) 9925-9932.
[44] I.J. Park, S.Y. Jo, M. Kang, S.M. Lee, Y.K. Lee, The effect of Ti precipitates on hydrogen embrittlement of Fe-18Mn-0.6C-2Al-xTi twinning-induced plasticity steel, Corros. Sci. 89 (2014) 38-45.
[45] T. Dieudonne, L. Marchetti, M. Wery, J. Chene, C. Allely, P. Cugy, C.P. Scott, Role of copper and aluminum additions on the hydrogen embrittlement susceptibility of austenitic Fe-Mn-C TWIP steels, Corros. Sci. 82 (2014) 218-226.
[46] I.J. Park, S.M. Lee, H.H. Jeon, Y.K. Lee, The advantage of grain refinement in the hydrogen embrittlement of Fe-18Mn-0.6C twinning-induced plasticity steel, Corros. Sci. 93 (2015) 63-69.
[47] B. Bal, M. Koyama, G. Gerstein, H.J. Maier, K. Tsuzaki, Effect of strain rate on hydrogen embrittlement susceptibility of twinning-induced plasticity steel pre-charged with high-pressure hydrogen gas, Int. J. Hydrog. Energy 41(34) (2016) 15362-15372.
[48] A. Barnoush, H. Vehoff, Electrochemical nanoindentation: A new approach to probe hydrogen/deformation interaction, Scr. Mater. 55(2) (2006) 195-198.
[49] A. Barnoush, Correlation between dislocation density and nanomechanical response during nanoindentation, Acta Mater. 60(3) (2012) 1268-1277.
[50] N. Kheradmand, R. Johnsen, J.S. Olsen, A. Barnoush, Effect of hydrogen on the hardness of different phases in super duplex stainless steel, Int. J. Hydrog. Energy 41(1) (2016) 704-712.
[51] M. Zamanzade, H. Vehoff, A. Barnoush, Effect of chromium on elastic and plastic deformation of Fe3Al intermetallics, Intermetallics 41 (2013) 28-34.
[52] A. Bamoush, N. Kheradmand, T. Hajilou, Correlation between the hydrogen chemical potential and pop-in load during in situ electrochemical nanoindentation, Scr. Mater. 108 (2015) 76-79.
[53] M. Kappes, G.S. Frankel, R. Thodla, M. Mueller, N. Sridhar, R.M. Carranza, Hydrogen Permeation and Corrosion Fatigue Crack Growth Rates of X65 Pipeline Steel Exposed to Acid Brines Containing Thiosulfate or Hydrogen Sulfide, Corrosion 68(11) (2012).
[54] I. Gutierrez-Urrutia, S. Zaefferer, D. Raabe, Electron channeling contrast imaging of twins and dislocations in twinning-induced plasticity steels under controlled diffraction conditions in a scanning electron microscope, Scr. Mater. 61(7) (2009) 737-740.
[55] R.D.K. Misra, Z. Zhang, Z. Jia, P.K.C.V. Surya, M.C. Somani, L.P. Karjalainen, Nanomechanical insights into the deformation behavior of austenitic alloys with different stacking fault energies and austenitic stability, Mater. Sci. Eng. A 528(22-23) (2011) 6958-6963.
[56] W.C. Oliver, G.M. Pharr, Measurement of hardness and elastic modulus by instrumented indentation: Advances in understanding and refinements to methodology, J. Mater. Res. 19(1) (2004) 3-20.

[57] J.L. Zhang, S. Zaefferer, D. Raabe, A study on the geometry of dislocation patterns in the surrounding of nanoindents in a TWIP steel using electron channeling contrast imaging and discrete dislocation dynamics simulations, Mater. Sci. Eng. A 636 (2015) 231-242.
[58] K. Durst, B. Backes, M. Goken, Indentation size effect in metallic materials: Correcting for the size of the plastic zone, Scr. Mater. 52(11) (2005) 1093-1097.
[59] W.S. Choi, B.C. De Cooman, S. Sandlobes, D. Raabe, Size and orientation effects in partial dislocation-mediated deformation of twinning-induced plasticity steel micro-pillars, Acta Mater. 98 (2015) 391-404.
[60] K.L. Johnson, Contact Mechanics, Cambridge University Press, Cambridge, 1987.
[61] P.M. Anderson, J.P. Hirth, J. Lothe, Theory of Dislocations, 3rd ed., Cambridge University Press, Cambridge, 2017.
[62] A. Barnoush, M. Zamanzade, Effect of substitutional solid solution on dislocation nucleation in Fe_3Al intermetallic alloys, Philos. Mag. 92(25-27) (2012) 3257-3268.
[63] C. Begau, A. Hartmaier, E.P. George, G.M. Pharr, Atomistic processes of dislocation generation and plastic deformation during nanoindentation, Acta Mater. 59(3) (2011) 934-942.
[64] A. Barnoush, H. Vehoff, Hydrogen embrittlement of aluminum in aqueous environments examined by in situ electrochemical nanoindentation, Scr. Mater. 58(9) (2008) 747-750.
[65] M. Zamanzade, H. Vehoff, A. Barnoush, Cr effect on hydrogen embrittlement of Fe3Al-based iron aluminide intermetallics: Surface or bulk effect, Acta Mater. 69 (2014) 210-223.
[66] M.Q. Chandler, M.F. Horstemeyer, M.I. Baskes, P.M. Gullett, G.J. Wagner, B. Jelinek, Hydrogen effects on nanovoid nucleation in face-centered cubic single-crystals, Acta Mater. 56(1) (2008) 95-104.
[67] P.J. Ferreira, I.M. Robertson, H.K. Birnbaum, Influence of hydrogen on the stacking-fault energy of an austenitic stainless steel, Mater. Sci. Forum 207-209 (1996) 93-96.
[68] W. Zhang, Y. Gao, Y. Xia, H. Bei, Indentation Schmid factor and incipient plasticity by nanoindentation pop-in tests in hexagonal close-packed single crystals, Acta Mater. 134 (2017) 53-65.
[69] S. Kang, Y.S. Jung, B.G. Yoo, J.I. Jang, Y.K. Lee, Orientation-dependent indentation modulus and yielding in a high Mn twinning-induced plasticity steel, Mater. Sci. Eng. A 532 (2012) 500-504.
[70] I. Karaman, H. Sehitoglu, K. Gall, Y.I. Chumlyakov, H.J. Maier, Deformation of single crystal Hadfield steel by twinning and slip, Acta Mater. 48(6) (2000) 1345-1359.
[71] S. Mahajan, G.Y. Chin, Formation of Deformation Twins in Fcc Crystals, Acta Metall. 21(10) (1973) 1353-1363.
[72] I. Gutierrez-Urrutia, S. Zaefferer, D. Raabe, The effect of grain size and grain orientation on deformation twinning in a Fe-22 wt.% Mn-0.6 wt.% C TWIP steel, Mater. Sci. Eng. A 527(15) (2010) 3552-3560.
[73] K. Durst, B. Backes, O. Franke, M. Goken, Indentation size effect in metallic materials: Modeling strength from pop-in to macroscopic hardness using geometrically necessary dislocations, Acta Mater. 54(9) (2006) 2547-2555.
[74] W.D. Nix, H.J. Gao, Indentation size effects in crystalline materials: A law for strain gradient plasticity, J. Mech. Phys. Solids 46(3) (1998) 411-425.
[75] A. Barnoush, M. Asgari, R. Johnsen, Resolving the hydrogen effect on dislocation nucleation and mobility by electrochemical nanoindentation, Scr. Mater. 66(6) (2012) 414-417.

[76] T. Zhu, J. Li, K.J. Van Vliet, S. Ogata, S. Yip, S. Suresh, Predictive modeling of nanoindentation-induced homogeneous dislocation nucleation in copper, J. Mech. Phys. Solids 52(3) (2004) 691-724.
[77] M.C. Fivel, C.F. Robertson, G.R. Canova, L. Boulanger, Three-dimensional modeling of indent-induced plastic zone at a mesoscale, Acta Mater. 46(17) (1998) 6183-6194.
[78] D. Kramer, H. Huang, M. Kriese, J. Robach, J. Nelson, A. Wright, D. Bahr, W.W. Gerberich, Yield strength predictions from the plastic zone around nanocontacts, Acta Mater. 47(1) (1998) 333-343.
[79] B.R. Lawn, A.G. Evans, D.B. Marshall, Elastic/Plastic Indentation Damage in Ceramics: The Median/Radial Crack System, J. Am. Ceram. Soc. 63(9-10) (1980) 574-581.
[80] J. Chen, S.J. Bull, On the relationship between plastic zone radius and maximum depth during nanoindentation, Surf. Coat. Technol. 201(7) (2006) 4289-4293.
[81] P.J. Burnett, D.S. Rickerby, The Mechanical Properties of Wear-Resistant Coatings I: Modeling of Hardness Behavior, Thin Solid Films 148(1) (1987) 41-50.
[82] V. Olden, C. Thaulow, R. Johnsen, Modelling of hydrogen diffusion and hydrogen induced cracking in supermartensitic and duplex stainless steels, Mater. Des. 29(10) (2008) 1934-1948.
[83] J. Crank, The Mathematics of Diffusion, 2nd ed., Oxford University Press, London, 1975.

Paper III

In-situ observation of martensitic transformation in an interstitial metastable high-entropy alloy during cathodic hydrogen charging

Dong Wang, Xu Lu, Di Wan, Zhiming Li, Afrooz Barnoush

Scr. Mater. 173 (2019) 56-60

In-situ observation of martensitic transformation in an interstitial metastable high-entropy alloy during cathodic hydrogen charging

Dong Wang, Xu Lu, Di Wan, Zhiming Li, Afrooz Barnoush

Abstract: We show for the first time that a critical amount of dissolved hydrogen can induce a phase transformation from γ-austenite to ε-martensite in an interstitial metastable high-entropy alloy. This is demonstrated by in-situ hydrogen charging in combination with nanoindentation and scanning probe microscopy, plus further electron channeling contrast imaging, X-ray diffraction, and transmission Kikuchi diffraction techniques. The transformed martensites appear as bands on the surface along γ-{111} habit planes, leading to an irreversible increase of hardness. The hydrogen-induced internal stress together with the intrinsic hydrogen effects are proposed to be responsible for the martensitic transformation upon hydrogen charging.

Keywords: Hydrogen; High-entropy alloy; Martensitic transformation; In-situ electrochemical nanoindentation; Transmission Kikuchi diffraction

High-entropy alloys (HEAs) are a new class of alloys containing multiple principal elements, which provide a high mixing entropy and a massive solid solution state [1, 2]. Over the past decade, HEAs have attracted considerable attention owing to their excellent properties such as excellent combination of strength and ductility, outstanding fracture toughness, and good resistance to wear at both elevated and cryogenic temperatures [1-4]. These outstanding properties make HEAs as promising materials for applications in nuclear construction, liquid gas storage, transportation, and so forth [5]. However, a hydrogen-rich service environment can be deduced from the aforementioned applications, giving a high possibility of catastrophic and unpredictable failure known as hydrogen embrittlement. Up to now, most of the hydrogen embrittlement studies on HEAs are performed on the equiatomic CoCrFeMnNi alloy with the conclusion that this alloy has good resistance to hydrogen embrittlement at relatively low hydrogen concentration, while it still exhibits embrittlement phenomena when charged with high hydrogen content [6-8]. In addition, the hydrogen effect on a non-equiatomic dual-phase FeMnCoCr HEA was investigated by Ichii et al. [9] via performing macroscopic tensile tests on pre-charged samples. The results showed

reduction on both elongation and strength with obvious ε-martensite transformation, which was a combined effect from both hydrogen and deformation.

Recently, the interstitial metastable non-equiatomic HEAs have been developed exhibiting enhanced strength and strain hardening rate while maintaining good ductility compared to the equiatomic HEAs and the non-equiatomic HEAs without interstitial alloying [4, 10, 11]. This is due to the fact that this alloy design strategy can not only activate interstitial solid solution strengthening, but also tune phase stability and stacking fault energy (SFE) to achieve joint activation of transformation-induced plasticity (TRIP) and twinning-induced plasticity (TWIP) effects during deformation [12]. In such type of interstitial metastable HEAs, the TRIP effect suggests a deformation-induced phase transformation from face-centered cubic (FCC) γ phase to hexagonal close packed (HCP) ε phase [3, 11, 13]. To date, neither a hydrogen-related study at microscale nor the effect of hydrogen alone on the microstructure and nanomechanical properties of interstitial metastable HEAs has been discussed. In this study, we performed in-situ electrochemical hydrogen charging in combination with scanning probe microscopy (SPM) and nanoindentation. By this method combining with subsequent advanced characterization techniques, the effect of hydrogen alone on the microstructure and nanomechanical properties can be examined and understood.

The nominal chemical composition of the studied HEA is Fe-30Mn-10Co-10Cr-0.5C (at. %). The alloy ingot was cast in a vacuum induction furnace, hot-rolled at 900 °C, homogenized at 1200 °C for 2 h, and followed by water quenching. The alloy sample was further machined into discs with a thickness of 1.2 mm and a diameter of 12 mm. The disc samples were sequentially ground and polished till 1 μm diamond paste followed by electropolishing in a methanol/H_2SO_4 solution at 25 V for 80 s. After the surface preparation, a high-resolution scanning electron microscope (SEM, Quanta 650 FEG, Thermo Fisher Scientific Inc.) with a backscattered electron (BSE) detector as well as the electron backscatter diffraction (EBSD) techniques was used to study the original microstructure. After that, the sample was installed into an electrochemical cell consisting of a platinum counter electrode and a Hg/$HgSO_4$ reference electrode. Hereafter, all potentials in this study are reported versus this reference electrode. The electrochemical hydrogen charging was performed in a glycerol-based electrolyte, which consisted of 1.4 mol/L borax in glycerol and diluted with 20% distilled water to ensure the conductivity. In addition, 0.002 M $Na_2S_2O_3$ was

added to promote the hydrogen absorption and prevent the hydrogen recombination [14]. This electrolyte has been proven to be reliable in keeping the sample surface from corrosion or oxidation due to its extremely low solubility and diffusivity of oxygen [15, 16]. The setup was further installed into a Hysitron Tribo-indenter TI950 equipped with a specially designed long-shaft Berkovich diamond tip, which was used for both SPM and nanoindentation test. In this study, the sample was firstly tested in air as the reference condition, followed by the same tests with in-situ hydrogen charging at -1400 and -1800 mV (the current densities were 0.12 and 0.85 mA/cm^2, respectively). After each cathodic charging, an anodic discharging at 0 mV was performed to check the reversibility after the desorption of hydrogen. Both cathodic charging and anodic discharging processes were applied at room temperature for more than 1.5 h till a stable hardness was reached. The SPM images were scanned on a same area and the hardness values were measured on the same grain at every 15 min. After the in-situ test, electron channeling contrast imaging (ECCI) was applied to characterize the deformed surface microstructure with 30 kV acceleration voltage and ~6.5 mm working distance; EBSD and grazing incidence X-ray diffraction (GIXRD, D8 DaVinci with LynxEye™ Superspeed detector) were performed to determine the phase distribution. The GIXRD was operated by using Cu Kα radiation (40 kV, 40 mA) at 0.75° incident angle at a step size of 0.02° and a counting time of 4.8 s per step; Transmission Kikuchi diffraction (TKD) was used to correlate the hydrogen effect on phase transformation with the dissolved hydrogen concentration determined by thermal desorption spectroscopy (TDS) test. The TDS test was carried out by Bruker G4 PHOENIX with a mass spectrometer detector from 25 °C to 700 °C at a heating rate of 25 °C/min.

Fig. 1 shows the representative SPM images and the corresponding root-mean-square roughness R_q at different in-situ polarization conditions. The topography of sample surface in air condition before hydrogen charging is shown in Fig. 1a for reference. The original sample has a smooth surface with a R_q value of 0.056 nm as shown in Fig. 1g. The exact same position was continuously scanned in the following polarization conditions. Fig. 1b was captured after 2 h cathodic hydrogen charging at -1400 mV followed by 1.5 h anodic hydrogen discharging at 0 mV, and no noticeable change can be detected. Moreover, the R_q value was kept constant through the first sequence of hydrogen ingression and egression. However, the evolution of topography was detected when switched to -1800 mV cathodic polarization. As shown in Fig. 1c-e, the straight bands appeared

after 1 h charging at -1800 mV, and these bands accumulated and became more noticeable by increasing the charging time. Fig. 1g shows that the roughness increased 32 times from 0.056 nm to 1.8 nm after 3.5 h charging at -1800 mV. After -1800 mV cathodic charging, the second anodic discharging was applied for a long time (13 h), and no irreversible phenomena were observed on both the SPM image and R_q value. Worthy of note, the accuracy of R_q values calculated from SPM images can be affected by factors such as tip bluntness, scan rate, and contact condition especially for in-situ condition and might not precisely reflect the actual surface roughness. Nevertheless, the change in the R_q values can be used as an indicator to reflect the trend of the actual surface roughness and martensitic transformation during in-situ hydrogen charging.

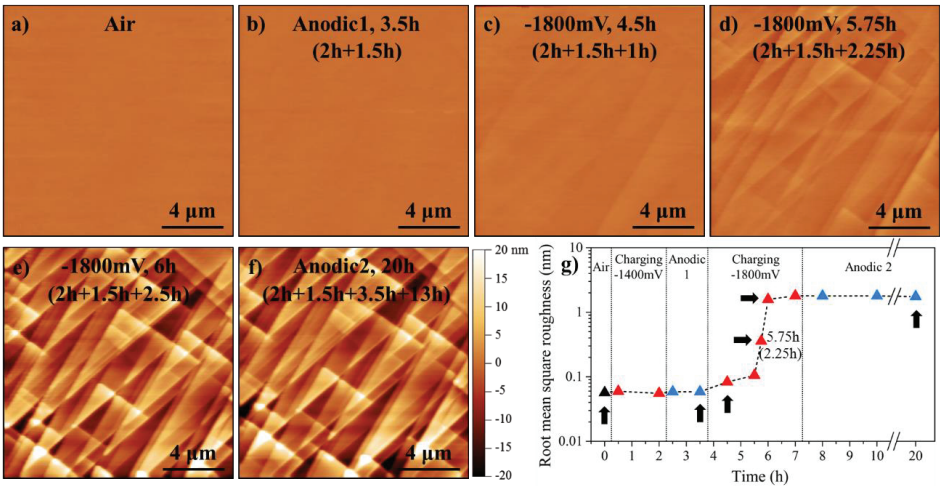

Fig. 1. (a-f) The representative SPM images during in-situ hydrogen charging/discharging under different conditions. The times marked on the top are the total polarization time and the times marked in the parenthesis below are the individual cathodic charging and anodic discharging times. g) The evolution of root-mean-square roughness R_q (nm) during in-situ hydrogen charging. The black arrows indicate the conditions shown in SPM images.

The nanoindentation test was performed on the same grain after each SPM scan, and the representative load-displacement curves are shown in the supplementary Fig.1. The hardness values were further calculated by using the Oliver-Pharr method [17]. As shown in Fig. 2, the original hardness in air was 3.63 GPa, and it accumulatively increased to a stable value of 4.07

GPa after 2 h cathodic charging at -1400 mV and then recovered to a similar value as in air condition after 1.5 h anodic discharging. By applying a higher charging potential at -1800 mV, a continuously increased hardness value was detected till a stable value was reached after 3.5 h charging, which showed a more significant hardness increment to 7.75 GPa. Moreover, a sudden hardness increment was observed in this cathodic charging condition after 2.25 h, which matches the apparent topography change (Fig. 1d). However, in comparison with the fully recovered hardness in the first anodic process, the hardness in the second anodic discharging condition showed only partial recovery (38.3%).

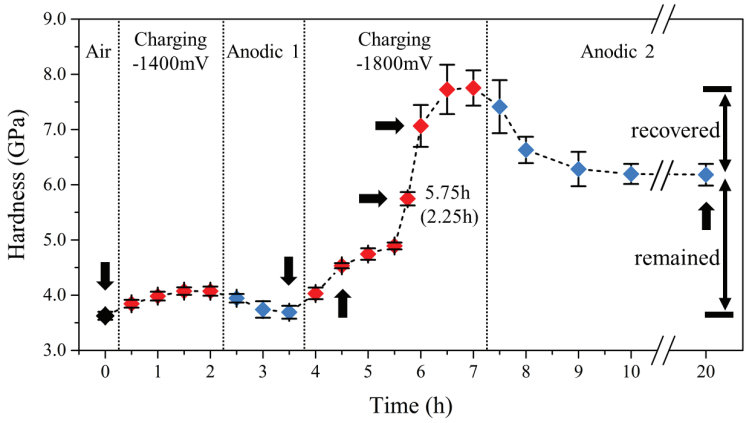

Fig. 2. The hardness values of the studied alloy under sequential polarization conditions. The black arrows indicate the conditions corresponding to the SPM images shown Fig. 1.

The reversible hardness increment during the first sequence of hydrogen ingression and egression was caused by the enhanced retarding stress on dislocation motion due to the increased lattice friction between dislocations and dissolved hydrogen [18]. The remained hardness increment as well as the topography change in the second sequence of charging and discharging was proposed due to hydrogen-induced phase transformation from γ-austenite to ε-martensite, which generally shows a very high hardness value [19]. In order to validate this assumption, further advanced characterization techniques were applied. Fig. 3a-3d show the ECC images of sample surface before (Fig. 3a) and after (Fig. 3b-3d) the in-situ test. The sample surface before charging contains uniformly distributed dislocations at a relatively low density. After the whole charging/discharging process, the deformation bands along three different directions are clearly visible. The orientations

of these deformation bands, marked as black lines, are parallel to {111} slip traces indicated by red lines. Fig. 3d shows the ECC image at a higher magnification: the thin bands are stacking faults (SFs) and the thick bands are martensite plates forming through the overlapping of SFs [3]. The martensitic transformation can also be confirmed by GIXRD and EBSD analysis. Fig. 3e and 3f show the phase maps with the corresponding GIXRD spectra before and after hydrogen charging, respectively. It shows a pure γ-austenite phase in the original sample, and the parallel pattern consisting of ε-martensite lamellae can be observed within the γ grains after the whole in-situ hydrogen charging/discharging process. The γ-{111} and ε-{0001} pole figures constructed from the marked grains (1 to 4 in Fig. 3f) are shown as Fig. 3g and 3h, respectively. The poles are colored uniquely and encircled by unique shapes for each γ grain. It can be seen that the {0001} poles of ε phase appeared roughly at the same place as the {111} poles of γ phase for each indexed grain. This suggests a $\{111\}_\gamma \parallel \{0001\}_\varepsilon$ orientation relationship, which is in good agreement with the habit planes of ε-martensite transformation [20, 21]. It is worth noting that in contrast to the transformed α' and ε phases in austenitic stainless steels [22, 23], the ε phase is the only detected product phase in the current alloy. This might be due to a relatively high stability of the ε phase in the studied material [24]. This agrees with the phase transformation investigations of this material after cold rolling and tensile testing [11, 25].

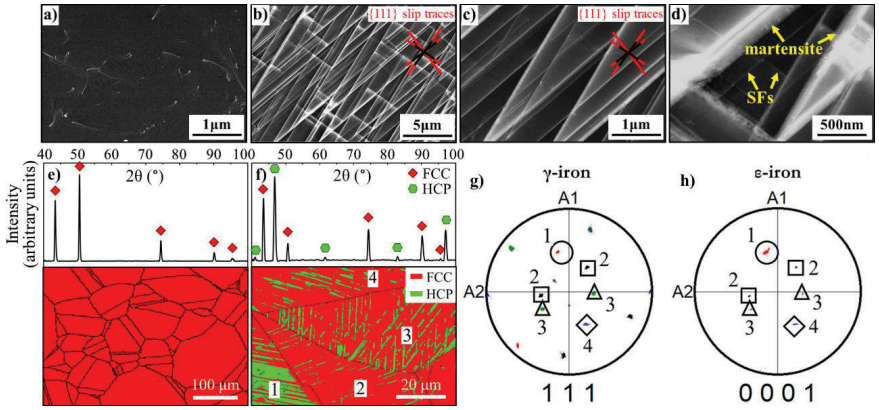

Fig. 3. The ECC images of the sample surface before (a) and after (b-d) in-situ polarization test. (c) and (d) are the magnified areas of (b). The phase maps with the corresponding GIXRD spectra before (e) and after (f) hydrogen charging. The γ-{111} (g) and ε-{0001} (h) pole figures of the marked grains in (f).

It has been claimed within the framework of the defactant theory that the dissolved hydrogen can act as defactants and reduce the SFE [26-28]. A reduced SFE can facilitate the formation of SFs, which can serve as the nucleation sites for martensitic transformation [29]. According to the Kajiwara model [30], when stress is applied, a dislocation loop with partial Burgers vector is generated two atomic layers away from the pre-existing SF and a four-atomic-layer nano-sized ε-martensite is therefore produced. This thin ε-martensite grows thicker by consecutive formation of such dislocation loops at every second layer. The further growth of the martensite plates is thus presented as surface reliefs referring to the topographical changes. In this study, the charged hydrogen facilitated the formation of SFs on {111} closed packed planes, which acted as the nucleation sites for martensitic transformation. This hypothesis matches perfectly with the ECCI and EBSD results in Fig. 3 showing that the martensite formation is along {111} habit planes. Moreover, it has been proven by both experiments [31, 32] and simulations [33, 34] that hydrogen charging can lead to the formation of superabundant vacancies. The hydrogen-induced vacancies can further reduce the phase stability, resulting in martensitic phase transformation in interstitial-substitutional alloys [35]. Therefore, the hydrogen-induced vacancies might also facilitate the observed phase transformation in the current study. However, not only the intrinsic hydrogen effect can promote the martensitic transformation, the hydrogen-induced internal stress also facilitates the phase transformation. During charging at -1800 mV, a high hydrogen concentration in the surface area is reached, which causes lattice expansion and results in high compressive internal stress [36]. This high internal stress acts as the driving force for γ to ε transformation during the cathodic charging process in this study.

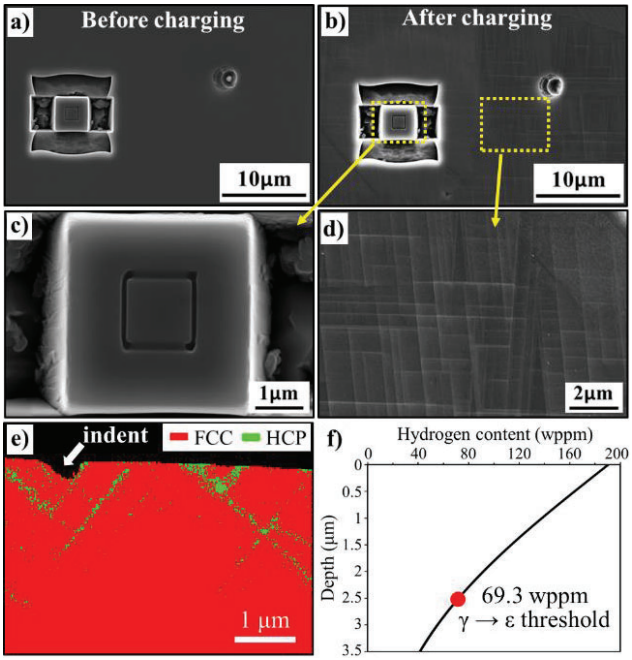

Fig. 4. The SEM images of the sample surface with a specially milled micro-pillar before (a) and after (b) hydrogen charging. The magnified images of micro-pillar surface (c) and sample matrix (d) after hydrogen charging. (e) The TKD phase map of surface area showing the depth of martensitic transformation. (f) Hydrogen concentration as a function of depth at the end of -1800 mV charging process.

In order to prove the necessary conditions of hydrogen-induced internal stress on the phase transformation, an isolated square-shaped micro-pillar with the size of 4×4×2 μm^3 was milled by focused ion beam (FIB, Helios Dual Beam, Thermo Fisher Scientific Inc., USA) as shown in Fig. 4a. The milling process was performed by a pre-designed one-step-pattern to avoid Ga ion-induced FIB damage. Without constraints surrounding the free-standing pillar, the internal stress induced by hydrogen charging can be easily released. By repeating the same hydrogen charging/discharging process, the pillar shows a smooth surface without any observable changes (Fig. 4c), while uniformly distributed martensitic bands are exhibited along three directions in the nearby matrix surface regions (Fig. 4d). This observation shows that a critical internal stress is the prerequisite for the martensitic transformation in this study. In order to determine the threshold of

hydrogen concentration for this critical internal stress, a TKD characterization was performed. The specimen for TKD was cut by using FIB from the tested sample surface (deposited with protective carbon layer) till a depth of 5 μm and then milled from both sides to a final thickness of approximately 100 nm. The TKD result in Fig. 4e clearly shows that the ε-martensite was transformed within a depth of approximately 2.5 μm. The hydrogen content was measured by TDS on one sample (diameter 11.55 mm, thickness 0.81 mm, weight 0.6358 g) charged with the same conditions till the end of -1800 mV polarization as well as on one uncharged sample (diameter 11.55 mm, thickness 0.92 mm, weight 0.7243 g). The hydrogen content of the uncharged sample was measured as zero, while 1.0814 wppm hydrogen was quantified on the charged sample. The measured hydrogen content contains both diffusible hydrogen and trapped hydrogen, which are not differentiated in the current study and are considered to contribute together to the phase transformation. The surface hydrogen concentration C_s during charging at -1800 mV can be estimated by [37]

$$C_s = \frac{\omega C_M}{4}\sqrt{\frac{\pi}{Dt}} \tag{1}$$

where ω is the sample thickness, C_M is the mean hydrogen concentration of the sample (1.0814 wppm), and D is the hydrogen diffusion coefficient chosen as 3.2×10^{-16} m^2/s [7]. The related hydrogen concentration $C(x,t)$ at distance x and time t was calculated by using the Fick's law based "semi-infinite" model [38]:

$$\frac{C(x,t)-C_0}{C_s-C_0} = 1-\mathrm{erf}\left(\frac{x}{\sqrt{4Dt}}\right) \tag{2}$$

where C_0 is the initial hydrogen concentration as zero. The concentration profile of hydrogen in the sample is shown in Fig. 4f. Based on the TDS and TKD results, the threshold of hydrogen concentration for ε-martensite transformation can be estimated as 69.3 wppm, which was caused by 3.5 h hydrogen charging at -1800 mV (0.85 mA/cm^2) at the depth of 2.5 μm. Note that both the hydrogen charging current density and the dissolved hydrogen content resulting in martensitic transformation in this study are much less than that has been applied in many other studies involving martensitic transformation in the pre-charged samples after tensile tests [9, 39]. The above results suggest that it is important to distinguish between the tensile deformation induced

martensite and the pre-charged hydrogen induced martensite in the future hydrogen embrittlement studies.

In summary, the influence of hydrogen alone on the phase transformation was investigated for the first time in an interstitial metastable HEA through in-situ hydrogen charging together with nanoindentation and SPM tests, plus further characterization by ECCI, EBSD, GIXRD and TKD techniques. The results show that cathodic hydrogen charging with a critical charging current density can lead to γ-austenite to ε-martensite transformation along the {111} habit planes. The transformed martensites appear as bands on the sample surface, leading to an irreversible increase of hardness. The hydrogen-induced internal stress together with the intrinsic hydrogen effect on SFE reduction and superabundant vacancies formation are proposed as the reasons for the martensitic transformation during hydrogen charging. Accordingly, it is necessary to consider these effects in future studies on hydrogen embrittlement and the design of hydrogen-tolerant alloys.

Acknowledgements

The Research Council of Norway is acknowledged for the support to the Norwegian Micro- and NanoFabrication Facility, NorFab, project number 245963/F50. The authors are grateful for the support provided by the Research Council of Norway through the HyF-Lex (244068/E30) project. The author (Dong Wang) would like to acknowledge the financial support from the China scholarship council.

Reference

[1] Y. Zhang, T.T. Zuo, Z. Tang, M.C. Gao, K.A. Dahmen, P.K. Liaw, Z.P. Lu, Prog. Mater. Sci. 61 (2014) 1-93.
[2] J.W. Yeh, S.K. Chen, J.Y. Gan, S.J. Lin, T.S. Chin, T.T. Shun, C.H. Tsau, S.Y. Chang, Metall. Mater. Trans. A 35a(8) (2004) 2533-2536.
[3] Z. Li, K.G. Pradeep, Y. Deng, D. Raabe, C.C. Tasan, Nature 534(7606) (2016) 227-30.
[4] Z.M. Li, C.C. Tasan, H. Springer, B. Gault, D. Raabe, Sci. Rep. 7 (2017) 40704.
[5] Y.F. Ye, Q. Wang, J. Lu, C.T. Liu, Y. Yang, Mater. Today 19(6) (2016) 349-362.
[6] H. Luo, Z. Li, D. Raabe, Sci. Rep. 7(1) (2017) 9892.
[7] Y. Zhao, D.-H. Lee, M.-Y. Seok, J.-A. Lee, M.P. Phaniraj, J.-Y. Suh, H.-Y. Ha, J.-Y. Kim, U. Ramamurty, J.-i. Jang, Scr. Mater. 135 (2017) 54-58.
[8] K.E. Nygren, K.M. Bertsch, S. Wang, H. Bei, A. Nagao, I.M. Robertson, Curr. Opin. Solid State Mater. Sci. 22(1) (2018) 1-7.
[9] K. Ichii, M. Koyama, C.C. Tasan, K. Tsuzaki, Scr. Mater. 150 (2018) 74-77.
[10] Z. Li, Acta Mater. 164 (2019) 400-412.
[11] M.M. Wang, Z.M. Li, D. Raabe, Acta Mater. 147 (2018) 236-246.
[12] Z.M. Li, D. Raabe, Jom 69(11) (2017) 2099-2106.
[13] M. Koyama, T. Eguchi, K. Ichii, C.C. Tasan, K. Tsuzaki, Procedia Struct. Inte. 13 (2018) 292-297.
[14] M. Kappes, G.S. Frankel, R. Thodla, M. Mueller, N. Sridhar, R.M. Carranza, Corrosion 68(11) (2012).
[15] X. Lu, Y. Ma, M. Zamanzade, Y. Deng, D. Wang, W. Bleck, W.W. Song, A. Barnoush, Int. J. Hydrog. Energy 44(36) (2019) 20545-20551.
[16] X. Lu, D. Wang, Z. Li, Y. Deng, A. Barnoush, Mater. Sci. Eng. A 762 (2019) 138114.
[17] W.C. Oliver, G.M. Pharr, J. Mater. Res. 19(1) (2004) 3-20.
[18] D. Wang, X. Lu, Y. Deng, X. Guo, A. Barnoush, Acta Mater. 166 (2019) 618-629.
[19] H. Zhang, Y.Z. He, Y. Pan, Scr. Mater. 69(4) (2013) 342-345.
[20] G. Stone, G. Thomas, Metall. Trans. 5(9) (1974) 2095-2102.
[21] Z.H. Guo, Y.H. Rong, S.P. Chen, T.Y. Hsu, Scr. Mater. 41(2) (1999) 153-158.
[22] A.P. Bentley, G.C. Smith, Metall. Mater. Trans. A 17(9) (1986) 1593-1600.
[23] X.-S. Yang, S. Sun, T.-Y. Zhang, Acta Mater. 95 (2015) 264-273.
[24] W.J. Lu, C.H. Liebscher, G. Dehm, D. Raabe, Z.M. Li, Adv. Mater. 30(44) (2018).
[25] J. Su, X.X. Wu, D. Raabe, Z.M. Li, Acta Mater. 167 (2019) 23-39.
[26] R. Kirchheim, Scr. Mater. 62(2) (2010) 67-70.
[27] M.Q. Chandler, M.F. Horstemeyer, M.I. Baskes, P.M. Gullett, G.J. Wagner, B. Jelinek, Acta Mater. 56(1) (2008) 95-104.
[28] P.J. Ferreira, I.M. Robertson, H.K. Birnbaum, Mater. Sci. Forum 207-209 (1996) 93-96.
[29] N. Bergeon, S. Kajiwara, T. Kikuchi, Acta Mater. 48(16) (2000) 4053-4064.
[30] S. Kajiwara, D.Z. Liu, T. Kikuchi, N. Shinya, J. Phys. IV 11(Pr8) (2001) 199-204.
[31] Y. Fukai, K. Mori, H. Shinomiya, J. Alloys Compd. 348(1-2) (2003) 105-109.
[32] Y. Fukai, Phys. Scr. T103 (2003) 11-14.
[33] K. Ohsawa, F. Nakamori, Y. Hatano, M. Yamaguchi, J. Nucl. Mater. 458 (2015) 187-197.
[34] A. Metsue, A. Oudriss, X. Feaugas, MRS Adv. 1(24) (2016) 1785-1790.
[35] V.N. Bugaev, V.G. Gavriljuk, Y.N. Petrov, A.V. Tarasenko, Int. J. Hydrog. Energy 22(2-3) (1997) 213-218.
[36] Q. Yang, L.J. Qiao, S. Chiovelli, J.L. Luo, Scr. Mater. 40(11) (1999) 1209-1214.

[37] A.E. Pontini, J.D. Hermida, Scr. Mater. 37(11) (1997) 1831-1837.
[38] V. Olden, C. Thaulow, R. Johnsen, Mater. Des. 29(10) (2008) 1934-1948.
[39] Y.S. Chun, J.S. Kim, K.T. Park, Y.K. Lee, C.S. Lee, Mater. Sci. Eng. A 533 (2012) 87-95.

Supplementary material for

In-situ observation of martensitic transformation in an interstitial metastable high-entropy alloy during cathodic hydrogen charging

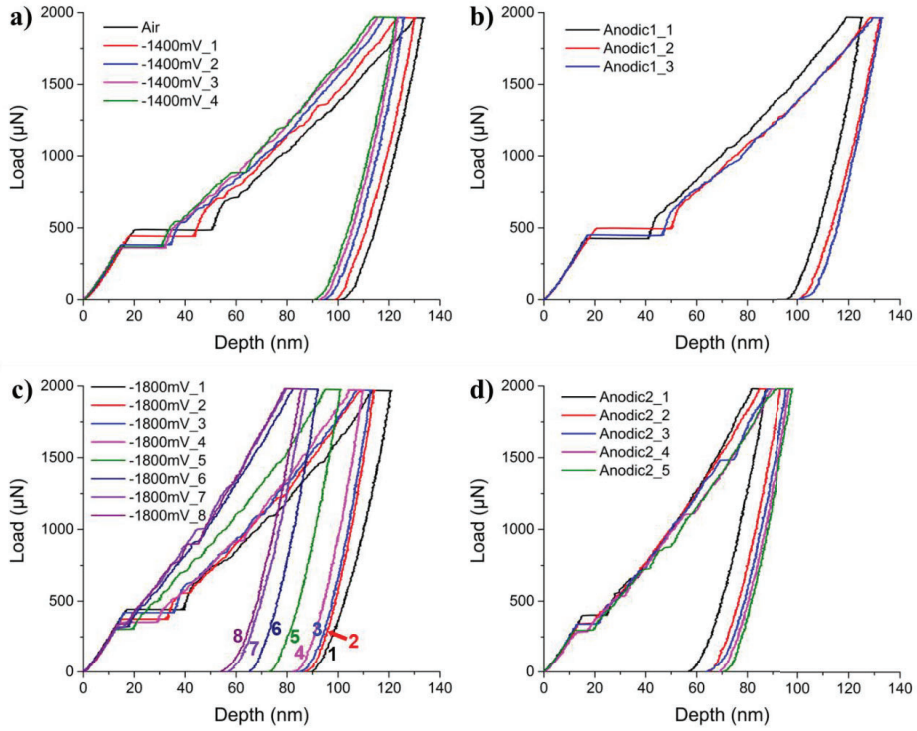

Supplementary Fig. 1. Representative load-displacement curves in (a) air and -1400 mV hydrogen charging, (b) first anodic discharging, (c) -1800 mV hydrogen charging, and (d) second anodic discharging. The numbers in the legends indicate the testing time sequence that corresponds to each measured hardness value shown in Fig. 2 in the paper.

Paper IV

Effect of hydrogen-induced surface steps on the nanomechanical behavior of a CoCrFeMnNi high-entropy alloy revealed by in-situ electrochemical nanoindentation

Dong Wang, Xu Lu, Yun Deng, Di Wan, Zhiming Li, Afrooz Barnoush

Intermetallics 114 (2019)

Effect of hydrogen-induced surface steps on the nanomechanical behavior of a CoCrFeMnNi high-entropy alloy revealed by in-situ electrochemical nanoindentation

Dong Wang, Xu Lu, Yun Deng, Di Wan, Zhiming Li, Afrooz Barnoush

Abstract: The effect of hydrogen on the nanomechanical properties of CoCrFeMnNi high-entropy alloy was investigated by in-situ electrochemical nanoindentation testing. The changes in surface morphology, elastic modulus, pop-in load, and hardness during hydrogen ingress and egress processes were systematically evaluated. The results show that hydrogen charging leads to the formation of irreversible slip lines accumulated as surface steps. Furthermore, the irreversible reduced pop-in load and elastic modulus, and reversible increased hardness are detected. In this paper, the mechanisms of hydrogen-induced surface steps together with their further influences on the nanomechanical properties are discussed in detail.

Keywords: In-situ electrochemical nanoindentation; High-entropy alloy; Hydrogen embrittlement; Hydrogen-induced surface steps; Electron channeling contrast imaging; Nanomechanics

1. Introduction

High-entropy alloys (HEAs) are substances that are comprised of five or more metallic elements with (near-) equal atomic ratio [1]. Since first introduced by Yeh et al. [2], HEAs have attracted considerable research attention because of their extraordinary mechanical properties such as the excellent combination of high strength and good ductility, high toughness, and good creep resistance [2-5]. All of these astonishing properties make HEAs a group of promising materials for turbine blades, nuclear constructions, liquid gas storage and transportation, and so forth [1, 6]. However, with the aforementioned potential applications, a hydrogen-rich service environment can lead to a high possibility of unexpected failure owing to hydrogen embrittlement, which is in accordance with the concept of hydrogen-induced degradation of metals with a transition from ductile to brittle failure [7, 8]. Therefore, the effects of hydrogen on the mechanical responses of HEAs should be investigated thoroughly prior to designing them for potential applications.

The mechanism of hydrogen embrittlement has been studied intensively but is still a controversial topic without a clear consensus. Different mechanisms have been proposed based on various experiments and observations, among which the hydrogen-enhanced decohesion (HEDE) [9, 10],

hydrogen-enhanced localized plasticity (HELP) [7, 11, 12], adsorption-induced dislocation emission (AIDE) [13, 14], and "Defactant" [15-17] are the most popular models. The HEDE mechanism, proposed by Troiano et al. [9], postulates that the bonding energy between atoms is reduced by the presence of hydrogen and thus there is an increased risk of decohesion. The HEDE mechanism has been widely used to explain the cleavage-like failure and intergranular fracture surface in high strength steels [18, 19]. The HELP mechanism postulates that the mobility of dislocations is increased by the dissolved hydrogen due to the shielding effect on the elastic stress field of dislocations, thus resulting in slip localization and denser dislocation pile-ups [7, 11, 20]. The HELP mechanism was directly proven by the in-situ transmission electron microscopy (TEM) technique [12], where the enhanced dislocation motion was directly observed when hydrogen gas was introduced around a thin specimen subjected to plastic deformation. However, contradictory results have also been reported showing a hydrogen-restricted dislocation mobility effect [21, 22]. The AIDE mechanism, proposed by Lynch [13, 14], concludes that hydrogen-assisted cracking occurs because of the adsorption of hydrogen at crack tips. Specifically, the adsorbed hydrogen facilitates the emission of dislocations from crack tips and therefore promotes the occurrence of coalescence of cracks with voids to lower strains. The Defactant model, based on thermodynamic calculations, suggests that the formation energy of defects (such as dislocations and stacking faults) is reduced by the presence of defactant solutes, such as hydrogen [15-17]. It is necessary to mention here that hydrogen embrittlement is a complex process that depends heavily on the metals and applied environment and no aforementioned mechanisms can explain the phenomena exclusively. Moreover, these mechanisms are not completely distinct but share some overlaps with each other [23].

Among the various HEAs systems, CoCrFeMnNi alloy with five elements in equiatomic concentrations is the most appealing one owing to the thermodynamically stable single face-centered cubic (FCC) phase, the outstanding mechanical properties that provide a good combination of strength and ductility at room temperature [1, 24], and the superior fracture resistance at low temperatures [25]. Recently, the susceptibility of CoCrFeMnNi to hydrogen embrittlement has been reported with interesting conclusions. Luo et al. [26] reported results from in-situ tensile tests on electrochemically charged samples and the findings demonstrated that the dissolved hydrogen at relatively low concentrations (8.01-33.25 wppm) increases both the strength and ductility rather than causing catastrophic failure. They proposed that the charged hydrogen

reduces the stacking fault energy and the phase stability. Therefore, the density of nano-twins is increased leading to an enhanced work hardening capability, and this thus enhances both the strength and ductility. Zhao et al. [27] charged the tensile test samples with 15 MPa gaseous hydrogen at 300°C for 72 h (76.5 wppm) and the results showed that the ductility reduction of the hydrogen-charged sample is only 5%. The fracture surfaces of charged and uncharged samples are similar, and both consist of dimples indicating ductile fractures. Also, Nygren et al. [28] performed tensile tests on samples charged by 120 MPa gaseous hydrogen at 200°C for 160 h with a much higher concentration (146.9 wppm) and the results showed that the CoCrFeMnNi alloy exhibites a significant reduction in ductility with the fracture mode changing from transgranular ductile failure to intergranular brittle failure. These macroscopic tensile tests on pre-charged samples provided useful information on the hydrogen embrittlement phenomena showing the changes in mechanical properties and fracture behavior with adequate dissolved hydrogen. However, due to the fact that HEAs exhibit high configurational entropy and low hydrogen diffusivity, disordered hydrogen distribution and strong hydrogen concentration gradient can be expected after the pre-charging. This makes it difficult to precisely connect the embrittlement phenomena with hydrogen concentration by using the conventional macroscopic tests with pre-charged samples. Moreover, the macroscopic tensile tests are not able to directly assess the small-scale interactions between hydrogen and dislocations, which is of strategic importance in understanding the hydrogen embrittlement mechanism. Therefore, it is necessary to perform investigations at nanoscale on the sample surface with constant and evenly distributed hydrogen to better understand the hydrogen effect on the degradation process. Recently, the effect of hydrogen on CoCrFeMnNi alloy was studied at nanoscale by Zhao et al. [29] by performing nanoindentation tests on pre-charged samples. They concluded that there is a hardness increment effect induced by the dissolved hydrogen because of the solid solution strengthening. However, owing to the outgassing diffusion process, a hydrogen depletion zone close to the surface could be expected in the pre-charged samples. This can result in uncertainties during nanomechanical testing, since the penetrating depth of the indenter is in the range of nanometers. Therefore, it is necessary to integrate in-situ hydrogen charging into nanoindentation testing to keep the surface hydrogen concentration constant by setting a proper electrochemical hydrogen charging process. The in-situ electrochemical nanoindentation (ECNI) technique, initiated by Barnoush et al. [30], has shown its advantage in probing the hydrogen effect on the nanomechanical properties of various metals

[31-33]. By recording the high resolution load-displacement (L-D) data, both the mechanical properties, such as elastic modulus and hardness, and the discrete events, including dislocation nucleation, surface deformation, and phase transformation, are able to be detected [31, 34]. In this study, the in-situ ECNI tests were performed to obtain a better understanding of the effects of hydrogen absorption and desorption on the surface integrity and nanomechanical behavior of a CoCrFeMnNi HEA. With the applied in-situ technique, the drawbacks mentioned above from ex-situ charging tests can be avoided.

2. Experimental

2.1 Materials and sample preparation

The studied material is an equiatomic HEA with nominal composition $Co_{20}Cr_{20}Fe_{20}Mn_{20}Ni_{20}$ (at. %). The alloy ingot with dimensions of 25×60×65 mm^3 was cast in a vacuum induction furnace by using cleaned pure metals (purity higher than 99.8 wt%). Alloy sheets with dimensions of 10×25×60 mm^3 were further machined from the original cast block. The as-cast alloy sheets were hot-rolled at 900 °C to a 50% thickness reduction and then homogenized at 1200 °C for 2 h in an Ar atmosphere followed by water quenching. The detailed composition of the studied HEA obtained from chemical analysis is presented in Ref. [26]. The samples used for the in-situ ECNI tests were cut by electrical discharge machining into discs with a thickness of 2 mm and a diameter of 12 mm. The disc samples were ground sequentially by using 220-4000 grit SiC papers, followed by two polishing steps with 3 μm and 1 μm diamond sprays. The surface preparation was finalized by electropolishing in a methanol/H_2SO_4 solution at 35 V for 30 s. The surface quality was then checked by using the scanning probe microscopy (SPM), and the surface root-mean-square roughness was measured to be less than 0.2 nm over 100 μm^2. After surface preparation, the microstructure of the studied material was analyzed by using a high-resolution scanning electron microscope (SEM, Quanta 650 FEG, Thermo Fisher Scientific Inc.) with a backscattered electron (BSE) detector as well as the electron backscatter diffraction (EBSD) technique.

2.2 Electrochemical measurements

In order to determine the appropriate polarization potentials for the in-situ ECNI test, the polarization curve was measured by scanning from -2500 to 1500 mV with a scan rate of 1 mV/s.

The electrolyte used in this study for both the polarization curve measurement and the in-situ nanoindentation test was a glycerol-based solution, which consisted of 600 g borax (sodium tetraborate decahydrate) dissolved in 1 L glycerol and diluted with 20% distilled water to ensure the conductivity [32]. In addition, 0.002 M $Na_2S_2O_3$ (sodium thiosulfate) was added into the solution to promote hydrogen absorption [35]. The developed electrolyte has an extremely low solubility and diffusivity of oxygen, and therefore, it is appropriate for preserving the sample surface from corrosion throughout the whole testing procedure [36]. A special three-electrode electrochemical cell was designed for the testing, and it consisted of a platinum counter electrode and a $Hg/HgSO_4$ reference electrode. All potentials in this study are reported versus this reference electrode.

2.3 In-situ ECNI

The in-situ ECNI test was performed with a Hysitron Tribo-indenter TI 950 equipped with a specially designed long-shaft Berkovich diamond tip, which was used not only for indenting but also for SPM imaging after each polarization condition to trace the changes of the surface integrity. The SPM images were analyzed with Gwyddion software. The load function used for the nanoindentation test starts with an 8000 μN/s loading segment until the peak load of 2000 μN plus a 0.45 s holding time, followed by an 8000 μN/s unloading segment with an additional 0.25 s holding time at 10% of the peak load for drift correction.

The sample was firstly tested in air as the reference condition, followed by the in-situ ECNI test at a sequence of -1500, -1600, and -1700 mV cathodic potential (CP) polarizations (more details are shown in the Section 3.2). After each cathodic polarization, an anodic polarization at 0 mV was performed to check the reversibility of nanomechanical properties after desorption of hydrogen. Hereafter, the cathodic charging potentials of -1500, -1600, and -1700 mV will be referred to as “CP1”, “CP2”, and “CP3”, while the corresponding anodic discharging potential of 0 mV will be described as “AP1”, “AP2”, and “AP3”, respectively. The sample was charged or discharged for 2 h at each potential before starting the first indentation test to ensure that a sufficient amount of hydrogen had been absorbed or desorbed. At least 27 indentations were performed in each condition to guarantee the reproducibility.

2.4 Electron channeling contrast imaging

The electron channeling contrast imaging (ECCI) technique has been proven to be an excellent SEM method based on the controlled diffraction condition with optimum contrast [37]. In the present study, ECCI was performed before and after the in-situ ECNI test to identify the evolution of dislocations induced by the electrochemical hydrogen charging. The imaging was performed at an acceleration voltage of 30 kV with a working distance of ~6.5 mm in the same SEM equipped with a solid-state four-quadrant BSE detector. The optimum channeling contrast was obtained by tilting the specimen to a situation where the grain matrix was exactly in the Bragg condition, thus enabling the diffraction vector in a two-beam condition. With the applied electron acceleration voltage and the activated diffraction condition, a visibility depth in the range of tens of nanometers was supposed to be reached [38].

2.5 Thermal desorption spectroscopy

In order to determine the content of absorbed hydrogen after different polarization process, the thermal desorption spectroscopy (TDS) test was carried out. The electrochemical hydrogen charging/discharging process was repeated on four samples that stopped at the end of each CP condition and AP3 condition, which together with an uncharged sample were tested by TDS. The TDS measurement was started immediately (less than one minute) after each charging and discharging process to eliminate the outgassing effect. The TDS was performed using a Bruker G4 PHOENIX DH hydrogen analyzer together with a mass spectrometry detector set up (ESD 100, InProcess Instruments, Germany), and the corresponding heating rate was 25 °C/min from 25 °C to 700 °C.

3. Results

3.1 Initial microstructure

Fig. 1 shows the BSE image and the normal direction-inverse pole figure (ND-IPF) map of the studied material, which revealed a single FCC structure consisting of grains with an equiaxed morphology and annealing twins. The average grain size was 160 μm, which was large enough to perform repeated indentation tests for all polarization conditions within a single grain to eliminate

the influence of different orientations. In this study, the grain with a normal direction of <112> (parallel to the indentation direction) was chosen for the in-situ ECNI testing.

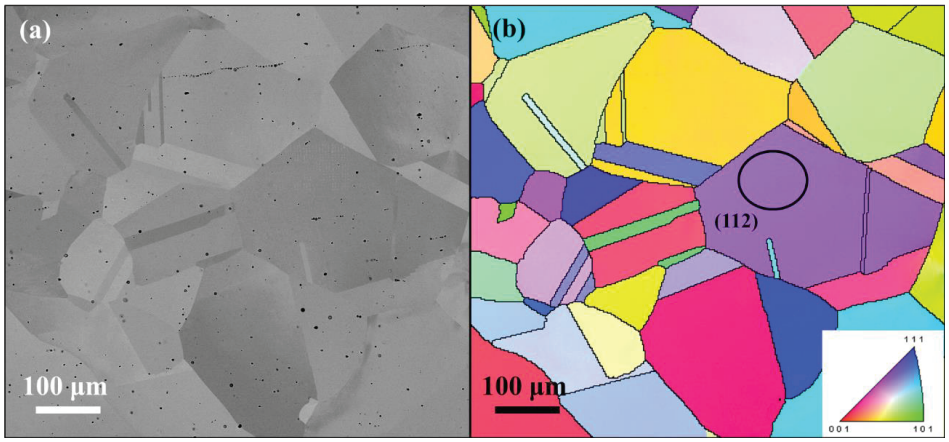

Fig. 1. (a) BSE image showing the microstructure of the investigated sample. (b) ND-IPF map of the same area with the marked (112) grain used for the in-situ ECNI testing.

3.2 Polarization curve

The polarization curve is shown in Fig. 2. The sample was cathodic polarized from -2500 to -1100 mV, where hydrogen was produced and diffused into the sample. A more negative cathodic potential resulted in a higher current density, which caused a higher hydrogen concentration on the sample surface. The anodic branch started at -1100 mV, and a passive region was obtained between -400 and 500 mV. As proposed in Section 2.3, in this study, -1500, -1600, and -1700 mV were chosen as cathodic charging potentials, while 0 mV, a value in the passive region, was chosen as the anodic discharging potential, at which the dissolved hydrogen diffused out; also, the sample surface could be kept free of corrosion. The chosen potentials are highlighted by horizontal dashed lines in the polarization curve shown in Fig. 2.

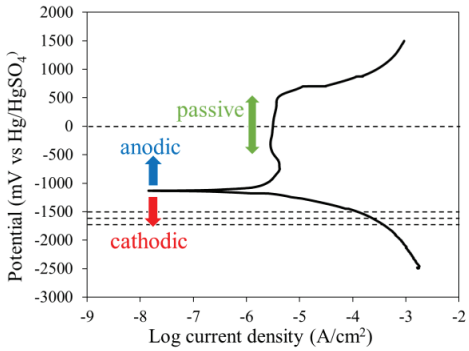

Fig. 2. Polarization curve of the investigated HEA sample. The horizontal dashed lines represent the chosen potentials for the in-situ ECNI tests.

3.3 The evolution of hydrogen induced surface steps (HISS)

The SPM images of the tested grain before and after the in-situ ECNI test under different conditions are exhibited in Fig. 3. Fig. 3a shows the original sample surface at air condition as the reference point. Figs. 3b-3d describe the sample surface after hydrogen charging at different cathodic potentials. The image in Fig. 3b was scanned after 2 h of hydrogen charging at CP1, and no noticeable changes on the surface can be seen. However, the evolution of surface steps on the sample surface can be easily observed after charging at higher potentials of CP2 and CP3 (Figs. 3c and 3d). It should be noted that the observed phenomenon (HISS) is a general feature for grains with different orientations in this material, and <112> grain is one of the most suited types of grains showing the slip behavior. By choosing <112> grain for testing, most slip features could be correctly revealed. Also, this relatively low-index orientation would not cause high complexity in the analysis. According to the corresponding surface roughness data shown in Fig. 3e, the root-mean-square roughness R_q before charging was 0.16 nm, and it remained the same after 2 h of CP1 charging followed by obvious increments to 0.26 and 0.28 nm at CP2 and CP3, respectively. The maximum height of roughness R_t showed a similar trend to that for R_q. Additionally, the ECC images of the sample surface before and after the whole in-situ ECNI test are presented in Fig. 4. The dislocations appeared as short white curved lines or dots on the dark background, indicating the intersections between the dislocations and the sample surface [38]. The fresh sample surface after electropolishing, as shown in Fig. 4a, contained uniformly distributed dislocations at a

relatively low density, whereas the hydrogen-charged surface exhibited much more dislocations that were distributed mainly around the surface steps. Based on the ECCI results, the average dislocation spacing was measured as 0.5 µm for the fresh surface (Fig. 4a), while it decreased to 0.2 µm after whole charging/discharging polarizations (Fig. 4b).

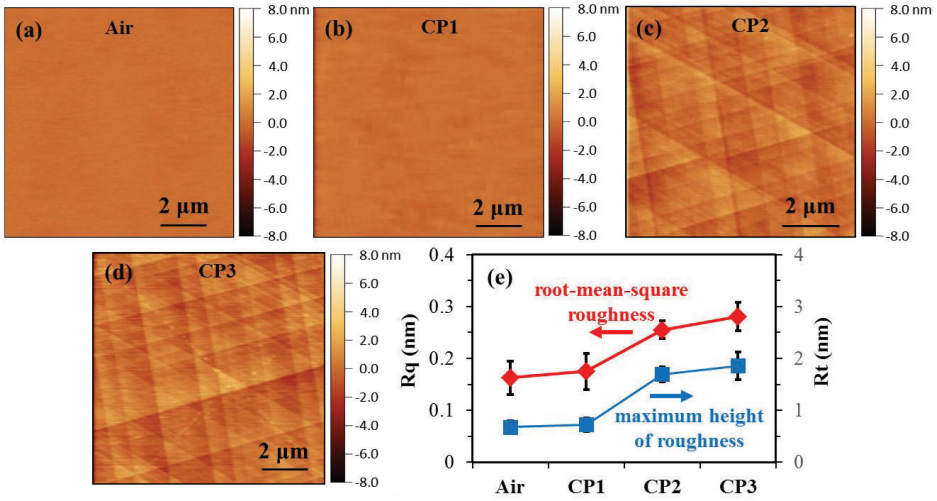

Fig. 3. The SPM images during in-situ electrochemical hydrogen charging: (a) before hydrogen charging in air; (b) after 2 h of hydrogen charging at CP1; (c) after 2 h of hydrogen charging at CP2; (d) after 2 h of hydrogen charging at CP3; (e) the root-mean-square roughness R_q (nm) and maximum height of roughness R_t (nm) under different electrochemical conditions.

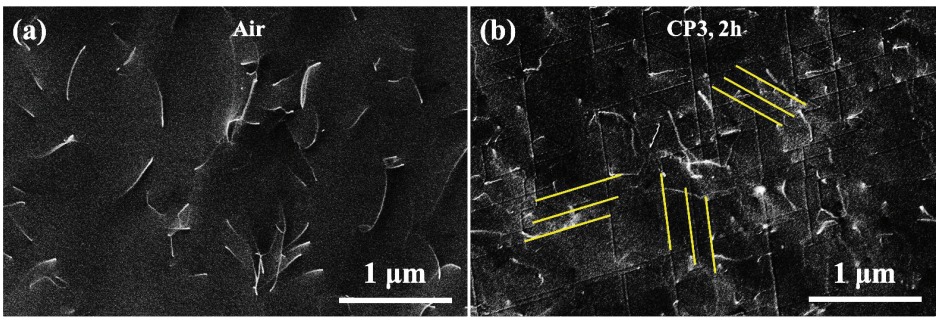

Fig. 4. The ECC images of the sample surface (a) in air and (b) after hydrogen charging at CP3 condition for 2 h. The yellow solid lines in (b) describe the directions of surface slip lines.

3.4 Nanomechanical properties

The representative L-D curves under different testing conditions are exhibited in Fig. 5. All of the curves clearly showed the following four stages: initial elastic loading; pop-in as a displacement burst; subsequent elastoplastic loading up to the maximum applied load; and elastic unloading. Except for the pop-in parts, the L-D curves measured in air and under APs were very similar, while evident changes were observed for all of the loading segments when polarized to CPs. In the following sections, the effects of hydrogen on each of the mentioned segments will be presented in detail.

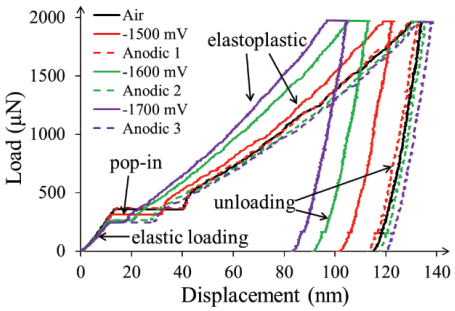

Fig. 5. The representative L-D curves for the tested grain in air, under three cathodic charging conditions and three anodic discharging conditions.

3.4.1 Elastic modulus

According to the Hertzian contact theory [39], the reduced modulus E_r of the sample can be obtained by fitting the initial elastic portion of the L-D curve with the relation:

$$P = \frac{4}{3} E_r \sqrt{R h^3} \tag{1}$$

where P is the applied load, h is the indentation depth, and R is the radius of the Berkovich tip curvature. Since the maximum penetration depth of the initial elastic segment is 10-15 nm, only the apex of the tip, which can be treated approximately as a sphere, is in contact with the material. The accurate R value was measured by performing indents on a standard fused quartz sample with a well-defined reduced modulus (69.6 GPa). By fitting the L-D curves with the Hertzian relation

up to the depth of 15 nm, the Berkovich tip was found to be described perfectly as a sphere with a radius of 1.05 μm. Therefore, the E_r value of the tested sample can be determined by Eq. (1) and the Young's modulus E can be converted from E_r by:

$$\frac{1}{E_r} = \frac{1-\upsilon_1^2}{E_1} + \frac{1-\upsilon_2^2}{E_2} \quad (2)$$

where υ is the Poisson's ratio. Here, the subscripts 1 and 2 represent the sample and the indenter tip, respectively. For a diamond tip, the elastic modulus is 1140 GPa, and the Poisson's ratio is 0.07. The Poisson's ratio of the studied CoCrFeMnNi alloy was reported as 0.26 [40]. Fig. 6 presents the Young's modulus E calculated by the Hertzian method under different conditions. The Young's modulus tested in air was 201.5 GPa, and there was no observable change (less than 1%) during the first CP-AP polarization sequence. However, when the applied potential was switched to CP2 and CP3, the Young's modulus was reduced to 197.0 and 184.4 GPa with 2.8% and 8.5% reductions, respectively, and no recovery was detected at the afterwards APs polarization.

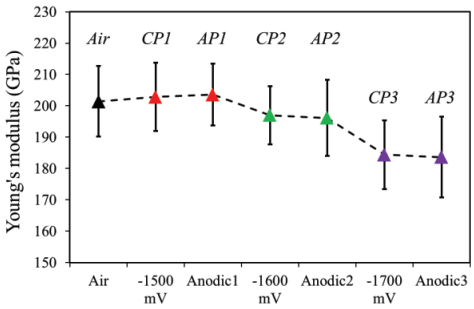

Fig. 6. Young's modulus of the studied CoCrFeMnNi HEA under different hydrogen absorption and desorption conditions.

3.4.2 Pop-in load

The pop-in phenomenon, as a sudden burst of indentation displacement, indicates the onset of plasticity. It has been proposed as a link to homogeneous dislocation nucleation or activation of a defect source such as dislocation, vacancy, or stacking fault [39, 41, 42]. Fig. 7a presents the magnified pop-in segments of typical L-D curves shown in Fig. 5. The observed changes in the pop-in load at different polarizations are summarized in Fig. 7b, where the mean values of the pop-

in load with standard deviation error bars are presented. After the application of the first charging process at CP1, the pop-in load decreased from 352 μN (as obtained in air) to 328 μN. The reduced pop-in load then recovered to a similar value to that in air when AP1 polarization was applied. The reduction in the pop-in load at the following CPs scaled up with the values of applied potentials. However, in contrast to the AP1 polarization, the pop-in load showed no recovery effect at AP2 and AP3; instead, it remained at the same value as that for the previously applied CP2 and CP3 polarization, respectively.

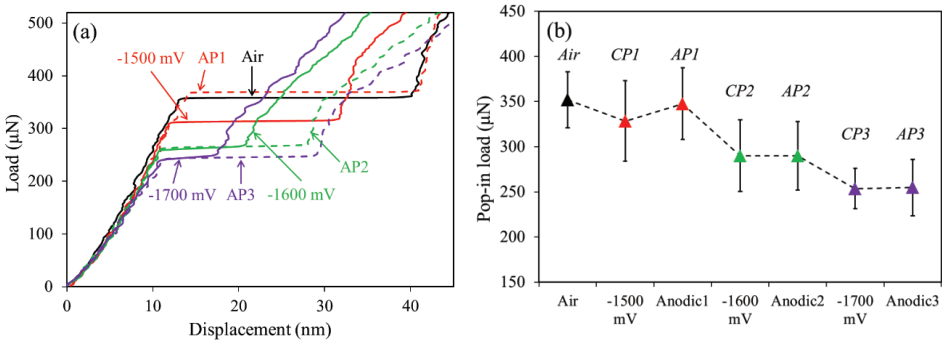

Fig. 7. (a) Magnified area of the initial elastic part and the pop-in part of L-D curves in Fig. 5. (b) The pop-in load under different polarization conditions.

3.4.3 Hardness

The hardness H of the studied material was determined from the elastic unloading segment of the L-D curve by using the Oliver-Pharr (O-P) method [43]:

$$H = \frac{P_{max}}{A_c} \tag{3}$$

where P_{max} is the maximum load during the nanoindentation test and A_c is the projected contact area according to the tip area function and the tip contact depth h_c, which can be calculated as shown in Eq. (4):

$$h_c \cong h_{max} - 0.75\frac{P_{max}}{S} \tag{4}$$

Here, h_{max} is the maximum displacement during the test and S is the stiffness extracted from the initial unloading slope of the L-D curve. The mean values of hardness under sequentially changed polarization conditions are shown in Fig. 8a. The hardness value in air was 3.36 GPa, and it accumulatively increased by 12.1%, 38.8%, and 54.8% at the applied cathodic polarizations of CP1, CP2, and CP3, respectively. In contrast to the irreversible behavior of the pop-in load and elastic modulus, the hardness recovered to (even slightly lower than) the original air-level at each AP polarization. The hydrogen-enhanced hardening effect can also be demonstrated by the reduced indenting contact areas under hydrogen charging conditions from the ECC images. As shown in Figs. 8b-8h, the radius of contact area in air was 0.66 nm, which was reduced to 0.61, 0.51, and 0.47 nm at CP1, CP2, and CP3 charging conditions, respectively. Furthermore, a fully recovered behavior of contact area was observed at each corresponding AP conditions.

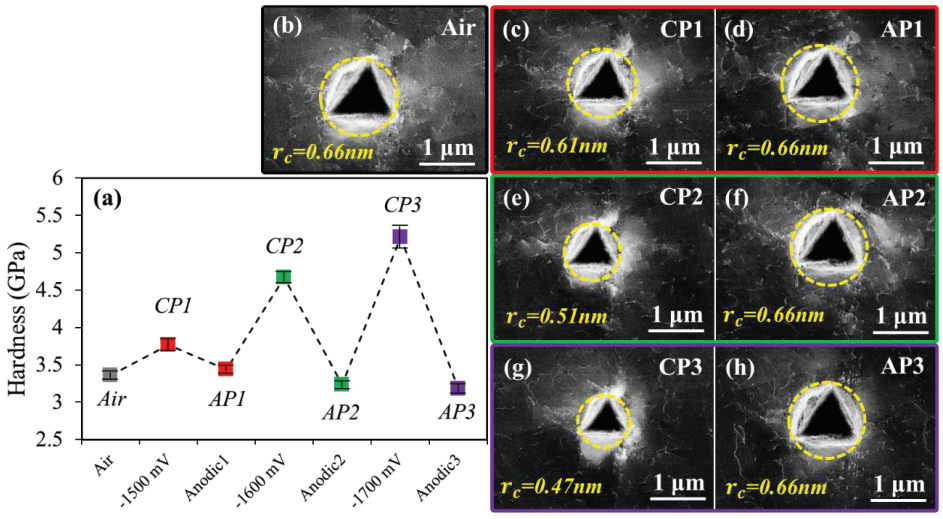

Fig. 8. (a) The mean hardness of the studied CoCrFeMnNi HEA under sequentially changed polarization conditions. (b)-(h) The ECC images of indents in different testing conditions with marked contact area.

3.5 Hydrogen content

The contents of hydrogen at different selected charging/discharging conditions were measured by TDS. As shown in Table 1, the amount of hydrogen in the uncharged sample is 0.0001 wppm, which increases to 0.10556, 1.15565, and 3.00399 wppm at the following CP1, CP2, and CP3 hydrogen charging conditions, respectively. After the 2 h anodic discharging process at AP3, the remained hydrogen content is 0.02980 wppm. According to the method used by Pontini and Hermida [44], the hydrogen concentration near the sample surface C_s during hydrogen charging can be estimated as follows:

$$C_s = \frac{\omega C_M}{4}\sqrt{\frac{\pi}{Dt}} \tag{5}$$

where ω is the thickness of tested sample, C_M is the dissolved hydrogen content measured by TDS, t is the hydrogen charging time, and D is the hydrogen diffusion coefficient chosen as 3.2×10^{-16} m^2/s from the austenitic stainless steel with similar crystal structure and composition [45]. Therefore, the hydrogen concentration $C(x,t)$ after charging time of t and at the depth of x can be calculated from the Fick's law-based "semi-infinite" model [45]:

$$\frac{C(x,t)-C_0}{C_s-C_0} = 1-\mathrm{erf}\left(\frac{x}{\sqrt{4Dt}}\right) \tag{6}$$

$$\mathrm{erf}(u) = \frac{2}{\sqrt{\pi}}\int_0^u \exp(-u^2)\,du \tag{7}$$

where C_0 is the original dissolved hydrogen measured as 0.0001 wppm in air condition. The concentration profile of hydrogen as a function of depth at different CP conditions is shown in Fig. 9. It shows that after 2 h of cathodic charging at each potential, the hydrogen mainly distributed in the surface area within a depth of 5 μm. As summarized in Table 1, the hydrogen contents on the surface, which primarily affects the nanomechanical properties, are calculated as 31.43, 560.03, and 920.79 wppm after charging at CP1, CP2, and CP3, respectively.

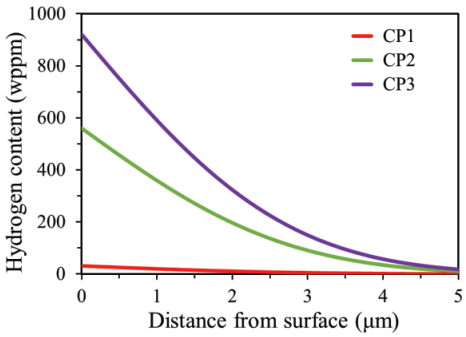

Fig. 9. Hydrogen distribution as a function of depth at different hydrogen charging conditions.

Table 1

Summary of the TDS results on samples in selected electrochemical polarization conditions.

Charging condition	Hydrogen content (wppm)	Sample thickness (mm)	Surface hydrogen content (wppm)
Air	0.00010	0.85	—
CP1	0.10556	1.02	31.43
CP2	1.15565	1.66	560.03
CP3	3.00399	1.05	920.79
AP3	0.02980	0.92	—

4. Discussion

4.1 Hydrogen induced surface steps (HISS)

As shown in Figs. 3 and 4, the formation of slip lines accumulated as steps on the sample surface with an increased dislocation density was observed after hydrogen charging process at CP2. It is necessary to mention that special care was taken during the installation of the sample into the electrochemical cell and there were no external forces applied to the surface during the charging process. Moreover, the SPM images of the sample surface after indenting in each charging conditions are shown in Fig. 10. Through comparing Fig. 10 and Fig. 3, it shows a negligible

influence on the matrix topography by the indentation tests. This further confirms that the formation of surface steps was caused by the charging process instead of nanomechanical loading. Further, it can be deduced that the potential threshold for triggering the formation of HISS is somewhere between CP1 and CP2, i.e., between -1500 mV and -1600 mV.

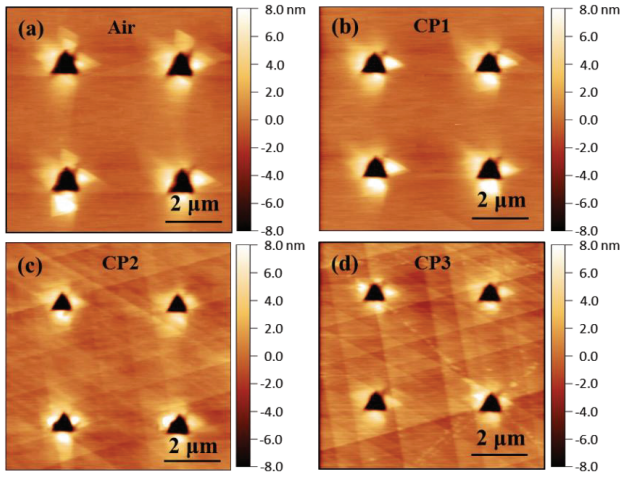

Fig. 10. The SPM images after indenting in each hydrogen charging conditions: (a) air; (b) CP1; (c) CP2; (d) CP3.

It has been reported that hydrogen can increase the mobility of dislocations because of the shielding effect on the interaction between dislocations and elastic obstacles in the frame of the HELP mechanism [7, 12, 46]. However, the hydrogen-enhanced dislocation mobility is not a sufficient condition for the formation of large number of surface steps with dislocations in this study. This is because the density of pre-existing dislocation in our sample was very low after the annealing process (Fig. 4a), which made it insufficient to form the dislocation structure as shown in Fig. 4b. Therefore, the multiple dislocations around surface steps appeared after CP2 condition must be newly generated. Base on the hydrogen concentration curve shown in Fig. 9, the atomic ratio between hydrogen and metal H_a/M_a near the sample surface at CP2 condition can be calculated by:

$$H_a/M_a = \frac{C_s \times N_A/M_H}{(10^6 - C_s) \times N_A/M_A} \quad (8)$$

where C_s is the hydrogen content on the surface layer in wppm as proposed in Eq. (5), N_A is the Avogadro constant, M_H and M_A are the molar mass of hydrogen and the studied equiatomic HEA, respectively. The SPM images in Fig. 3 show surface slip line formation at CP2 charging condition, which indicates that enough hydrogen is dissolved in the surface area to trigger the dislocation nucleation. The H_a/M_a atomic ratio in the surface area at CP2 condition is calculated as 0.031 from Eq. (8). The correlation between the content of dissolved hydrogen and resulted lattice expansion can be described by the linear relationship [47]:

$$\frac{\Delta V}{V_0} = \frac{H_a}{M_a}\frac{\Delta v}{\Omega} \quad (9)$$

Where $\Delta V/V_0$ is the change of lattice volume, Δv is the volume change of unit cell with one dissolved hydrogen atom, and Ω is the mean volume of metallic atom. The ratio of $\Delta v/\Omega$ was reported as 0.19 for 310 stainless steel [48], which has a similar crystal structure and composition to the studied material. Therefore, the lattice expansion due to hydrogen charging at CP2 condition is estimated as 0.59%. For simplicity, we assume that the lattice expansion is caused by isotropic internal stress due to abundant dissolved hydrogen. The internal stress σ_i can be estimated by using the proposed bulk modulus ($B = 137\ GPa$) from the same material as follow [49]:

$$\sigma_i = B \cdot \frac{\Delta V}{V_0} \quad (10)$$

The internal stress in the surface area at CP2 condition is calculated as 808.3 MPa, which is about four times higher than the proposed yield stress [50]. Moreover, after the same calculation, the internal stress in the surface area at CP1 condition is only 45.9 MPa. Thus, the proposed mechanism can explain the formation of slip lines in the aspect of plastic deformation theory. It needs to mention here that the above estimation of the internal stress is based on the Hook's law and can only be regarded as an approximation. Nevertheless, the estimated stresses, though not precise, are able to qualitatively and comparably explain the plastic deformation with the occurrence of slip lines on the sample surface after CP2 polarization. Moreover, according to the Defactant model proposed by Kirchheim [15, 16], the dissolved hydrogen can act as defactants and reduce the formation energy of dislocations by reducing the dislocation line energy. As a result,

the nucleation of dislocation is promoted by the dissolved hydrogen. Therefore, the combination of hydrogen-induced internal stress and the intrinsic hydrogen effect on reducing the dislocation formation energy is suggested as the reason for dislocation nucleation, followed by dislocations gliding to the surface and forming HISS due to the accumulation of slip lines. It is worth noting that such HISS phenomenon is uncommon for other conventional austenitic alloys. This is due to the combined intrinsic features of the studied CoCrFeMnNi HEA, including a low hydrogen diffusion coefficient [1], a low critical resolved shear stress [50], and a low stacking fault energy [51]. The low hydrogen diffusivity causes superabundant accumulation of hydrogen at the near-surface region, which results in a high internal stress. The low critical resolved shear stress makes the onset of planar dislocation slip easier under the hydrogen enhanced internal stress. The low stacking fault energy ensures the dislocations moving on certain preferred slip planes instead of cross-slipping or climbing, and therefore resulting in observable surface steps.

4.2 Effects of hydrogen and HISS on the nanomechanical properties

4.2.1 Effect of HISS on the elastic modulus

In general, the influence of hydrogen on the elastic modulus is still under debate. Tomatsu et al. [52] proposed that hydrogen charging has no effect on the elastic properties by performing in-situ ECNI tests on Ni-Cr bi-alloys. Shalskyi et al. [53] measured the time of passage of elastic waves in material with electrolytically absorbed hydrogen and found out the elastic modulus is enhanced by hydrogen. In contrast, Lunarska et al. [54] charged gaseous hydrogen into pure iron and found a decrease in elastic modulus by using the inverted torsion pendulum method within the temperature range of 100 to 200 K. In the present study, the elastic modulus was not affected by the hydrogen absorption-desorption processes at CP1-AP1 polarization, whereas noticeable reduction was observed when polarized to CP2 and CP3. However, if we interpret the reduction of modulus at CPs as a result of the dissolved hydrogen, the non-recovered value at the following APs after the desorption of hydrogen is unexplainable. Jiang et al. [55] performed nanoindentation tests together with theoretical calculations to study the effect of surface morphology on the nanomechanical properties, and the results indicated that the surface roughness significantly influences the elastic modulus. This is due to the fact that the elastic modulus in the current study was determined by fitting the initial elastic loading part of the L-D curve with the Hertzian contact

model, and the maximum depth of elastic deformation is approximately 10-15 nm. By contrast, the hardness value was calculated by using the Oliver-Pharr method from the elastic unloading segment, which has a larger depth of approximately 85-120 nm. Therefore, due to the different effective depths between elastic modulus and hardness, the enhanced surface roughness is supposed to have a greater effect on the elastic modulus than on the hardness (cf. Fig. 6 and Fig. 8). As a significant hydrogen-induced surface topography change was observed in the present study (cf. Fig. 3 and Fig. 4), the hydrogen effect on the elastic modulus was not able to be directly detected and the reduction of the elastic modulus was mainly stemmed from the HISS.

4.2.2 Effect of HISS on the pop-in load

For the first sequence of charging and discharging (CP1 and AP1), the results revealed that there were no changes in the surface roughness (Fig. 3e). The average spacing of dislocations for the original sample was measures as 0.5 μm based on the ECCI result (Fig. 4a). As shown in Fig. 7a, the elastic region probed a maximum depth of 15 nm before the occurrence of the pop-in, thus indicating that the average dislocation spacing was ~33 times larger than the indented depth when the pop-in happened. Therefore, an indent placed randomly on the surface has a high probability of probing on an area without pre-existing dislocations. The absence of pre-existing dislocations implies that the pop-in phenomena indicate the homogeneous dislocation nucleation. The pop-in phenomena occur when the maximum shear stress τ_{max} reaches the theoretical critical shear stress, followed by subsequent dislocation gliding and other motion events [31, 39]. According to the continuum mechanics, the τ_{max} during the indentation testing occurs below the tip as follows [56]:

$$\tau_{max} = 0.31 \left(\frac{6E_r^2}{\pi^3 R^2} P_{pop-in} \right)^{\frac{1}{3}} \tag{11}$$

Where P_{pop-in} is the pop-in load, E_r and R are the reduced modulus and tip radius, respectively, as proposed in Eq. (1). The τ_{max} values calculated in air, CP1, and AP1 were 4.06, 3.99, and 4.14 GPa, respectively. The shear modulus μ was calculated as 72.1 GPa based on the Young's modulus and Poisson's ratio. Therefore, the τ_{max} values in the aforementioned conditions are approximately equal to $\frac{\mu}{18}$, which is in good agreement with the Frenkel model for prediction of homogeneous dislocation nucleation [57].

The classic dislocation theory proposed the required free energy ΔG for nucleating a circular dislocation with radius r as [58]

$$\Delta G = 2\pi r W_{dis} + \pi r^2 \gamma - \pi r^2 b \tau_{max} \quad (12)$$

Here, W_{dis} is the dislocation line energy, γ represents the stacking fault energy and b is the Burgers vector (0.255 nm for the present HEA). Based on the Defactant model [15, 16, 59], the dissolved hydrogen can be assumed as defactants that reduce the formation energy of defects. For a linear dislocation, the dissolved hydrogen atoms can segregate around the dislocation and effectively increase the dislocation core radius and therefore reduces the dislocation line energy [60, 61]. Moreover, the stacking fault energy is also reduced by hydrogen, which has been illustrated via both experimental works and numerical simulations [62, 63]. Therefore, at the CP1 polarization with a uniform surface integrity, the reduction of pop-in load can be concluded as being caused by the hydrogen-enhanced homogeneous dislocation nucleation through the reduction of dislocation line energy and stacking fault energy.

For the following two cathodic charging processes with higher potentials at CP2 and CP3, the pop-in load decreased to 290 and 254 μN, with reductions of 17.6% and 27.8%, respectively, compared to air-values. The pop-in load remained the same at the following anodic polarizations when the dissolved hydrogen had diffused out of the sample surface. This is contradictory to the results in former in-situ ECNI studies [61, 64], which showed reversible behavior of the pop-in load during anodic polarization. However, in those former studies, the surfaces were reported to have no roughness change during the whole test. This means that the observed pop-ins are related to dislocation nucleation on a relatively dislocation-free area and the changes in pop-in load are not due to surface changes, but the ingression of hydrogen atoms. In contrast, the surface roughness in the present study increased with HISS formation at CP2 and CP3. It has been proposed that the surface steps strongly decrease the first dislocation emission, i.e. pop-in, by the stress concentration due to the decrease in initial contact area between surface steps and the indenter tip [65]. Another possibility is that hydrogen charging introduces multiple dislocations in the near-surface region, and the pop-in phenomenon begins at lower stress by activating the pre-existing dislocations instead of nucleating new sources [66]. Therefore, the pop-in behavior is very sensitive to the surface quality: for a defect-free surface, the pop-in is facilitated through the homogeneous dislocation nucleation, and reversible pop-in behavior with hydrogen ingress and

egress can be observed. In other cases, the pop-in happens by activating the existing defects. In this study, the pop-in load at the CP1 condition was caused by the homogeneous dislocation nucleation with a reversible behavior. On the contrary, irreversible pop-in load reduction was observed at higher CPs due to the activation of the pre-existing dislocations by the concentrated stress.

4.2.3 Effect of hydrogen on the hardness

In contrast to the anodic non-recovery behavior of elastic modulus and pop-in load, the hardness showed a full recovery behavior at anodic conditions as shown in Fig. 8a. The hardness values at AP2 and AP3 were even slightly lower than that of uncharged sample. This softening effect has been reported as the result of formation of superabundant vacancies during hydrogen charging [29]. In this study, since the hardness values were extracted from the deeper unloading segment, it is suggested that the increment of hardness at CPs was not caused by the HISS but by the dissolved hydrogen in the affected area. To describe the dependency of hardness on the dissolved hydrogen, the elastoplastic regions of L-D curves can be represented by the Tabor relation-based Nix-Gao model [67]. Based on the Tabor's relation $H_0 = C\sigma$, the elastoplastic part can be expressed as follows:

$$P = H_0 A_c = C\sigma A_c \tag{13}$$

where P is the applied load and A_c is the projected contact area as proposed in Eq. (1). H_0 is the depth-dependent hardness during the elastoplastic regime, σ is the flow stress, and C is the Tabor factor as 3. In the current study, all the indents were performed on a defined coarse grain, which can be treated as a single crystal. Therefore, the hardening mechanisms caused by grain boundaries and phase boundaries are not considered. Hence, the flow stress σ is consisted of lattice friction (σ_{Fric}) and Taylor stress (σ_{Taylor}). The σ_{Fric} was proposed by Refs. [50, 68] as 190 MPa including the effect of solid solution hardening for the similar HEA, while the σ_{Taylor}, indicating the interaction between dislocations, is defined by Eq. (14) [67]:

$$\sigma_{Taylor} = M\alpha\mu b\sqrt{\rho_{SSD} + \rho_{GND}} \tag{14}$$

Here, M is equal to 3.06 as the Taylor factor, μ is the shear modulus, b is the Burgers vector, and α is an empirical factor related to the mean dislocation strength, which is chosen as 0.5 [31, 69].

The ρ_{SSD} and ρ_{GND} are the density of statistically stored dislocation (SSD) and geometrically necessary dislocation (GND), respectively. The ρ_{SSD} value is assumed as 5×10^{12} m^{-2} for an annealed sample, which matches perfectly with the estimated dislocation density from ECC image shown in Fig. 4a. Based on the ECCI result in Fig. 4b, the ρ_{SSD} value for the specimen after hydrogen charging was measured as 2.5×10^{13} m^{-2}. Since there was no noticeable change in the topography and roughness between the air condition and CP1, as well as between CP2 and CP3, we assumed ρ_{SSD} values for CP1 and CP2 the same as those for air and CP3, respectively. The density of GND is described by the Nix-Gao model [67] as follows:

$$\rho_{GND} = \frac{3}{2}\frac{1}{f^3}\frac{\tan^2\theta}{bh_f} \tag{15}$$

where θ is 19.7° in this study as the equivalent cone angle representing the angle between indenter and sample surface, b is the Burgers vector, h_f is the residual indentation depth, and f is the correction factor expressed as the ratio of the plastic zone radius to the contact area radius r_{pz}/r_c [70]. The r_c can be measured from the ECC images as shown in Fig. 8, while the r_{pz} can be estimated based on the Lawn's theory [71], which relies on the ratio of Young's modulus to the hardness E/H as follows:

$$r_{pz} = \varphi\left(\frac{E}{H}\right)^{\frac{1}{3}} tan^{\frac{1}{3}}(\theta)h_f \tag{16}$$

Here, φ is the geometry constant of 3.64 for the Berkovich indenter. The values of the relevant parameters under different conditions together with the physical meanings are summarized in Table 2. By considering the effect of hydrogen on lattice friction σ_H, the equation between the hardening behavior and indenting depth can be rearranged as follows:

$$P = CM\alpha\mu bA_c\sqrt{\rho_{SSD} + \frac{3}{2}\frac{1}{f^3}\frac{tan^2\theta}{bh_f}} + C(\sigma_{Fric} + \sigma_H)A_c \tag{17}$$

By inserting the f factor calculated as 1.77 in the air condition, the curve obtained from Eq. (17) becomes fully consistent with the elastoplastic regime of the L-D curve obtained in air as shown in Fig. 11. The σ_H value in each cathodic polarization can be quantitatively obtained by fitting Eq. (17) with the elastoplastic part of the experimental L-D curves. Accordingly, the contribution of hydrogen to the lattice friction in the CoCrFeMnNi HEA is 95, 260, and 320 MPa at CP1, CP2, and CP3 polarizations, respectively. Such increases in the lattice friction are caused by the

dissolved hydrogen atoms acting as the Cottrell atmosphere around moving dislocations [21]. This short-range interaction thus retards the dislocation motion and increases the hardness value.

Table 2

Parameters used for the elastoplastic regime fitting.

	Physical meaning	Air	CP1 (-1500 mV)	CP2 (-1600 mV)	CP3 (-1700 mV)
E (GPa)	Elastic modulus	201.4	202.8	201.2	184.4
H (GPa)	Hardness	3.36	3.77	4.67	5.21
h_f (nm)	Residual depth	115.2	105.7	90.8	82.7
r_{pz} (μm)	Plastic zone radius	1.17	1.03	0.82	0.70
r_c (μm)	Contact area radius	0.660	0.605	0.510	0.470
f	Correction factor	1.77	1.70	1.61	1.49
σ_H (MPa)	Hydrogen-enhanced lattice friction	0	95	260	320

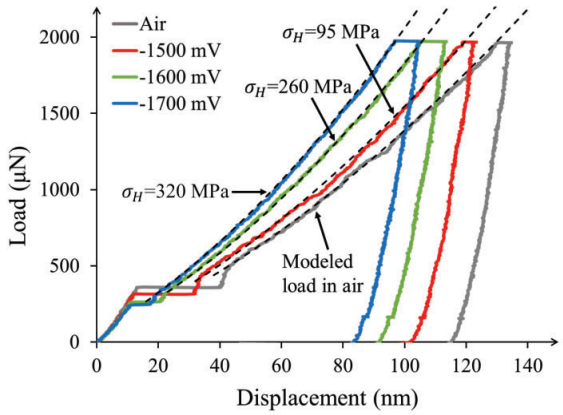

Fig. 11. The representative L-D curves for different conditions with the elastoplastic regime fitted by the Tabor relation-based Nix-Gao model.

5. Conclusion

A novel in-situ ECNI was used to examine the effects of hydrogen on the nanomechanical properties of a CoCrFeMnNi HEA. By applying cathodic charging at three different potentials and anodic discharging, the changes in the surface integrity, elastic modulus, pop-in load, and hardness were evaluated and analyzed. The main findings are summarized as follows.

1. There was no noticeable change on the sample surface during the cathodic charging process at -1500 mV, while irreversible slip lines accumulated as steps were detected at higher charging potentials of -1600 and -1700 mV. The formation of HISS is related to the plastic deformation caused by the hydrogen-induced internal stress and the intrinsic hydrogen effect on promoting dislocation nucleation through reducing the dislocation formation energy.

2. The HISS can irreversibly reduce the elastic modulus and the pop-in load. Specifically, the reduction of elastic modulus is caused by the increased surface roughness due to the HISS. The pop-in phenomenon in this circumstance is caused by the activation of pre-existing dislocation sources instead of homogeneous dislocation nucleation. The lower stress needed for activating the pre-existing dislocations and the stress concentration due to the increased surface roughness result in the reduced pop-in load.

3. The hardness is not influenced by the HISS and a reversible enhanced hardening behavior can be observed with the hydrogen ingress and egress processes. The enhanced hardness at cathodic charging conditions is related to the hydrogen-enhanced lattice friction due to the short-range interactions between dislocations and dissolved hydrogen.

4. To the best of our knowledge, the influences of HISS on the nanomechanical properties of materials especially on the studied alloy have not been discussed before. It will be necessary to consider this effect in future studies on hydrogen embrittlement and design of hydrogen-tolerant alloys.

Acknowledgements

The authors are grateful for the support provided by the Research Council of Norway through the HyF-Lex (244068/E30) project. The author (Dong Wang) would like to acknowledge the financial support from the China scholarship council.

Data availability

The raw/processed data required to reproduce these findings cannot be shared at this time as the data also forms part of an ongoing study.

Conflicts of interest

The authors declare no conflict of interest.

References:

[1] D.B. Miracle, O.N. Senkov, A critical review of high entropy alloys and related concepts, Acta Mater. 122 (2017) 448-511.
[2] J.W. Yeh, S.K. Chen, J.Y. Gan, S.J. Lin, T.S. Chin, T.T. Shun, C.H. Tsau, S.Y. Chang, Formation of simple crystal structures in Cu-Co-Ni-Cr-Al-Fe-Ti-V alloys with multiprincipal metallic elements, Metall. Mater. Trans. A 35a(8) (2004) 2533-2536.
[3] Z. Li, Interstitial equiatomic CoCrFeMnNi high-entropy alloys: carbon content, microstructure, and compositional homogeneity effects on deformation behavior, Acta Mater. 164 (2019) 400-412.
[4] T.K. Chen, T.T. Shun, J.W. Yeh, M.S. Wong, Nanostructured nitride films of multi-element high-entropy alloys by reactive DC sputtering, Surf. Coat. Technol. 188 (2004) 193-200.
[5] P.K. Huang, J.W. Yeh, T.T. Shun, S.K. Chen, Multi-principal-element alloys with improved oxidation and wear resistance for thermal spray coating, Adv. Eng. Mater. 6(1-2) (2004) 74-78.
[6] Y.F. Kao, S.K. Chen, J.H. Sheu, J.T. Lin, W.E. Lin, J.W. Yeh, S.J. Lin, T.H. Liou, C.W. Wang, Hydrogen storage properties of multi-principal-component CoFeMnTi(x)V(y)Zr(z) alloys, Int. J. Hydrog. Energy 35(17) (2010) 9046-9059.
[7] I.M. Robertson, P. Sofronis, A. Nagao, M.L. Martin, S. Wang, D.W. Gross, K.E. Nygren, Hydrogen Embrittlement Understood, Metall. Mater. Trans. A 46a(6) (2015) 2323-2341.
[8] H. Luo, Z.M. Li, A.M. Mingers, D. Raabe, Corrosion behavior of an equiatomic CoCrFeMnNi high-entropy alloy compared with 304 stainless steel in sulfuric acid solution, Corros. Sci. 134 (2018) 131-139.
[9] A.R. Troiano, R. Gibala, R. Hehemann, Hydrogen embrittlement and stress corrosion cracking: a Troiano Festschrift, ASM International, Ohio, 1984.
[10] W. Gerberich, 8 - Modeling hydrogen induced damage mechanisms in metals, in: R.P. Gangloff, B.P. Somerday (Eds.), Gaseous Hydrogen Embrittlement of Materials in Energy Technologies, Woodhead Publishing2012, pp. 209-246.
[11] D.P. Abraham, C.J. Altstetter, Hydrogen-enhanced localization of plasticity in an austenitic stainless steel, Metall. Mater. Trans. A 26(11) (1995) 2859-2871.
[12] P. Ferreira, I. Robertson, H. Birnbaum, Hydrogen effects on the interaction between dislocations, Acta Mater. 46(5) (1998) 1749-1757.
[13] S. Lynch, Hydrogen embrittlement phenomena and mechanisms, Corros. Rev. 30(3-4) (2012) 105-123.
[14] S.P. Lynch, Environmentally Assisted Cracking: Overview of Evidence for an Adsorption-Induced Localized-Slip Process, Acta Metall. 36(10) (1988) 2639-2661.
[15] R. Kirchheim, Reducing grain boundary, dislocation line and vacancy formation energies by solute segregation II. Experimental evidence and consequences, Acta Mater. 55(15) (2007) 5139-5148.
[16] R. Kirchheim, Reducing grain boundary, dislocation line and vacancy formation energies by solute segregation. I. Theoretical background, Acta Mater. 55(15) (2007) 5129-5138.
[17] R. Kirchheim, Revisiting hydrogen embrittlement models and hydrogen-induced homogeneous nucleation of dislocations, Scr. Mater. 62(2) (2010) 67-70.
[18] M. Koyama, E. Akiyama, K. Tsuzaki, Effect of hydrogen content on the embrittlement in a Fe-Mn-C twinning-induced plasticity steel, Corros. Sci. 59 (2012) 277-281.
[19] Z. Tarzimoghadam, M. Rohwerder, S.V. Merzlikin, A. Bashir, L. Yedra, S. Eswara, D. Ponge, D. Raabe, Multi-scale and spatially resolved hydrogen mapping in a Ni-Nb model alloy reveals the role of the δ phase in hydrogen embrittlement of alloy 718, Acta Mater. 109 (2016) 69-81.

[20] H. Luo, Z.M. Li, W.J. Lu, D. Ponge, D. Raabe, Hydrogen embrittlement of an interstitial equimolar high-entropy alloy, Corros. Sci. 136 (2018) 403-408.
[21] J. Song, W.A. Curtin, Mechanisms of hydrogen-enhanced localized plasticity: An atomistic study using alpha-Fe as a model system, Acta Mater. 68 (2014) 61-69.
[22] Y. Deng, A. Barnoush, Hydrogen embrittlement revealed via novel in situ fracture experiments using notched micro-cantilever specimens, Acta Mater. 142 (2018) 236-247.
[23] O. Barrera, D. Bombac, Y. Chen, T.D. Daff, E. Galindo-Nava, P. Gong, D. Haley, R. Horton, I. Katzarov, J.R. Kermode, C. Liverani, M. Stopher, F. Sweeney, Understanding and mitigating hydrogen embrittlement of steels: a review of experimental, modelling and design progress from atomistic to continuum, J. Mater. Sci. 53(9) (2018) 6251-6290.
[24] Z. Li, K.G. Pradeep, Y. Deng, D. Raabe, C.C. Tasan, Metastable high-entropy dual-phase alloys overcome the strength-ductility trade-off, Nature 534(7606) (2016) 227-30.
[25] A. Haglund, M. Koehler, D. Catoor, E.P. George, V. Keppens, Polycrystalline elastic moduli of a high-entropy alloy at cryogenic temperatures, Intermetallics 58 (2015) 62-64.
[26] H. Luo, Z. Li, D. Raabe, Hydrogen enhances strength and ductility of an equiatomic high-entropy alloy, Sci. Rep. 7(1) (2017) 9892.
[27] Y. Zhao, D.-H. Lee, M.-Y. Seok, J.-A. Lee, M.P. Phaniraj, J.-Y. Suh, H.-Y. Ha, J.-Y. Kim, U. Ramamurty, J.-i. Jang, Resistance of CoCrFeMnNi high-entropy alloy to gaseous hydrogen embrittlement, Scr. Mater. 135 (2017) 54-58.
[28] K.E. Nygren, K.M. Bertsch, S. Wang, H. Bei, A. Nagao, I.M. Robertson, Hydrogen embrittlement in compositionally complex FeNiCoCrMn FCC solid solution alloy, Curr. Opin. Solid State Mater. Sci. 22(1) (2018) 1-7.
[29] Y. Zhao, D.-H. Lee, J.-A. Lee, W.-J. Kim, H.N. Han, U. Ramamurty, J.-Y. Suh, J.-i. Jang, Hydrogen-induced nanohardness variations in a CoCrFeMnNi high-entropy alloy, Int. J. Hydrog. Energy 42(16) (2017) 12015-12021.
[30] A. Barnoush, H. Vehoff, Electrochemical nanoindentation: A new approach to probe hydrogen/deformation interaction, Scr. Mater. 55(2) (2006) 195-198.
[31] A. Barnoush, Correlation between dislocation density and nanomechanical response during nanoindentation, Acta Mater. 60(3) (2012) 1268-1277.
[32] D. Wang, X. Lu, Y. Deng, X. Guo, A. Barnoush, Effect of hydrogen on nanomechanical properties in Fe-22Mn-0.6C TWIP steel revealed by in-situ electrochemical nanoindentation, Acta Mater. 166 (2019) 618-629.
[33] M. Asgari, A. Barnoush, R. Johnsen, R. Hoel, Nanomechanical evaluation of the protectiveness of nitrided layers against hydrogen embrittlement, Corros. Sci. 62 (2012) 51-60.
[34] X. Lu, Y. Ma, M. Zamanzade, Y. Deng, D. Wang, W. Bleck, W.W. Song, A. Barnoush, Insight into hydrogen effect on a duplex medium-Mn steel revealed by in-situ nanoindentation test, Int. J. Hydrog. Energy 44(36) (2019) 20545-20551.
[35] M. Kappes, G.S. Frankel, R. Thodla, M. Mueller, N. Sridhar, R.M. Carranza, Hydrogen Permeation and Corrosion Fatigue Crack Growth Rates of X65 Pipeline Steel Exposed to Acid Brines Containing Thiosulfate or Hydrogen Sulfide, Corrosion 68(11) (2012).
[36] X. Lu, D. Wang, Z. Li, Y. Deng, A. Barnoush, Hydrogen susceptibility of an interstitial equimolar high-entropy alloy revealed by in-situ electrochemical microcantilever bending test, Mater. Sci. Eng. A 762 (2019) 138114.
[37] I. Gutierrez-Urrutia, D. Raabe, Dislocation and twin substructure evolution during strain hardening of an Fe-22 wt.% Mn-0.6 wt.% C TWIP steel observed by electron channeling contrast imaging, Acta Mater. 59(16) (2011) 6449-6462.

[38] S. Zaefferer, N.N. Elhami, Theory and application of electron channelling contrast imaging under controlled diffraction conditions, Acta Mater. 75 (2014) 20-50.
[39] K.L. Johnson, Contact Mechanics, Cambridge University Press, Cambridge, 1987.
[40] S.F. Liu, Y. Wu, H.T. Wang, J.Y. He, J.B. Liu, C.X. Chen, X.J. Liu, H. Wang, Z.P. Lu, Stacking fault energy of face-centered-cubic high entropy alloys, Intermetallics 93 (2018) 269-273.
[41] A. Barnoush, H. Vehoff, Recent developments in the study of hydrogen embrittlement: Hydrogen effect on dislocation nucleation, Acta Mater. 58(16) (2010) 5274-5285.
[42] W.W. Gerberich, J.C. Nelson, E.T. Lilleodden, P. Anderson, J.T. Wyrobek, Indentation induced dislocation nucleation: The initial yield point, Acta Mater. 44(9) (1996) 3585-3598.
[43] W.C. Oliver, G.M. Pharr, Measurement of hardness and elastic modulus by instrumented indentation: Advances in understanding and refinements to methodology, J. Mater. Res. 19(1) (2004) 3-20.
[44] A.E. Pontini, J.D. Hermida, X-ray diffraction measurement of the stacking fault energy reduction induced by hydrogen in an AISI 304 steel, Scr. Mater. 37(11) (1997) 1831-1837.
[45] V. Olden, C. Thaulow, R. Johnsen, Modelling of hydrogen diffusion and hydrogen induced cracking in supermartensitic and duplex stainless steels, Mater. Des. 29(10) (2008) 1934-1948.
[46] H.K. Birnbaum, P. Sofronis, Hydrogen-enhanced localized plasticity—a mechanism for hydrogen-related fracture, Mater. Sci. Eng. A 176(1) (1994) 191-202.
[47] M. Hoelzel, S.A. Danilkin, H. Ehrenberg, D.M. Toebbens, T.J. Udovic, H. Fuess, H. Wipf, Effects of high-pressure hydrogen charging on the structure of austenitic stainless steels, Mater. Sci. Eng. A 384(1-2) (2004) 255-261.
[48] D.G. Ulmer, C.J. Altstetter, Phase-Relations in the Hydrogen Austenite System, Acta Metall. Mater. 41(7) (1993) 2235-2241.
[49] G. Laplanche, P. Gadaud, O. Horst, F. Otto, G. Eggeler, E.P. George, Temperature dependencies of the elastic moduli and thermal expansion coefficient of an equiatomic, single-phase CoCrFeMnNi high-entropy alloy, J. Alloys Compd. 623 (2015) 348-353.
[50] Z. Wu, C.M. Parish, H. Bei, Nano-twin mediated plasticity in carbon-containing FeNiCoCrMn high entropy alloys, J. Alloys Compd. 647 (2015) 815-822.
[51] A.J. Zaddach, C. Niu, C.C. Koch, D.L. Irving, Mechanical Properties and Stacking Fault Energies of NiFeCrCoMn High-Entropy Alloy, Jom 65(12) (2013) 1780-1789.
[52] K. Tomatsu, K. Miyata, T. Omura, Electrochemical Nanoindentation Study on Influence of Hydrogen on Local Mechanical Properties of Fcc Metals at Slow Strain Rate, ISIJ Int. 56(3) (2016) 418-423.
[53] V.R. Skalskyi, Z.T. Nazarchuk, S.I. Hirnyi, Effect of electrolytically absorbed hydrogen on Young's modulus of structural steel, Materials Science 48(4) (2013) 491-499.
[54] E. Lunarska, A. Zielinski, M. Smialowski, Effect of Hydrogen on Shear Modulus of Polycrystalline Alpha-Iron, Acta Metall. 25(3) (1977) 305-308.
[55] W.G. Jiang, J.J. Su, X.Q. Feng, Effect of surface roughness on nanoindentation test of thin films, Eng. Fract. Mech. 75(17) (2008) 4965-4972.
[56] C. Begau, A. Hartmaier, E.P. George, G.M. Pharr, Atomistic processes of dislocation generation and plastic deformation during nanoindentation, Acta Mater. 59(3) (2011) 934-942.
[57] J. Frenkel, Zur Theorie der Elastizitätsgrenze und der Festigkeit kristallinischer Körper, 37(7) (1926) 572-609.
[58] P.M. Anderson, J.P. Hirth, J. Lothe, Theory of Dislocations, 3rd ed., Cambridge University Press, Cambridge, 2017.

[59] I.M. Robertson, The effect of hydrogen on dislocation dynamics, Eng. Fract. Mech. 68(6) (2001) 671-692.
[60] A. Barnoush, H. Vehoff, Hydrogen embrittlement of aluminum in aqueous environments examined by in situ electrochemical nanoindentation, Scr. Mater. 58(9) (2008) 747-750.
[61] M. Zamanzade, H. Vehoff, A. Barnoush, Cr effect on hydrogen embrittlement of Fe3Al-based iron aluminide intermetallics: Surface or bulk effect, Acta Mater. 69 (2014) 210-223.
[62] M.Q. Chandler, M.F. Horstemeyer, M.I. Baskes, P.M. Gullett, G.J. Wagner, B. Jelinek, Hydrogen effects on nanovoid nucleation in face-centered cubic single-crystals, Acta Mater. 56(1) (2008) 95-104.
[63] P.J. Ferreira, I.M. Robertson, H.K. Birnbaum, Influence of hydrogen on the stacking-fault energy of an austenitic stainless steel, Mater. Sci. Forum 207-209 (1996) 93-96.
[64] A. Bamoush, N. Kheradmand, T. Hajilou, Correlation between the hydrogen chemical potential and pop-in load during in situ electrochemical nanoindentation, Scr. Mater. 108 (2015) 76-79.
[65] D.B. Shan, L. Yuan, B. Guo, Multiscale simulation of surface step effects on nanoindentation, Mater. Sci. Eng. A 412(1-2) (2005) 264-270.
[66] Z.G. Wang, H. Bei, E.P. George, G.M. Pharr, Influences of surface preparation on nanoindentation pop-in in single-crystal Mo, Scr. Mater. 65(6) (2011) 469-472.
[67] W.D. Nix, H.J. Gao, Indentation size effects in crystalline materials: A law for strain gradient plasticity, J. Mech. Phys. Solids 46(3) (1998) 411-425.
[68] J.Y. He, H. Wang, H.L. Huang, X.D. Xu, M.W. Chen, Y. Wu, X.J. Liu, T.G. Nieh, K. An, Z.P. Lu, A precipitation-hardened high-entropy alloy with outstanding tensile properties, Acta Mater. 102 (2016) 187-196.
[69] O. Bouaziz, S. Allain, C.P. Scott, P. Cugy, D. Barbier, High manganese austenitic twinning induced plasticity steels: A review of the microstructure properties relationships, Curr. Opin. Solid State Mater. Sci. 15(4) (2011) 141-168.
[70] K. Durst, B. Backes, M. Goken, Indentation size effect in metallic materials: Correcting for the size of the plastic zone, Scr. Mater. 52(11) (2005) 1093-1097.
[71] B.R. Lawn, A.G. Evans, D.B. Marshall, Elastic/Plastic Indentation Damage in Ceramics: The Median/Radial Crack System, J. Am. Ceram. Soc. 63(9-10) (1980) 574-581.